

Improving the Performance of III-Nitride Emitters
by Nanostructure Fabrication and Surface Plasmon
Coupling

Paul James Renwick

A thesis submitted for the degree of Doctor of Philosophy.
Department of Electronic and Electrical Engineering
The University of Sheffield

December, 2013

Abstract

III-Nitride based LEDs are quickly being adopted as the next generation in almost all lighting applications due to their potential ability to emit throughout the visible wavelength spectrum. Major challenges exist however which need to be overcome to further increase the adoption of GaN based LEDs, including low efficiency, especially in the green wavelength (and longer) emitting region, and efficiency droop, currently a major issue with GaN based LEDs.

This thesis begins by discussing studies made on nanostructures, where improvements to internal quantum efficiency and light extraction efficiency of InGaN/GaN MQW structures are observed. An improvement in efficiency droop is also observed, linked to a reduction in LO-phonon coupling, and quantified by data fitting and the Huang-Rhys factor.

Surface plasmon-quantum well interaction is discussed, where an optimised Ag film thickness and morphology is developed leading to an increase in PL emission of up to twenty five times for InGaN/GaN SQW structures, as well as a improvement in internal quantum efficiency.

The combination of these two techniques is investigated, resulting in the development of single nanorod emitters showing significant enhancement of InGaN QW structures. Finally stimulated emission is observed by surface plasmon coupling enhanced InGaN QW based single nanorods, offering a potential fabrication technique to realise nano-laser technologies.

Acknowledgements

I would like to take this opportunity to mention several important people who have made this thesis possible.

My first thanks must go to Professor Tao Wang, for giving me the opportunity to pursue this work, and for his guidance, insight and encouragement during the past four years. Regards also go to Professor Richard Tozer, my second supervisor, for his continued help and interest in my academic progress.

I would like to thank the whole nitride team in Sheffield, but in particular mention those who have had a key role in this project. Doctor Jie Bai and Doctor Qi Wang mentored me early in this work, and effectively trained me on the fabrication and characterisation equipment in the EPSRC III-V centre and the nitrides labs (As well as providing various SEM images and data). Yipin Gong, Xiang Yu and Kun Xing grew samples for this work and performed XRD experiments. Doctor Bin Liu and Rick Smith helped immensely with μ PL and TRPL measurements, and Doctor Yaonan Hou has taken over the single nanorod work and achieved great results. I would also like to thank my colleagues in office 203 for making it a great place to work and Paul Haines and the other technical staff for their continued help with equipment.

I must give thanks to my colleagues at my current employer INEX Nanotechnology, who have been incredibly flexible and understanding during the last months of this work.

Finally thanks go to my friends and family for their love and support, and in particular to Hattie and my parents for their help, motivation and continued encouragement.

Publications

Journal Publications

1. Y. Hou, **P. Renwick**, B. Liu, J. Bai and T. Wang “*Room temperature plasmonic lasing in a continuous wave operation mode from an InGaN/GaN single nanorod with a low threshold*” In Submission (2014)
2. **P. Renwick**, H. Tang, J. Bai and T. Wang “*Reduced LO-phonon-exciton interaction in InGaN/GaN nanorod structures*” Appl. Phys. Lett. 100, 182105 (2012)
3. **P. Renwick**, H. Tang, Q. Wang, R. Smith and T. Wang “*Enhanced internal quantum efficiency of an InGaN/GaN quantum well as a function of silver thickness due to surface plasmon coupling*” Phys. Stat. Sol. C, Vol.8, Issue 7-8, Page 2176, (2011)

Conference Contributions

1. **P. Renwick**, H. Tang, Y. P. Gong, K. Xing, J. Bai and T. Wang “*Study of LO-phonon and exciton interaction in GaN/InGaN MQW nanorod structures*” UK Nitrides Consortium (UKNC) Winter Conference, University of Bath, UK (2012)
2. **P. Renwick**, H. Tang and T. Wang “*Evaluating Internal Quantum Efficiency of Green LEDs via Electroluminescence*” UK Nitrides Consortium (UKNC) Winter Conference, University of Manchester, UK (2011)
3. **P. Renwick**, H. Tang, Q. Wang, R. Smith and T. Wang “*Enhanced internal quantum efficiency of an InGaN/GaN quantum well as a function of Ag thickness due to surface plasmon coupling*” International Workshop on Nitride Semiconductors, Tampa, Florida, USA (2010)

-
4. **P. Renwick**, Q Wang, J Bai, R Smith and T Wang “*Significantly Enhanced Photoluminescence of an InGaN/GaN Quantum Well due to the Surface Plasmon Coupling Effect*” UK Semiconductors and UK Nitrides Consortium (UKNC) Summer Meeting, The University of Sheffield, UK (2010)
 5. Y. Hou **P. Renwick**, B. Liu, J. Bai and T. Wang “*Room temperature plasmonic lasing from a single nanorod with a low thresholds*” UK Nitrides Consortium (UKNC) Winter Conference, The University of Bristol, UK (2014)
 6. B. Liu, Y. Xiang, R. Smith, H. Tang, **P. Renwick**, X. Kun, B. B. Xu, Y. P. Gong, J. Bai, T. Wang “*Improved optical properties and anisotropy of semi-polar GaN thin films and InGaN/GaN multiple quantum wells grown on nanorod templates*” UK Semiconductors and UK Nitrides Consortium (UKNC) Summer Meeting, Sheffield Hallam University and The University of Sheffield, UK (2013)
 7. J. Bruckbauer, P. R. Edwards, **P. Renwick**, T. Wang and R. W. Martin “*Optical Investigation of LED Structures Using Cathodoluminescence Hyperspectral Imaging*” SET for Britain event, House of Commons, Westminster Parliament, UK (2011)
 8. Q. Wang, **P. Renwick**, F. Ryder and T. Wang, “*Internal quantum efficiency of an InGaN/GaN quantum dot structure grown on GaN using a high temperature AlN buffer*” UK Semiconductors and UK Nitrides Consortium (UKNC) Summer Meeting, The University of Sheffield, UK (2010)
 9. Y. Gong, J. Zhang, **P. Renwick** and T. Wang “*Growth and characterisation of AlN with improved crystal quality by using multiple porous AlN buffers on sapphire*” UK Nitride Consortium (UKNC) Winter Conference, Tyndall Institute, Cork, Ireland (2010)
 10. J. Zhang, Y. Gong, Q. Wang, **P. Renwick** and T. Wang “*Quantum well thickness dependent optical anisotropy of spontaneous emission from AlGaIn multiple quantum well structures*” UK Nitride Consortium (UKNC) Winter Conference, Tyndall Institute, Cork, Ireland (2010)

Acronyms

AFM Atomic Force Microscopy
CB Conduction Band
CVD Chemical Vapour Deposition
CW Continuous Wave
DOS Density of States
DADR Density Activated Defect Recombination
DPSS Diode-Pumped Solid-State
FP Fabrey Perot
 F_P Purcell Factor
FWHM Full Width at Half Maximum
HF HydroFluoric acid
HR Huang-Rhys
IAR Indirect Auger Recombination
IPA Iso-Propyl Alcohol
IQE Internal Quantum Efficiency
LED Light Emitting Diode
LO Longitudinal Optical
LSP Localised Surface Plasmon
LT Low Temperature
MBE Molecular Beam Epitaxy
MOVCD Metal Organic Chemical Vapour Deposition
NR Nanorod
PECVD Plasma Enhanced Chemical Vapour Deposition
PL Photoluminescence
PLE Photoluminescence Excitation
PMT Photomultiplier Tube
QCM Quartz Crystal Monitor
QCSE Quantum Confined Stark Effect
QD Quantum Dot

QW Quantum Well
RSM Reciprocal Space Map
RT Room Temperature
SDS Sodium Dodecyl Sulphate
SEM Scanning Electron Microscopy
SOG Spin On Glass
SP Surface Plasmon
SQW Single Quantum Well
TCSPC Time Correlated Single Photon Counting
TEM Transmission Electron Microscopy
TMA Trimethyl Aluminium
TMG Trimethyl Gallium
TMI Trimethyl Indium
TO Transverse Optical
TRPL Time Resolved Photoluminescence
VB Valence Band
VCSEL Vertical Cavity Surface Emitting Laser
XRD X-ray Diffraction
YL Yellow Luminescence

Contents

| | |
|---|-----------|
| Acknowledgements | i |
| Publications | ii |
| Acronyms | iv |
| 1 Introduction | 1 |
| 1.1 Current Status of III-Nitride Optoelectronics | 1 |
| 1.2 History and Development of III-Nitride Light Emitters | 2 |
| 1.3 Challenges | 4 |
| 1.3.1 Substrate Mismatch and Growth Difficulties | 5 |
| 1.3.2 The Quantum Confined Stark Effect | 7 |
| 1.3.3 Efficiency Droop | 8 |
| 1.4 Motivation | 10 |
| References | 12 |
| 2 Background | 15 |
| 2.1 Properties of III-Nitrides | 15 |
| 2.1.1 Crystal Structure | 15 |
| 2.1.2 Electrical and Chemical Properties | 15 |
| 2.1.3 Band Structure | 17 |
| 2.1.4 Ternary Alloy III-Nitride Materials | 19 |
| 2.1.5 Carrier Recombination | 19 |
| 2.1.6 LED Structures | 21 |
| 2.1.7 Stimulated Emission and Lasing | 23 |
| 2.2 III-Nitride MOCVD Growth | 27 |
| 2.3 Low Dimensional Structures | 32 |
| 2.4 Carrier Localisation | 36 |
| 2.5 The Quantum Confined Stark Effect | 37 |
| 2.5.1 Piezoelectric Effects | 37 |

| | | |
|----------|---|-----------|
| 2.5.2 | Spontaneous Polarisation | 38 |
| 2.6 | Efficiency Droop | 42 |
| 2.7 | Plasmonics | 45 |
| | References | 49 |
| 3 | Experimental Techniques | 55 |
| 3.1 | Optical Characterisation | 55 |
| 3.1.1 | Conventional PL Set-up | 57 |
| 3.1.2 | High Power PL | 61 |
| 3.1.3 | Time Resolved PL | 62 |
| 3.2 | Sample Fabrication | 63 |
| 3.2.1 | Preparation of Samples | 63 |
| 3.2.2 | Metal Deposition | 64 |
| 3.2.3 | Dielectric Material Deposition by Chemical Vapour Methods | 65 |
| 3.2.4 | Rapid Thermal Processing | 66 |
| 3.2.5 | Dry Etching of Semiconductor and Dielectric Materials | 67 |
| 3.2.6 | LED Fabrication | 69 |
| 3.3 | Structure Characterisation | 71 |
| 3.3.1 | Atomic Force Microscopy | 71 |
| 3.3.2 | Scanning Electron Microscopy | 72 |
| 3.3.3 | X-Ray Diffraction | 73 |
| | References | 75 |
| 4 | Optical Investigation of InGaN/GaN Nanorod Array Structures as a Method of Improving Efficiency and Efficiency Droop Characteristics | 77 |
| 4.1 | Nanostructure Fabrication | 77 |
| 4.1.1 | Nanorod Array Fabrication | 78 |
| 4.1.2 | Nano-mask Characterisation | 81 |
| 4.2 | Characterisation of As Grown Sample | 81 |
| 4.3 | Study of Internal Quantum Efficiency of Nanorod Structures | 83 |
| 4.3.1 | Increased Extraction Efficiency | 86 |
| 4.4 | PL Investigation of Localisation in Nanostructures | 88 |
| 4.4.1 | Varshni Fitting | 89 |
| 4.4.2 | In-Plane Exciton Localisation in Nanorods | 90 |
| 4.5 | Study of Strain Relaxation | 91 |
| 4.6 | Reduction in Longitudinal-Optical Phonon - Exciton Interaction | 93 |
| 4.6.1 | Background | 93 |
| 4.6.2 | Investigation of Phonon-Exciton Coupling | 93 |

| | | |
|----------|---|------------|
| 4.7 | Reduction of Efficiency Droop in Nanorods | 97 |
| 4.8 | Conclusions | 99 |
| | References | 100 |
| 5 | Study of the Enhancement of InGaN QWs by Surface Plasmon Coupling | 105 |
| 5.1 | Introduction to Exciton-Plasmon Interaction | 105 |
| 5.2 | Investigation of Ag Film Thickness on Surface Plasmon Enhancement of InGaN SQW Structures | 108 |
| 5.2.1 | Sample Fabrication | 108 |
| 5.2.2 | Optical Characterisation of Surface Plasmon Enhanced InGaN SQWs | 109 |
| 5.2.3 | PL Enhancement | 110 |
| 5.2.4 | Peak Wavelength Blue Shift | 112 |
| 5.3 | Investigation of Ag Grain Size Dependence on Surface Plasmon Enhancement | 114 |
| 5.4 | Study of Internal Quantum Efficiency of an InGaN SQW Enhanced by Surface Plasmon Coupling | 116 |
| 5.5 | Study of Surface Plasmon Enhanced InGaN QW Exciton Dynamics . | 118 |
| 5.6 | Conclusions | 121 |
| | References | 123 |
| 6 | Stimulated Emission from Single Nanorods Enhanced by Surface Plasmon Coupling | 125 |
| 6.1 | Single Nanorod Emitters | 125 |
| 6.2 | Single Nanorod Fabrication Techniques | 126 |
| 6.2.1 | Silicon Dioxide Nanosphere Mask | 126 |
| 6.2.2 | Separating and Depositing Single Nanorods | 128 |
| 6.2.3 | Substrates for Single Nanorod Deposition | 130 |
| 6.3 | Characterisation of Single Nanorod Emitters | 131 |
| 6.3.1 | Planar and Nanorod Sample Characterisation with Conventional PL | 131 |
| 6.3.2 | MicroPL Characterisation of Single Nanorods | 132 |
| 6.4 | Study of Surface Plasmon Induced Single Nanorod Lasing | 137 |
| 6.4.1 | Stimulated Emission from Single Nanorods Enhanced by Surface Plasmon Coupling | 138 |
| 6.4.2 | Sample Fabrication | 139 |
| 6.4.3 | Theory of InGaN Single Nanorod-Surface Plasmon Stimulated Emission | 141 |

| | | |
|----------|--|------------|
| 6.4.4 | Excitation Power Dependant MicroPL | 142 |
| 6.5 | Conclusion | 149 |
| | References | 151 |
| 7 | Conclusions | 155 |
| 7.1 | Conclusions | 155 |
| 7.2 | Future Work | 156 |
| 7.2.1 | Advanced Photoluminescence Studies | 156 |

Introduction

1.1 Current Status of III-Nitride Optoelectronics

The energy crisis and climate change are major problems currently facing the world. One of the major uses of energy is general illumination, which may account for up to 19% of the world's total energy consumption [1]. It is therefore becoming increasingly important to develop solid state lighting technologies with ultra high efficiency in order to replace traditional light sources, such as incandescent and fluorescent systems.

III-nitride semiconductors have a direct bandgap structure, which potentially allows the fabrication of highly efficient solid state emitters. Importantly, their bandgaps also cover the entire visible spectrum and a major part of the ultraviolet (UV) spectrum (broadly from ~ 0.7 eV for InN, through 3.5 eV for GaN, to 6.2 eV for AlN). Therefore, III-nitrides are currently the best candidates for the fabrication of the ultimate lighting source for general illumination.

Over the past 20 years, major advances have been made in developing InGaN-based blue light emitting diodes (LEDs), currently the key component for generating white light (using the main approach for fabrication of white LEDs - blue LED and a down conversion yellow phosphor). Very recently, white LEDs emitting at 276 lm/W have been reported, which is over ~ 10 times the efficiency of incandescent bulbs and more than ~ 5 times higher than the efficiency of compact florescent technologies [2]. This is still far from the maximum theoretical prediction of 350 lm/W [3] from an InGaN LED however. Furthermore, a significant issue with colour rendering is encountered due to the simple combination of “blue LED + yellow phosphor” for white lighting, which has low emission in the green wavelength region.

The ultimate white lighting technology, which is potentially fully adjustable and close to the natural colour temperature of sunlight, would be a combination of red, green and blue LEDs (i.e. RGB). Currently, the performance of green LEDs lag

far behind blue emitting LED technologies due to a number of technological challenges and fundamental limits. These difficulties also extend to the current high performance blue LEDs, for which there exists a number of fundamental problems including the major hurdle of efficiency droop at large drive current. There is therefore a need to understand a number of fundamental issues surrounding III-nitrides, and develop new technologies and approaches to further improve the performance of III-nitride based emitters.

1.2 History and Development of III-Nitride Light Emitters

The first light emitting diodes were developed by R. Biard and G. Pittman from a gallium arsenide based p-n junction in 1961 emitting in the infra-red region [4]. In 1962 the first LED to emit in the visible region was developed by N. Holonyak, where phosphorous was incorporated into gallium arsenide in order to increase the bandgap and thus generate red light [5]. By the mid 1960s researchers had developed gallium phosphide light emitters capable of emission in the green wavelength range, although at a low efficiency due to the material's indirect bandgap [6].

Over the next 25 years, significant progress was made in both pushing the photon emission energy higher, and increasing performance, with ~ 10 times increase in output performance per decade in the red wavelength range as seen in Figure 1.1.

The study of III-nitrides began in the 1960s, where an understanding of the direct band structure of III-nitride materials and their potential application in the visible spectral region was developed. Rudimentary blue and green light emitting diodes consisting of a metal-semiconductor (m-i-n) structure were developed by Pankove et al. as early as 1972 [7], but development of p-n junction devices in this wavelength region didn't take off until the beginning of the 1990s, as illustrated in Figure 1.1, after several key developments in III-nitride materials technology.

In the 1990s, silicon carbide and zinc selenide were developed into reasonably effective blue, green and white LEDs. Fundamental flaws exist in these materials however: SiC LEDs tend to have low efficiency due to the material's indirect band-gap, meaning a momentum shift is required to allow electron and hole carriers to recombine [9]. ZnSe devices also have problems with propagation of defects during use, resulting in limited lifespan of devices [10]. As such, GaN has become the most commercially viable material with direct band-gap wide enough to emit in the blue region and beyond [11].

Initially difficulties were encountered finding suitable substrates for GaN growth, however a breakthrough by Akasaki et al. lead to sapphire substrates being iden-

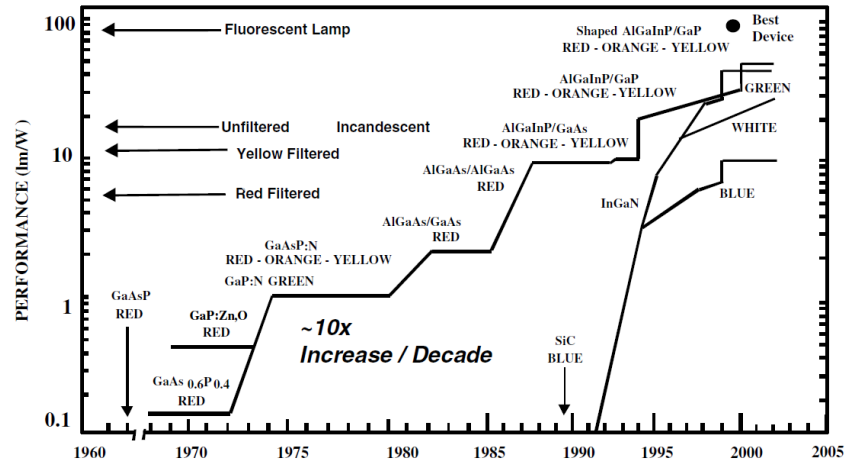


Figure 1.1: The improvement in performance of LEDs emitting in the visible region from 1962 to 2002. The performance of other lighting technologies such as incandescent and fluorescent lamps are also shown for comparison. Figure from [8] reprinted with permission.

tified as suitable medium to produce good crystal quality material, despite a lattice mismatch of $\sim 16\%$ [12]. Initial attempts at p-type GaN material had poor p-conductivity, however developments by Amano et al. lead to p-type doping of GaN with magnesium using a post-growth acceptor activation method [13]. A chance discovery using a low energy electron beam to irradiate the samples allowed the magnesium dopant to become activated, increasing conductivity by several orders of magnitude [14]. These breakthroughs paved the way for the first reported p-n junctions in GaN in 1989 by Akasaki's group [14], and research into III-nitride LEDs began to rapidly develop.

The first InGaN based LEDs with emission on the candela scale were demonstrated in the blue spectral region in 1994 by Nakamura et al. [15], where a double heterostructure was used to sandwich a single Zn-doped InGaN layer, instead of the conventional multiple quantum well (MQW) active regions used today. From then on, further development allowed the growth of high quantum efficiency LED structures containing InGaN MQWs emitting at wavelengths from 365 nm (ultraviolet) to 530 nm (green) [16].

As crystal quality improvements were made in the growth of GaN and associated alloys, the possibility of lasers was realised. As early as 1990, stimulated emission from GaN in the UV region was discovered [17], and by 1996 blue/violet lasers emitting around 405nm were developed using InGaN quantum wells (QW) as the active medium for stimulated emission [18]. This was followed by the commercialisation of higher wavelength lasers, incorporating more indium into the QWs providing a lower band-gap. UV lasers were also developed operating at 365nm and 375nm, utilising

quaternary AlInGaN alloys [19] or an InGaN QW emission region with AlGaIn alloy barriers to aid in carrier confinement [20], and recent work on improving crystal quality has led to green wavelength III-nitride lasers [21].

Combining a short wavelength LED (emission in the blue wavelength range) with suitable phosphors (emitting in the yellow-red range) enabled the next generation of white light emitting LEDs to be developed. As commercialisation continued, the demand for white LEDs to replace incandescent bulbs for general lighting increased massively. At the time of writing, several local authorities in the UK are replacing entire city street lighting systems with white LEDs based on InGaN blue LEDs and a yellow/red phosphor [22].

With massive investment into GaN based emitters, improvements in efficiency and reduction in cost have been achieved, and the current state of the art white LEDs, made up of a blue LED with yellow phosphor have luminescence efficacy of over 276 lm/W [2]. Many new methods of reducing the cost of LED growth and fabrication have also been employed, including many wafer pocket reactors, increasing substrate size and using alternative substrates to costly sapphire, including the recent commercialisation of GaN on silicon substrates [23].

Further developments to improve crystal quality, and reduce efficiency droop and piezoelectric strain effects have led to recent work on non-polar and semi-polar III-nitride growth. Polar growth, in the Ga-polar (0001) c-orientation is still the dominant method used commercially, but non-polar growth on the m- or a-axis alleviates the piezoelectric effects found in the c-axis, which can improve emission efficiency [24]. Growth in semi-polar directions has also been developed using patterned substrates to expose specific crystal facets in the GaN crystal, allowing growth in various orientations with different polarisation fields [25]. The use of non- or semi-polar GaN crystal orientations can potentially provide the best device performance, however growth difficulties still limit this technology.

1.3 Challenges

From the previously discussed initial development of InGaN blue LEDs by S. Nakamura et al. [15], research in III-nitride materials increased dramatically. In theory, GaN/InGaN heterostructures can produce light anywhere in the green wavelength range and above towards the red, however, as illustrated in Figure 1.3, the efficiency of an InGaN emitter at 600 nm emission wavelength is very low. At this wavelength however, GaAs and GaP based emitters can be used, with efficient AlGaP emission in the yellow region at ~ 580 nm observed. Lower wavelength emission from this material becomes indirect and inefficient however; with the GaP band-gap (corresponding to 555 nm wavelength) being the lower limit of this material [26].

This “Green Gap” in LED technology, between highly efficient Blue LEDs and very high efficiency red and yellow LEDs is a major technological hurdle, preventing development and improvement of many lighting applications. The importance of improving the efficiency of LEDs at this wavelength range is illustrated in Figure 1.2, where it is clear that the wavelength sensitivity of the human eye is at a maximum when LED efficiency reaches its minimum [27], suggesting large improvements in colour temperature and usable output of light are possible with improved green LEDs, as well as fully controllable RGB emitters.

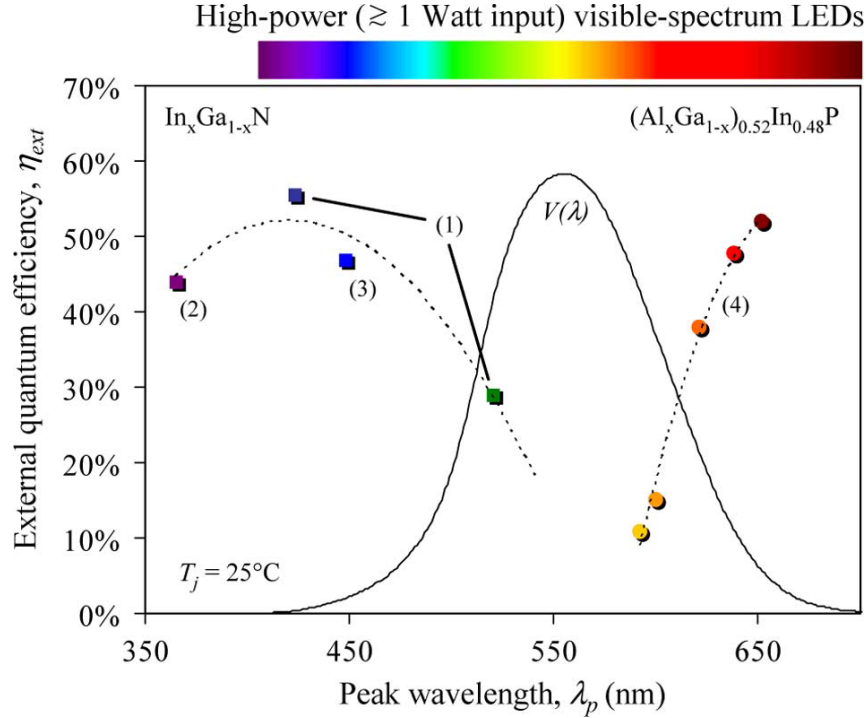


Figure 1.2: The “Green Gap” in current LED technology compared with the sensitivity of the human eye with wavelength $V(\lambda)$, showing a clear discrepancy. The LEDs 1 and 2 are InGaIn “Flip Chip” devices, LED 3 is a conventional InGaIn LED and LEDs 4 are various Philips Lumileds AlGaInP devices. Reprinted with permission from [27].

Several major difficulties in the development of high efficiency InGaIn LEDs are encountered. The main issues limiting the current performance of III-nitride emitters are detailed in the following subsections.

1.3.1 Substrate Mismatch and Growth Difficulties

GaN native free-standing substrates are difficult to produce and very expensive. Pulling a boule of the crystal to slice into epi-wafers is a standard technique in the semiconductor industry, however it is very difficult on a large scale with GaN due to the high temperatures and pressures required [28]. Hydride vapour phase epitaxy

(HVPE), which uses hot metal chloride gasses to react with ammonia can be used to produce small free standing GaN substrates: Using sapphire as a sacrificial substrate, GaN is grown up to 400 μm thick by HVPE. A laser lift off process can then be used to separate this from the sapphire producing free standing GaN, however it has a large wafer bow due to stress in the material and is prone to cracking [29]. This is also a costly and slow process unsuitable for large area fabrication of emitters.

The lack of commercially available free-standing GaN leads to the use of non-native substrates such as sapphire, Si and SiC. The lattice mismatch associated with these materials causes defects and dislocations during growth however, reducing the crystal quality of the material.

The lattice mismatch between SiC and GaN is low, $\sim 3.5\%$, however a SiC substrate is up to twenty times more expensive than sapphire, meaning it is used only for high performance emitters (with associated high cost) [9].

The mismatch between sapphire and GaN is 16%, which causes dislocations in the GaN epi-layer during growth. Because of this various nucleation layer technologies have been developed to improve the crystal quality and allow good quality crystal growth [30]. Large scale 2 to 4 inch sapphire substrates are commercially available for growth of device epi-layers, and are the current technology in use for the majority of InGaN based LEDs.

Six inch silicon substrates are a recently developed GaN growth medium, due mainly to their compatibility with existing fabrication tools and procedures [23]. The use of Si substrates causes problems with wafer bow and GaN epi-layer cracking due to the disparity in thermal expansion between the materials. Novel nucleation methods can reduce the cracking issue and thermal stress, or confine it to the wafer edge where it may cause less issue and lead to greater device yield [31], but Si grown devices are still some way behind LEDs grown on sapphire.

Recent developments with growth on non-polar and semi-polar substrates have allowed improvements in crystal quality and free standing GaN substrates, with small fragments (1 cm x 1 cm) of free standing GaN currently developed with high crystal quality [25]. These substrates are still prohibitively expensive however and unsuitable for mass device fabrication.

Issues with non-native substrate growth on device performance are compounded by the difficulty in growing InGaN layers for the active region in an LED. Indium incorporation is generally poor during growth, leading to the use of lower growth temperatures, which further deteriorates the crystal quality [32]. The use of nitrogen as an indium element carrier gas, versus hydrogen used as a gallium element carrier during MOCVD growth also causes problems when growing thin heterostructures for an LED active region.

These issues are compounded further with increasing In content, where as the

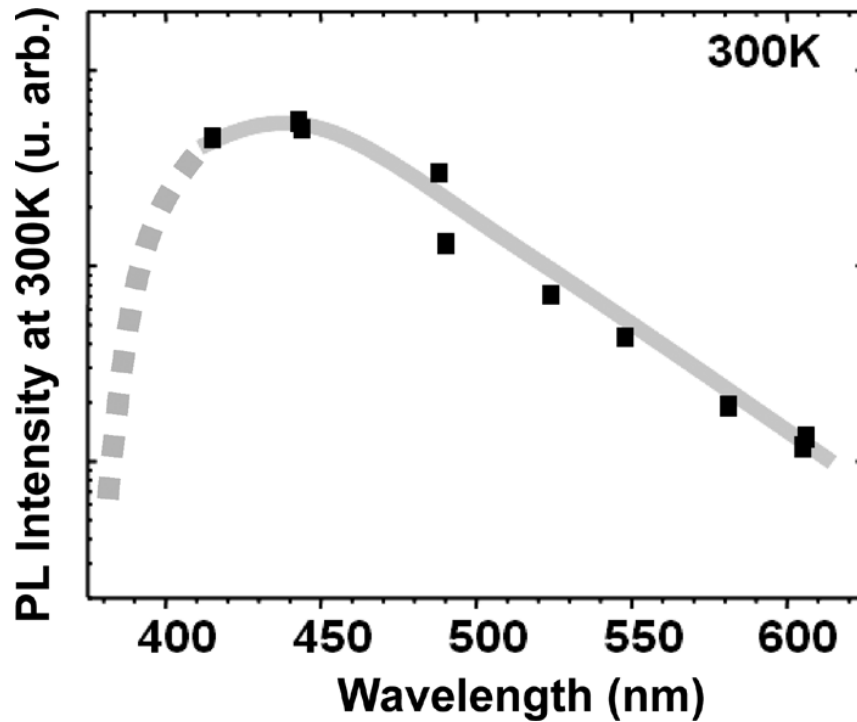


Figure 1.3: Room temperature measurement of PL intensity of InGaN QWs with increased indium content, showing a clear reduction in performance with increasing indium and therefore wavelength. Figure from [32] reprinted with permission.

amount of In in the alloy increases, the emission wavelength increases, and efficiency reduces dramatically - illustrated in Figure 1.3. This is mainly due to phase separation during growth due to changes in temperature and carrier gas, as well as inbuilt polarisation, which is discussed in the following subsection.

1.3.2 The Quantum Confined Stark Effect

The GaN crystal is naturally polarised due to the Wurtzite tetrahedral-covalent crystal structure, and has ionic properties when the gallium and nitrogen atoms are displaced from their equilibrium position. This causes inbuilt spontaneous and piezoelectric polarisation, which can generate strong polarisation fields in the crystal structure. This results in the quantum confined stark effect (QCSE), where an electric field effects the light emission from a QW in a heterostructure, and is discussed in greater detail in chapter 2. QCSE reduces the overlap of the carrier wave functions and hence carrier transition probability in a III-nitride heterostructure, by separating the carriers in a QW. This reduces the radiative efficiency of the emitter, and causes a red shift in the emission energy.

Piezoelectric polarisation is a direct result of the ionic nature of Wurtzite III-nitrides. A GaN crystal will be somewhat strained if grown on sapphire, due to the lattice mismatch between the two materials that moves the Ga and N atoms from

their equilibrium. Growth buffer technology can largely alleviate this issue, however the growth of III-nitride alloys also causes polarisation fields.

Due to the lattice mismatch between GaN, AlN and InN; an alloy of these (for example an InGaN QW in an LED) will show strong piezoelectric effects due to the influence of the underlying GaN material. The InGaN alloy will take the lattice constant of the underlying GaN material, meaning the In, Ga and N atoms are out of equilibrium and produce piezoelectric fields.

Adding to the piezoelectric polarisation due to strain in the crystal structure, Wurtzite material is inherently polarised due to the specific symmetry in the crystal. This spontaneous polarisation also produces internal fields, however piezoelectric fields due to strain tend to be the dominant factor for InGaN alloys.

Developing methods to improve the strain and reduce the piezoelectric fields in InGaN based LEDs is vital for increasing the performance of devices, particularly in the green and longer wavelength region.

1.3.3 Efficiency Droop

III-nitride based LEDs have a tendency to reduce in performance with increased carrier density. This can be observed in the efficiency against input current graph in Figure 1.4 (red trace), where an initial increase in efficiency from a low value reaches a peak, before reducing again at higher injection current - termed efficiency droop [33]. Typically for InGaN based LEDs the onset of this efficiency droop is between 0.1 to 10 A/cm² injection current [34], meaning in almost all lighting applications an InGaN LED will be operating at below its maximum efficiency in this droop region.

The exact cause of this efficiency droop is attributed to several mechanisms, (which are discussed in detail in chapter 2):

- **Carrier Leakage** - Carriers injected into an LED must be confined allowing them time to recombine and emit photons. In an InGaN based LED, carriers can overshoot the active region causing a reduction in efficiency. This is caused by a lack of confinement in quantum structures in an LED, as well as excess thermal energy due to device heating and the applied bias on an LED. This process will occur to some extent at all injection current levels, however when a large current is injected the issues can be compounded due to the larger applied bias and heating effect. Leakage into p-type GaN cladding layers, and polarisation fields (resulting in QCSE) also contribute to this loss of carriers [34].
- **Auger Recombination** - When a large number of excited carriers are confined in a semiconductor, any recombining electron and hole can potentially

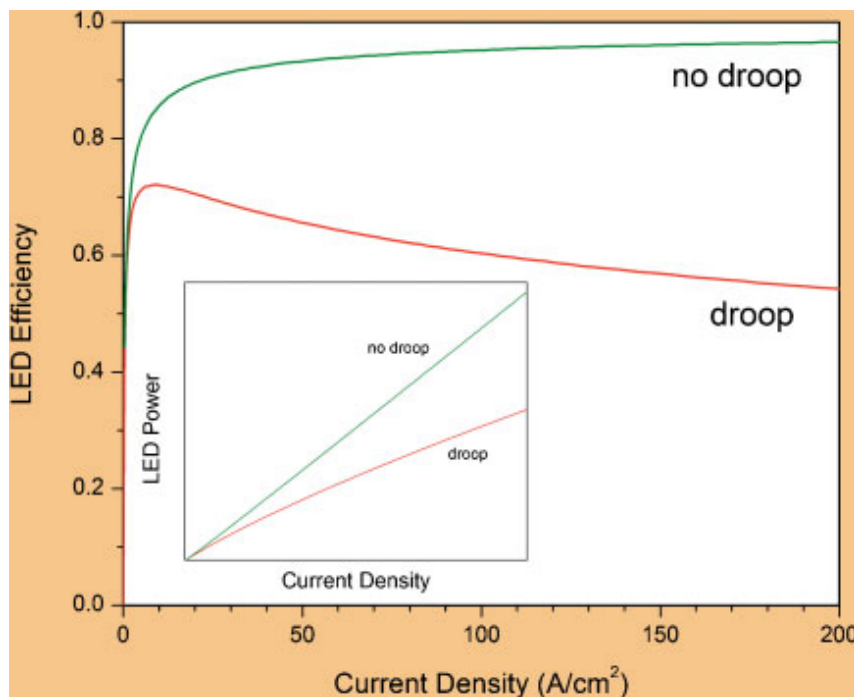


Figure 1.4: Illustration of the efficiency droop issue in III-nitride light emitters reprinted with permission from [33] showing a drop in efficiency at high current density and the resulting reduction in emission power (inset graph).

transfer their energy to a third carrier, instead of emitting a photon. This is termed Auger recombination, and results in carrier loss as the density increases [35]. Recent work has suggested Auger recombination is the dominant mechanism in efficiency droop, and that it is an indirect process assisted by phonon interaction [36].

- **Density Activated Defect Recombination** - A theory proposed by Hader et al. [37] suggests that defects in the GaN/InGaN crystal structure exist at increasing energy levels in the band structure. As a large number of carriers are injected into the system, the density of states in the active region begins to fill, and newly injected carriers must exist at a higher energy. This allows the carriers to interact with defects at these energy levels, increasing the loss of carriers and hence reducing efficiency. This is related to carrier de-localisation in LEDs, a theory suggesting defects are surrounded by a slightly higher bandgap InGaN alloy (with lower indium content), which restricts carriers interacting with them [38].

Improving the high current performance of InGaN based LEDs is vital for all lighting applications, but particularly for saving energy with more efficient emitters producing high lumen per watt values. Understanding the main cause of efficiency droop and developing a solution is therefore very important for designing high performance InGaN emitters.

1.4 Motivation

The aim of the research presented in this thesis is to continue the development of high efficiency InGaN based LEDs, both in the blue wavelength range for improved efficiency white emission using phosphor conversion, and in the green wavelengths where much progress is still to be made. Green wavelength devices are indispensable for both tri-colour white lighting and LED displays, and as lasers in next generation projectors. The “Green Gap” of semiconductor compounds able to efficiently emit green wavelengths has long been a problem, and high power green LEDs are only recently available commercially, at very high cost. Improvements in efficiency and cost are desirable for the current LED market because a small increase in LED efficiency has the potential to allow massive energy savings as LEDs begin to replace traditional lighting technology.

Three main issues are the focus of this work:

- Strain in the crystal structure of GaN and particularly in InGaN/GaN heterostructures.
- Efficiency droop due to carrier leakage, Auger recombination and piezoelectric effects limiting the high performance of III-nitride devices.
- Reduction in efficiency due to reduced crystal quality and hence a large number of non-radiative recombination centres.

The issue of strain and the resulting QCSE in III-nitride emitters causes a major reduction in efficiency, especially in the green wavelength region. The use of nanostructures potentially allows improvements to both extraction efficiency and quantum efficiency of an emitter by reducing strain, as well as improved performance droop characteristics by reducing inbuilt piezoelectric fields. This reduction in the piezoelectric fields and inbuilt strain found after nanostructure fabrication is due to improvements in carrier overlap and transition probability, therefore improving the emission efficiency of a structure.

Improvements found through nanostructuring can also offer a reduction in efficiency droop. Changes in piezoelectric polarisation effects, strain and improving transition probability all allow an improvement in efficiency performance at high carrier densities.

Surface plasmon coupling to InGaN QWs allows further efficiency improvements, by increasing the density of states in the system, and creating a fast radiative recombination process that reduces the number of carriers recombining non-radiatively via defects and dislocations. This exciton-plasmon coupling mechanism has the potential to offer massive improvements in device performance.

Developing these two methods of efficiency enhancement individually should yield real world efficiency improvements that are cost effective to implement. Including improving the radiative recombination rate, and improving the droop in efficiency at high carrier injection.

III-nitride lasers find a wide range of uses from data storage (such as blu-ray) to projector and medical applications, and reducing the lasing threshold is important for efficient laser devices. Pushing the emission wavelength higher into the green spectral region is a recent development with a promising future, as is the use of nano-lasers for lithographic and system-on-chip structures. Development of III-nitride lasers enhanced by nanostructuring and plasmonics is therefore a desirable result with real world applications.

References

- ¹European Commission, *European Commission: Energy Efficiency Directive*.
- ²CREE, *Cree Sets New R&D Performance Record with 276 Lumen-Per-Watt Power LED*, 2013.
- ³T. W. Murphy, “Maximum spectral luminous efficacy of white light”, *Journal of Applied Physics* **111**, 104909 (2012).
- ⁴J. Biard, E. Bonin, W. Carr, and G. Pittman, “GaAs Infrared Source”, 1962 International Electron Devices Meeting **8**, 96 (1962).
- ⁵N. Holonyak and S. F. Bevacqua, “Coherent (Visible) Light Emission From Ga(As_{1-x}P_x) Junctions”, *Applied Physics Letters* **1**, 82 (1962).
- ⁶L. M. Foster and M. Pilkuhn, “Electroluminescence Near Band Gap in Gallium Phosphide Containing Shallow Donor and Acceptor Levels”, *Applied Physics Letters* **7**, 65 (1965).
- ⁷J. I. Pankove, E. A. Miller, and J. E. Berkeyheiser, “GaN blue light-emitting diodes”, *Journal of Luminescence* **5**, 84–86 (1972).
- ⁸F. Steranka, J. Bhat, D. Collins, L. Cook, M. Craford, R. Fletcher, N. Gardner, P. Grillot, W. Goetz, M. Keuper, R. Khare, A. Kim, M. Krames, G. Harbers, M. Ludowise, P. Martin, M. Misra, G. Mueller, R. Mueller-Mach, S. Rudaz, Y.-C. Shen, D. Steigerwald, S. Stockman, S. Subramanya, T. Trottier, and J. Wierer, “High Power LEDs - Technology Status and Market Applications”, *Physica Status Solidi (A)* **194**, 380–388 (2002).
- ⁹S. Nakamura and S. Chichibu, *Introduction to Nitride Semiconductor Blue Lasers and Light Emitting Diodes* (Taylor & Francis, London and New York, 2000).
- ¹⁰Thomas Lettieri and Bill Harsch, *Brighter, Longer Lasting Blue and Green Lasers and LEDs*, technical report (Eagle-Picher Research Laboratory, 2001).
- ¹¹J Orton, *The Story of Semiconductors* (Oxford University Press, 2004).
- ¹²I. Akasaki, H. Amano, Y. Koide, K. Hiramatsu, and N. Sawaki, “Effects of AlN buffer layer on crystallographic structure and on electrical and optical properties of GaN and GaAlN films grown on sapphire substrate by MOVPE”, *Journal of Crystal Growth* **98**, 209–219 (1989).
- ¹³H. Amano, I. Akasaki, and T. Kozawa, “Electron beam effects on blue luminescence of zinc-doped GaN”, *Journal of Luminescence* **41** (1988).
- ¹⁴H. Amano, M. Kito, K. Hiramatsu, and I. Akasaki, “P-Type Conduction in Mg-Doped GaN Treated with Low-Energy Electron Beam Irradiation (LEEBI)”, *Japanese Journal of Applied Physics* **28**, 2112–2114 (1989).

- ¹⁵S. Nakamura, “High-power InGaN/AlGaIn double-heterostructure blue-light-emitting diodes”, in Proceedings of international electron devices meeting 94. technical digest (1994), pages 567–570.
- ¹⁶T. Hanada, “Basic Properties of ZnO, GaN, and Related Materials”, Oxide and Nitride Semiconductors, Processing, Properties and Applications (2009).
- ¹⁷H. Amano, T. Asahi, and I. Akasaki, “Stimulated Emission Near Ultraviolet at Room Temperature from a GaN Film Grown on Sapphire by MOVPE Using an AlN Buffer Layer”, Japanese Journal of Applied Physics **29**, 205–206 (1990).
- ¹⁸S. Nakamura, M. Senoh, S.-i. Nagahama, N. Iwasa, T. Yamada, T. Matsushita, Y. Sugimoto, and H. Kiyoku, “Room-temperature continuous-wave operation of InGaN multi-quantum-well structure laser diodes”, Applied Physics Letters **69**, 4056 (1996).
- ¹⁹S. Masui, Y. Matsuyama, T. Yanamoto, T. Kozaki, S.-i. Nagahama, and T. Mukai, “365 nm Ultraviolet Laser Diodes Composed of Quaternary AlInGaIn Alloy”, Japanese Journal of Applied Physics **42**, 1318–1320 (2003).
- ²⁰T. Kozaki, H. Matsumura, Y. Sugimoto, S.-i. Nagahama, and T. Mukai, “High-power and wide wavelength range GaN-based laser diodes”, Novel In-Plane Semiconductor Lasers V **6133**, edited by C. Mermelstein and D. P. Bour, 613306–12 (2006).
- ²¹A. Avramescu, T. Lermer, J. Müller, C. Eichler, G. Bruederl, M. Sabathil, S. Lutgen, and U. Strauss, “True Green Laser Diodes at 524 nm with 50 mW Continuous Wave Output Power on c -Plane GaN”, Applied Physics Express **3**, 061003 (2010).
- ²²S. Council, *Brighter, Energy Efficient Street Lights coming soon...* 2012.
- ²³S. Bush, *Plessey GaN-on-silicon LED sampling*, 2013.
- ²⁴Z. Liliental-Weber, “GaN grown in polar and non-polar directions”, Opto-Electronics Review **12**, 339–346 (2004).
- ²⁵Q. Sun and J. Han, “Heteroepitaxy of Nonpolar and Semipolar GaN”, in *Gan and zno-based materials and devices* (Springer Berlin / Heidelberg, 2012).
- ²⁶K. Takahashi, A. Yoshikawa, and A. Sandhu, *Wide Bandgap Semiconductors* (Springer Berlin / Heidelberg, 2007).
- ²⁷M. R. Krames, O. B. Shchekin, R. Mueller-Mach, G. O. Mueller, L. Zhou, G. Harbers, and M. G. Craford, “Status and Future of High-Power Light-Emitting Diodes for Solid-State Lighting”, Journal of Display Technology **3**, 160–175 (2007).
- ²⁸M. Bockowski, “Bulk growth of gallium nitride: challenges and difficulties”, Crystal Research and Technology **42**, 1162–1175 (2007).

- ²⁹K. Motoki, T. Okahisa, S. Nakahata, and K. Uematsu, “Preparation of 2-inch GaN substrates”, Proceedings of the 21st century COE Symposium, 32–37 (2003).
- ³⁰T. Wang, J. Bai, P. J. Parbrook, and a. G. Cullis, “Air-bridged lateral growth of an Al[0.98]Ga[0.02]N layer by introduction of porosity in an AlN buffer”, Applied Physics Letters **87**, 151906 (2005).
- ³¹S. Raghavan and J. Redwing, “Growth stresses and cracking in GaN films on (111) Si grown by metalorganic chemical vapor deposition. II. Graded AlGaIn buffer layers”, Journal of Applied Physics **98**, 023515 (2005).
- ³²N. Grandjean and M. Ilegems, “Visible InGaIn/GaN Quantum-Dot Materials and Devices”, Proceedings of the IEEE **95**, 1853–1865 (2007).
- ³³J. Piprek, “Efficiency droop in nitride-based light-emitting diodes”, Physica Status Solidi (A) **207**, 2217–2225 (2010).
- ³⁴M.-H. Kim, M. F. Schubert, Q. Dai, J. K. Kim, E. F. Schubert, J. Piprek, and Y. Park, “Origin of efficiency droop in GaN-based light-emitting diodes”, Applied Physics Letters **91**, 183507 (2007).
- ³⁵Y. C. Shen, G. O. Mueller, S. Watanabe, N. F. Gardner, A. Munkholm, and M. R. Krames, “Auger recombination in InGaIn measured by photoluminescence”, Applied Physics Letters **91**, 141101 (2007).
- ³⁶E. Kioupakis, P. Rinke, K. T. Delaney, and C. G. Van de Walle, “Indirect Auger recombination as a cause of efficiency droop in nitride light-emitting diodes”, Applied Physics Letters **98**, 161107 (2011).
- ³⁷J. Hader, J. V. Moloney, and S. W. Koch, “Density-activated defect recombination as a possible explanation for the efficiency droop in GaN-based diodes”, Applied Physics Letters **96**, 221106 (2010).
- ³⁸A. Kim, W. Gotz, D. Steigerwald, J. Wierer, N. Gardner, J. Sun, S. Stockman, P. Martin, M. Krames, R. Kern, and F. Steranka, “Performance of High-Power AlInGaIn Light Emitting Diodes”, Physica Status Solidi (A) **188**, 15–21 (2001).

Background

2.1 Properties of III-Nitrides

2.1.1 Crystal Structure

Stable III-nitride materials generally crystallise in the Wurtzite form, although rock-salt and zinc-blende structures can also be formed using cubic substrates [1]. The Wurtzite structure consists of stacked hexagonal lattices containing one type of atom, either metal (Ga, In, Al) or nitrogen, separated by a lattice constant a . The planar layers are stacked in the 0001 direction, termed the c -axis, as illustrated in Figure 2.1, and the lattice constants of each material are listed in Table 2.1. The preferred growth direction is on the Ga-polarity face, as the N-polarity direction tends to show reduced crystal quality [1].

2.1.2 Electrical and Chemical Properties

III-nitrides such as GaN are chemically stable, and have a high melting point. Etching and processing is therefore difficult, with chemicals such as KOH, NaOH or H_2SO_4 at high temperature able to etch defects in GaN, but with reduced etch rate as crystal quality increases. This makes GaN attractive as electrical devices can withstand extreme conditions that other semiconductors cannot.

| Material | Bandgap (eV) | Permittivity (ϵ_r) | Refractive Index | Lattice Constants (\AA) |
|----------|--------------|-------------------------------|------------------|------------------------------------|
| GaN | 3.39 | 8.9 | 2.49 | a=3.189, c=5.186 |
| InN | 0.65 | 15.3 | 2.90 | a=3.533, c=5.693 |
| AlN | 6.22 | 8.5 | 2.18 | a=3.112, c=4.982 |

Table 2.1: Table showing some important properties of III-Nitrides. All values are obtained at room temperature and refractive index is measured at a wavelength of 450 nm [2, 3].

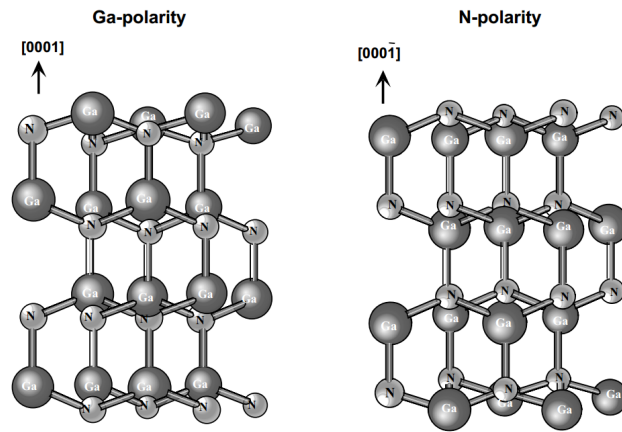


Figure 2.1: Stick and ball diagram of the GaN Wurtzite crystal structure, showing Ga- and N- polarity growth. Figure from [1] reprinted with permission.

| Material | Bandgap (eV) | Electron Mobility (cm ² /Vs) | Electron Velocity (x10 ⁷ cm/s) | Breakdown Field (MV/cm) | Dielectric Constant ϵ_r |
|----------|--------------|---|---|-------------------------|----------------------------------|
| GaN | 3.5 | 900 | 2.7 | 3.3 | 9.0 |
| SiC (3C) | 3.26 | 700 | 2 | 2 | 10 |
| GaAs | 1.42 | 8500 | 2.1 | 0.4 | 12.5 |
| InP | 1.35 | 10000 | 2.3 | 0.5 | 12.8 |
| Si | 1.1 | 1500 | 1 | 0.3 | 11.8 |

Table 2.2: Table showing important electrical properties of III-V semiconductors including GaN and other semiconductor materials Si and SiC.

Table 2.2 details electrical properties of GaN and other related semiconductor materials [2]. The bandgap of GaN is high, allowing it to switch larger voltages and withstand higher temperatures as well as operate throughout the visible wavelength emission region with the incorporation of InGaN alloys.

The carrier mobility of GaN is high for a wide bandgap semiconductor, and is higher than SiC with a similar bandgap. It also has a large 2DEG electron density making GaN useful for power electronics applications. The thermal conductivity of GaN is also high compared to many semiconductors, allowing it to withstand high temperatures and dissipate heat well.

The breakdown voltage of GaN is high, meaning it is suitable for IMPATT and other diode applications, and can withstand large fields and electrostatic effects. Finally the relative permittivity is low compared to other related semiconductors, further reducing charge build up and the effects of electrostatics [4].

GaN has a high background electron concentration, as high as $10^{16} - 10^{18}$ cm³,

due to defects and vacancies acting as carrier donors in the material. Consequently, GaN is unintentionally n-type, meaning doping levels must be high to overcome this.

N-type GaN with Si used as a donor was quickly realised early in GaN's development, and is reasonably easy to achieve with good conductivity due to a low donor activation energy of ~ 25 meV [5]. Basic p-doped GaN was achieved in the 1970's [6] however good conductivity proved difficult, due to a high acceptor activation energy of 170 meV [7]. A strong chemical bond also exists between the p-type acceptor atom Mg and hydrogen from the ammonia NH_3 gas used as a nitrogen source in normal GaN MOCVD growth. The Mg acceptor is effectively deactivated by a hydrogen atom, however the acceptor can be reactivated with a high temperature anneal or a low energy electron beam, increasing the conductivity of the p-type material and allowing good p-n junctions to be formed [8, 9]. P-type GaN using Mg produces deep acceptors however, which tend to be only approximately 1% activated. This leads to the p-type material being the limiting factor in GaN based p-n junctions in terms of electrical performance [4].

2.1.3 Band Structure

The interband processes of absorption and emission of photons in a semiconductor result from the discrete conduction band (CB) and valence band (VB) levels of the material. In such a system an electron may be promoted to a position in the upper CB by absorption of an incoming photon of energy hw . The conditions for this absorption to occur are that the energy of the photon is larger than the bandgap of the semiconductor, and that an empty state is available in the CB, so as not to break Pauli's exclusion principle [10]. The energy of the excited electron is given by equation 2.1, where E_i is the energy of the electron in the valence band (lower level), E_f is the energy of the upper conduction band (excited state) and hw is the energy of the absorbed photon.

$$E_f = E_i + hw \quad (2.1)$$

From this equation, which arises due to the conservation of energy principle, it can be seen that a minimum energy value of $E_f - E_i$ is given. This value, E_g is the bandgap of the system, and a photon with energy below this range would not be absorbed by the semiconductor (ignoring trapping effects). Above this energy, where $hw > E_g$, an absorption threshold is passed and electrons are excited to the CB. This absorption spectrum is from $hw > E_g$ to a potential upper limit at very high energy given by the structure, and means a semiconductor is transparent below its bandgap and opaque above this [10].

The point in the valence band, E_i that is left vacant by the electron is termed

a hole, which is a positive charge carrier and generally has lower mobility than an electron. One absorbed photon will therefore create one electron-hole pair in a band structure, and, upon recombination of these two carriers, a photon of energy E_g can be re-emitted.

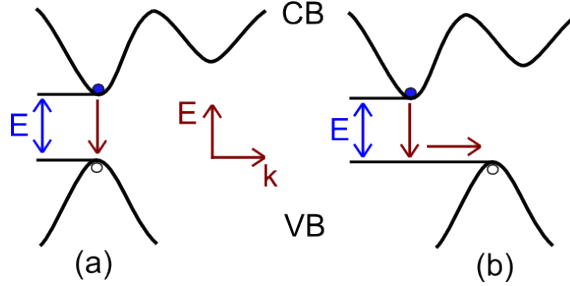


Figure 2.2: Direct (a) and indirect (b) bandstructure illustrated with conduction and valence band (CB and VB) close to $E=0$ and $k=0$ (where energy vs momentum is depicted as E vs k).

The band edge E_g recombination of a semiconductor, when an electron relaxes from the CB to VB, can be direct or indirect, as illustrated in Figure 2.2. In a typical band structure an excited electron and hole will relax to the band edges to a minima in the CB and maxima in the VB. If these points are vertically aligned in k -space, meaning they have the same momentum, recombination occurs in a direct mode and a photon can be emitted. If the minima in CB and maxima in VB do not align in k -space, a change in momentum is required before an electron and hole can recombine. This recombination is often assisted by a phonon, and the semiconductor is described as being indirect [10].

The bandgaps of InN, GaN and AlN are ~ 0.7 eV [13], 3.4 eV [14] and 6.2 eV [15] respectively, as listed in Table 2.1. The direct bandgap Wurtzite band structure of

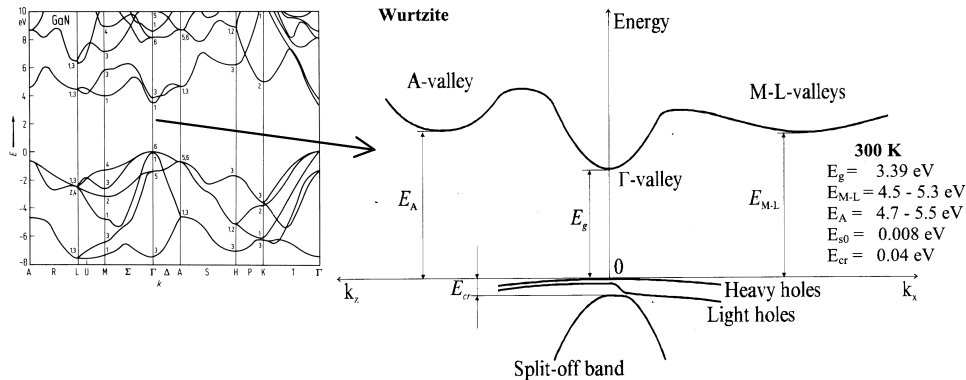


Figure 2.3: (Left) Wurtzite GaN band structure calculated by empirical pseudo potential calculations from [11]. (Right) The section of the Wurtzite GaN band structure of most interest in this work, showing the in-line maxima and minima that cause GaN to have a direct bandgap. Figure from [12] reprinted with permission.

each is complex, as can be seen in Figure 2.3 (right) [11]. The allowed energy levels of electrons and holes form various maxima and minima, and crucially for GaN and related III-nitride alloys, the highest maximum and lowest minimum points are aligned, forming a direct bandgap.

The important section of the complex band structure, the direct bandgap maxima and minima that give rise to the desirable optical properties of GaN, are illustrated in Figure 2.3 (left) [12]. The Γ valley has a CB minima above a split VB maxima, which exists in three levels: the heavy hole, light hole and split-off bands, as a result of the crystal fields and spin-orbit coupling in the lattice.

2.1.4 Ternary Alloy III-Nitride Materials

As mentioned previously, the bandgap energy of the III-nitrides spreads from InN at ~ 0.7 eV to AlN at ~ 6.2 eV. The bandgap of a III-nitride semiconductor can in theory be engineered to any value in this range, by incorporating different quantities of each material as an alloy. Quaternary alloys can also be formed, however for the basis of this thesis ternary alloys will be discussed. Both InGaN and AlGaN alloys are used in the production of optical emitters, where AlGaN produces UV emitters with shorter wavelength than GaN due to its higher bandgap, and InGaN produces emitters in the visible region with longer wavelength than the GaN bandgap. The bandgap energy of InGaN or AlGaN can be calculated using equation 2.2. Where x is the proportion of In or Al in the alloy, $E_{g(\text{GaN})}$ and $E_{g(\text{AlN,InN})}$ are the bandgaps of GaN and AlN or InN, and b is the bowing parameter [1].

$$E_{g(\text{AlGaN,InGaN})} = (1 - x)E_{g(\text{GaN})} + xE_{g(\text{AlN,InN})} - bx(1 - x) \quad (2.2)$$

2.1.5 Carrier Recombination

If a photon is absorbed by a semiconductor, creating an electron hole pair (or carriers are injected into an LED) they can recombine via several paths. The separation of the electrons in the conduction band and holes in valence band is broadly the bandgap of the semiconductor E_g , however small changes in this energy result as the carriers occupy various points near the band edges of the bandstructure, or recombine via mid band levels. Several recombination pathways exist for III-nitride materials as a result of the crystal structure and potential doping of the material, six main paths are illustrated in Figure 2.4 [1].

- Path 1 is band to band recombination between electrons in the CB and holes in the VB, resulting in an emitted photon at the band gap energy of the material.

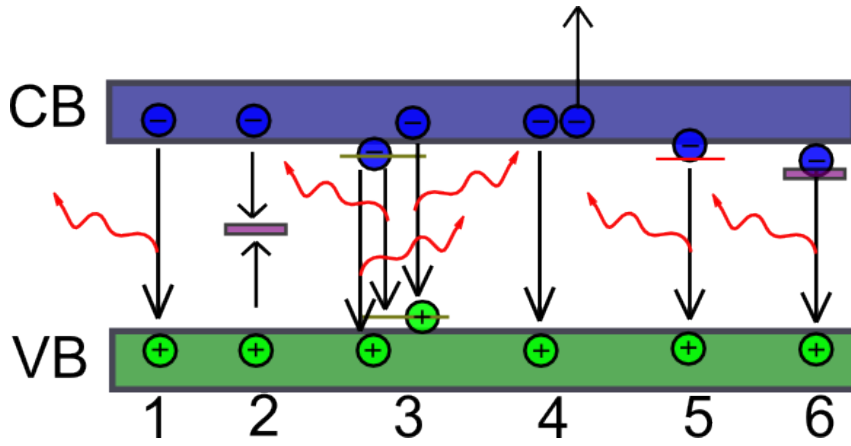


Figure 2.4: Typical III-nitride recombination paths.

- Path 2 is a defect level transition, where the carriers recombine via a defect and lose energy non-radiatively (or by emission of a photon at much lower energy).
- Path 3 is emission related to dopants, either donor to acceptor emission, or free to bound (in donor or acceptor state). If the semiconductor material is doped, the dopant atoms may introduce a level below or above the CB and VB respectively. Recombination via these states results in a photon of lower energy than the original material band-gap.
- Path 4 is Auger recombination, and only applicable at large excited carrier density. The energy from a recombining electron and hole acts to promote a third carrier (either an electron higher up in the CB or a hole lower down in the VB) to a higher energy instead of emitting as a photon.
- Path 5 is exciton recombination, where an electron and hole are excitonically bound due to coulomb interactions. The excitons may be free to move through the structure, and recombine emitting a photon at slightly reduced energy. For GaN based structures a 25 meV reduction in the bandgap energy is observed when recombination is via excitons.
- Path 6 is recombination via a phonon interaction, resulting in photon emission at a slightly reduced energy to the material band-gap.

Band to band radiative recombination, pathway 1 in Figure 2.4, results in a photon with the same energy as the bandgap $E_g = (hc)/\lambda$ while the other pathways result in a decrease in this energy, or lack of a photon emission.

Exciton recombination, path 5 in Figure 2.4, is a result of the Coulomb attraction between carriers with different charge in a semiconductor, such as an electron and hole. As a generated electron and hole are created at the same point, or can migrate

to a similar point in space, they are attracted together by their differing charge. This increases the probability of an optical transition, and therefore the light emission efficiency in a structure. An exciton is a neutrally charged system of electron and hole bound together, with the ability to move freely in a semiconductor (allowing both electron and hole to remain coupled as they move) [10]. These free moving Wannier-Mott excitons may result in the majority of light emission from GaN and other III-nitrides. This is due to a high exciton binding energy in the material of 25 meV, which is similar to the room temperature thermal activation energy (kT), and allows stable excitons and hence recombination via them at room temperature [16]. The exciton binding energy is calculated by approximating the electron-hole pair of an exciton to a hydrogen atom, and using the Bohr model, where the large effective mass of an electron and hole in III-nitrides, and high dielectric constant of the semiconductor result in the large exciton binding energy.

Recombination of excitons can occur at reduced energy via the interaction with a phonon as described in Figure 2.4 path 6. A phonon can take many forms, including as acoustic or optical, and within these forms longitudinal and transverse modes. Optical phonons are specifically referred to in this work, and arise when the atoms in a crystal have different mass (Ga and N in this case), and have opposing oscillation, resulting in the absorption of an infra-red photon by the lattice.

III-nitride structures may emit some yellow wavelength luminescence, due to optical transitions between defects in the crystal structure. This emission is about half the bandgap emission energy of GaN, and tends to be between a defect acting as a deep donor-like state allowing a transition from the mid band gap to emit at ~ 2 eV [1]. Typical causes are gallium or nitrogen vacancies in the Wurtzite crystal structure [17] and impurities such as carbon unintentionally introduced during growth or post processing [18].

If a structure is fabricated into an LED (and has a bias applied) then a further method of loss is by carrier leakage. In this situation, as the conduction and valance band are shifted by the applied bias, carriers can gain enough energy to overcome the barrier at the edge of the QW and leak out, where they are then lost due to the applied field. This is illustrated in Figure 2.5.

2.1.6 LED Structures

LEDs use a p-n junction to inject carriers into a material, where they recombine to emit photons. When an n-type material, doped to provide an excess of electrons, is combined with p-type material, doped to have a high hole concentration, a movement of carriers occurs as holes and electrons from each material move across the junction. As carriers move, the dopant atoms in each material lose their free carriers, creating

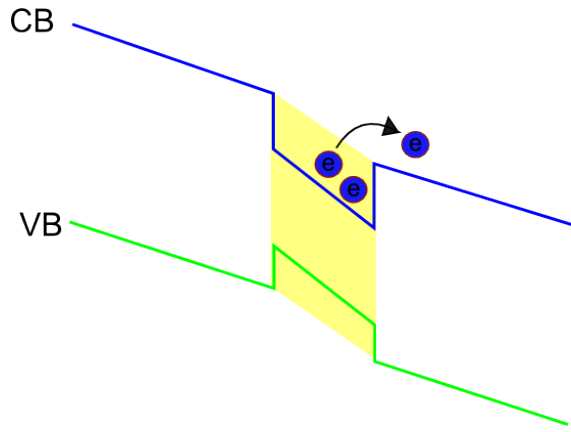


Figure 2.5: Carrier leakage in a biased QW. As the bands shift due to applied bias, electrons in a QW can overcome the barrier and be swept down the slope and out of the device, representing a loss in efficiency.

an area of ions and a build up of charge. This creates an electric field across the junction where carriers are depleted, and any carriers thermally generated in this region will move to the corresponding doped region due to the field. This system is self limiting because as the electric field becomes large, further carrier movement across the junction is restricted and an equilibrium is reached. Illustrated in the upper diagram of Figure 2.6 is the balanced p-n junction without an externally applied bias, where it is clear that the Fermi levels E_F of each material have aligned, producing a change in the band structure creating a potential barrier eV_o .

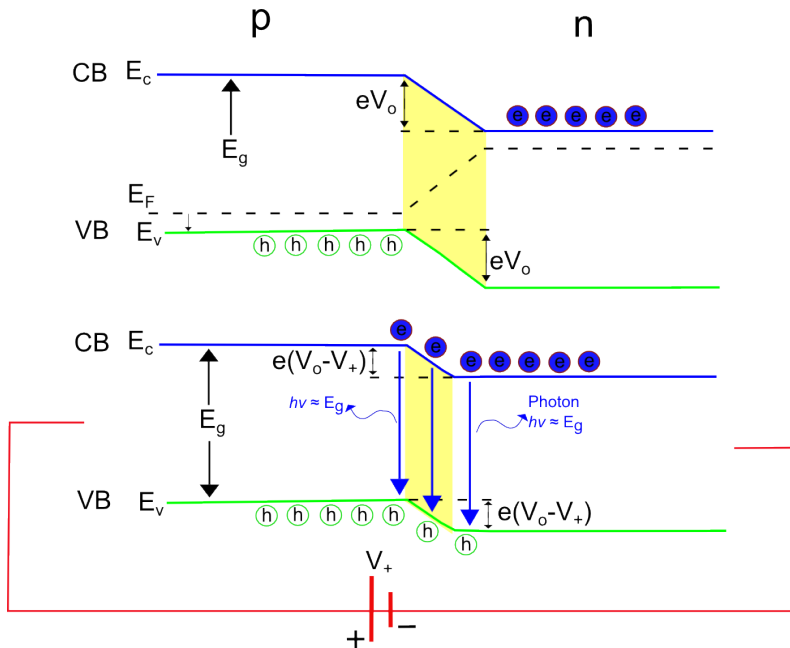


Figure 2.6: Band structure of an LED p-n junction at equilibrium in the upper diagram and with an applied bias V_+ in the lower diagram.

If a bias V_+ is applied to the device as illustrated in the lower diagram in Fig-

ure 2.6, the depleted region thickness and potential barrier height eV_o are reduced by the bias. As carriers are injected into the system, they combine with the ions previously stripped of their carriers to create the barrier and lower the in built potential. Further injected carriers can begin to overcome the potential barrier, and re-combine to emit as photons in the active region (yellow region in Figure 2.6).

A double heterostructure where thin areas of a lower bandgap material (QWs) are sandwiched between higher bandgap materials allows carrier confinement in the depletion region, reducing the leakage of carriers over the potential barrier and allowing a tailored emission spectra with changing bandgap. A GaN based LED emitting in the visible wavelength region will normally utilise InGaN QWs as the lower bandgap material used for confining carriers and emitting photons. Changing the In content of the layer allows the bandgap to be changed resulting in a change of emission wavelength [19].

Developments in LEDs have led to light output in the majority of the visible spectrum, with GaN based structures currently emitting between UV and green having been commercialised. Various LED structures exist, although a limitation with GaN based LEDs is the insulating substrate, such as sapphire, generally requiring a top down approach to fabrication. More complex vertical LED structures have been developed, especially grown on substrates such as Si which are easy to remove allowing a rear contact to be formed.

2.1.7 Stimulated Emission and Lasing

The radiative recombination mechanisms so far described are termed spontaneous emission paths. An excited state, such as an electron excited to the CB has a tendency to relax and lose its excess energy according to statistical physics. As such, excited carriers in a CB recombine at some point without influence from an external field and emit a photon with energy close to the bandgap of the material.

Stimulated emission is described as a strongly super-linear increase in luminescence output with increasing excitation power, usually above an observable threshold [21]. A narrowing of the emission spectra accompanies this non-linear increase, often with observed laser modes due to cavity confinement. These features are illustrated in Figure 2.7, showing stimulated emission from an AlGaIn based emitter at 340 nm developed at Sheffield. Typically a stimulated emission spectra appears as a sharp peak with very narrow linewidth. Due to the stimulated nature of the emission, this narrow spectral peak rises quickly with increasing carrier density, resulting in a distinct threshold between spontaneous and stimulated emission in an integrated intensity against carrier density plot as observed in Figure 2.7.

The main mechanism behind stimulated emission is the process of an excited

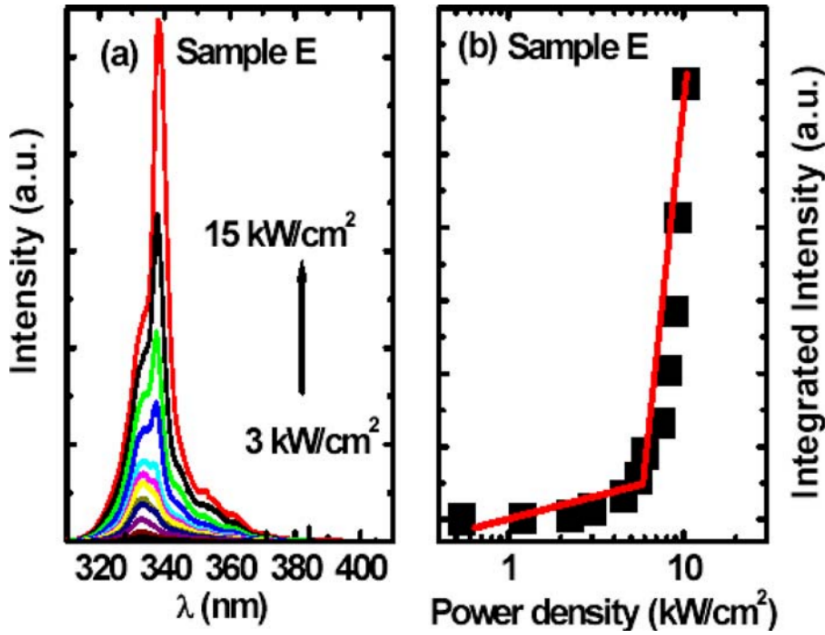


Figure 2.7: (Left) Stimulated emission of an AlGaIn sample, characterised by an observed shoulder peak with narrow linewidth that increases non-linearly with increasing excitation power. (Right) Integrated PL intensity against input power density showing a clear difference between spontaneous and stimulated emission regimes, characterised by a threshold seen as a kink in emission with increased excitation power. Reprinted with permission from [20].

carrier being driven into recombination by an external electromagnetic field. A simple case is that of an argon based laser, presented in Figure 2.8: An initial population of argon exists in a ground state, or unexcited condition. An input of energy promotes the ions to an upper energy level, where they may relax at a random time to spontaneously emit a photon. Placing this system into a cavity, where photons are continually reflected through the medium, the interaction between an existing photon and excited state stimulates the relaxation to a photon with the same wavelength, phase and direction. As pump energy E increases, the transition between spontaneous emission and stimulated emission occurs as population inversion is reached - In this case, the majority of the gain medium is in an excited state, and photon emission is stimulated if the gain medium is in a cavity. The cavity or optical resonator is created using two highly reflective mirrors, producing standing wave patterns or modes at certain resonant frequencies. The modes are generated due to the interference of light as it reflects inside the cavity, by constructive and destructive interference. The creation of these longitudinal modes at specific frequencies allows light of the same frequencies to oscillate between the mirrors, and if the allowed frequencies match to the emission frequency bandwidth of the gain

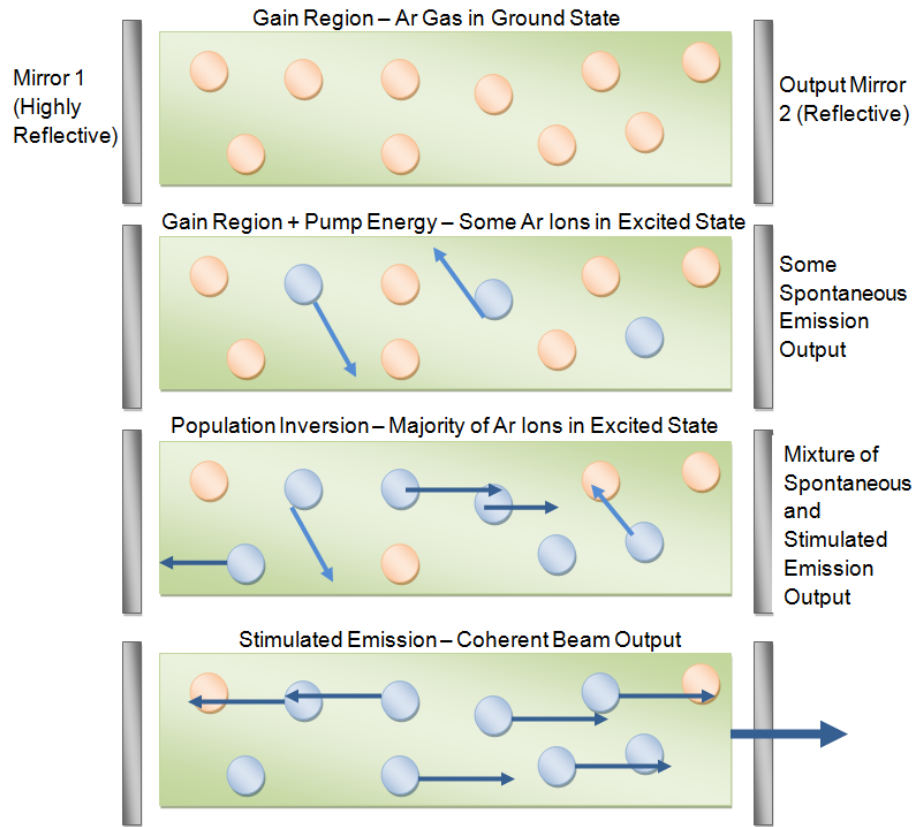


Figure 2.8: Diagram of the operation of an Ar ion based laser.

medium, lasing can take place, creating a stable mode with integer number of wavelengths resulting in a laser mode. This is illustrated in Figure 2.9. The longitudinal mode separation $d\nu$ is given by the cavity length L , where $d\nu = c/2L$, and c is the speed of light. A small change in cavity length L changes the mode spacing, and can result in mode-hopping as a cavity heats up and expands, resulting in changing output laser wavelength. The equation can be modified if the optical gain region is not the full length of the cavity by changing L , for example in a semiconductor laser where the gain region may be a thin active region inside a larger reflective cavity. An ideal laser will be single mode, where one longitudinal mode results in the emission of a single frequency from the laser gain spectrum. In reality many lasers emit in a multi-mode form, where several longitudinal modes produce several laser lines at different frequency due to laser gain spectral overlap.

One mirror in the cavity is usually designed to be as reflective as possible, while the other is intentionally less reflective, to allow generated light out of the system. The high reflectance of the cavity results in a large photon density in the structure, and allows stimulated emission to be the dominant process over spontaneous emission. The fundamental transverse mode of a laser is a Gaussian profile, termed TEM_{00} . As the beam will have some form of divergence or convergence, the optics and transverse limitations in the system cause increasing order modes, presented as

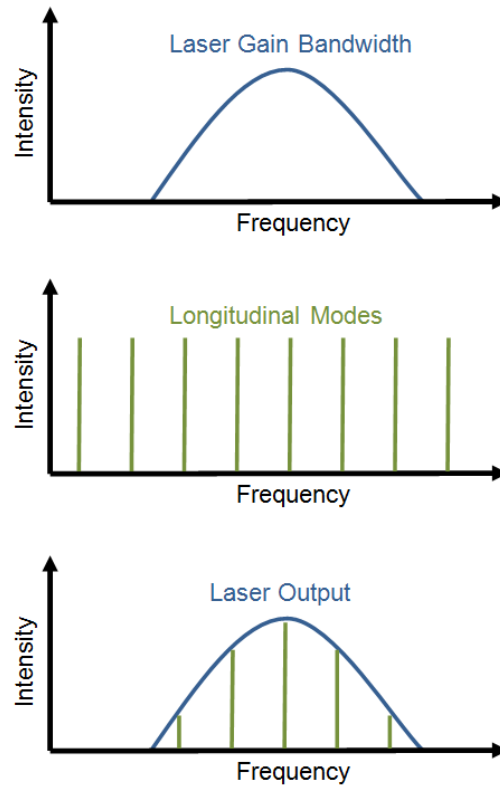


Figure 2.9: Diagram of the relationship between gain medium bandwidth and allowed frequencies generated in an optical resonator.

either rings (doughnuts) or lobes.

A similar mechanism exists in a semiconductor, where an incoming photon of certain energy can cause the relaxation of an excited electron in the CB. In this situation, an increase in the photon number is observed as light interacts with the atoms in the semiconductor, leading to optical amplification.

In a system exhibiting spontaneous emission below the laser threshold, if photons of energy ν close to the bandgap energy $h\nu$ enter a material, they are absorbed and promote carriers from the VB to CB, resulting in attenuation of the incoming light.

If the number of carriers present in the CB exceeds that of the VB, the result is population inversion. In this case incoming photons are not absorbed, and instead stimulate the emission of carriers from the CB, giving rise to an optical gain and non-linear increase in emission. Lasing can result if a cavity is present in the system, and the generated photons can repeatedly pass through the active region.

Illustrated in Figure 2.10 is the stimulated emission mechanism for a typical semiconductor. An incoming photon with specific energy, polarisation and phase stimulates an excited electron at a similar energy to recombine as a photon. The new photon has exactly the same energy, polarisation and phase as the initial photon, creating extremely coherent light output from the system.

An example of a semiconductor laser with quantum wells as a gain medium is a

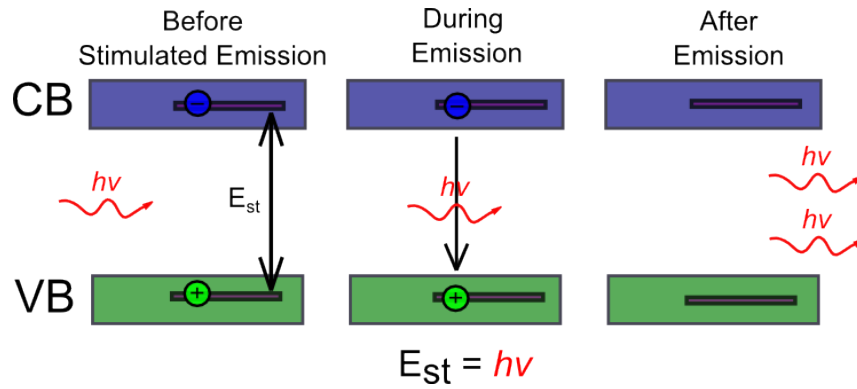


Figure 2.10: Diagram of the stimulated emission mechanism in a semiconductor. An excited electron at energy E_{st} is caused to recombine by an incoming photon with the same energy. The resulting new photon has the same energy, phase and polarisation as the incident photon.

vertical cavity surface emitting laser (VCSEL). In this structure, Bragg reflectors are grown below and above the QW active gain region, creating a cavity containing the QWs. The gain region and reflector cavity are very thin in this structure, which can create problems with multiple transverse modes but can allow single mode operation at specific frequencies [22].

2.2 III-Nitride MOCVD Growth

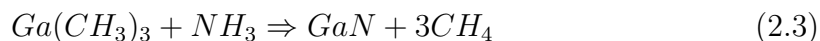
Due to the high cost of native substrates, the main substrate currently used in commercial III-nitride growth is sapphire, however other substrates such as SiC and Si can be used and have recently been commercialised [23]. The use of non native substrates often results in reduced crystal quality due to a lattice mismatch, which introduces dislocations during growth. Sapphire tends to provide the best balance between cost and crystal quality of the resulting GaN material, with an effective lattice mismatch between GaN and sapphire of 16% [24]. The real lattice mismatch is much larger, however the resultant GaN structure grows rotated by 30° to align with the sapphire hexagonal oxygen atoms allowing this 16% mismatch.

The two main growth methods of III-nitrides are by vapour phase epitaxy (VPE) or molecular beam epitaxy (MBE) although other growth methods such as reactive sputtering are possible but not readily used [4]. The basic operation of MBE is of the physical deposition of a thin film where, under high vacuum, a beam of atoms or molecules can be directed to a substrate at high temperature. The atoms in the beam react at the surface and build up an epitaxial film [25]. This process is an excellent way of accurately controlling the structure of a sample as a reduced temperature is used during growth compared to MOVPE (due to available nitrogen atomic sources instead of the need to crack ammonia), however it is slow and expen-

sive when compared with MOVPE techniques, and is therefore rarely commercially viable [4].

In a VPE deposition system, chemical vapours are transported to a chamber with heated substrate. The vapours carry the required substances and react to form a crystal at the substrate, with the remaining chemicals being extracted. Two main methods are used for growing GaN and other III-nitrides; hydride vapour-phase epitaxy (HVPE), which uses a halide containing gas as a carrier mechanism, and metal-organic vapour-phase epitaxy (MOVPE or metal-organic chemical vapour deposition - MOCVD), which uses organometallic carrier gasses. The majority of the samples used in this thesis, as well as commercially available LEDs are grown using a form of MOCVD.

The use of organometallic growth techniques originated in GaAs in the late 1960s, and became the leading technique for growing III-V compounds due to its scalability and commercial potential. For GaN and other III-nitride material growth, the precursors used are liquids trimethylgallium (TMGa) and trimethylaluminium (TMAI), and solid trimethylindium (TMIn). These substances are stored in a bubbler, where a carrier gas such as hydrogen is bubbled through and can transport the precursor vapour to a heated chamber for reaction with a hydride vapour such as ammonia (NH_3). The basic GaN reaction in MOCVD is described by equation 2.3:



The rate of growth and composition of a structure can be accurately controlled by controlling the flow rate of the group III alkyls and group V hydrides to create binary, ternary or quaternary compounds incorporating In, Ga, Al and N. Controlling temperature is also important when growing alloys, and typically for a GaN/InGaN heterostructure (as used in this work) two types of temperature control are available. The first method is to grow the GaN underlying layer at high temperature, followed by reducing the temperature to grow both the InGaN and GaN thin regions to form MQW structures. This produces uniform quantum wells, but poor quality GaN barriers as they are grown at a low temperature [7]. The second method involves cycling the temperature, where after the underlying GaN is grown, the temperature is ramped down for InGaN growth and ramped up for GaN growth. In a MQW structure this cycle will be performed multiple times, and provides good quality GaN barrier layers. The InGaN layers however will decompose during the ramping up of temperature, where the In is desorbed with higher temperature leaving non-uniform quantum wells. This well width fluctuation may actually improve performance, by confining carriers and reducing the likelihood of a carrier recombining with a non-radiative recombination centre [26].

Doping of a III-nitride material grown by MOCVD is readily accomplished using either metalorganic precursors such as bis(cyclopentadienyl) magnesium (CP_2Mg) for p-type doping or hydrides such as silane (SiH_4) for n-type doping [7]. Introducing dopants can cause a low energy recombination path in InGaN LEDs, where blue or yellow luminescence can result from recombination via dopants [19].

MOCVD Nucleation Mechanisms

Growth of GaN by MOCVD on sapphire begins with a high temperature ramp along with introduction of ammonia (NH_3), which breaks down into hydrogen and nitrogen on contact with the substrate (Al_2O_3). The nitrogen reacts with the aluminium face of the substrate in a nitridation process, which produces a thin layer of AlN, while the hydrogen gas is flushed out by the reactor gas flow.

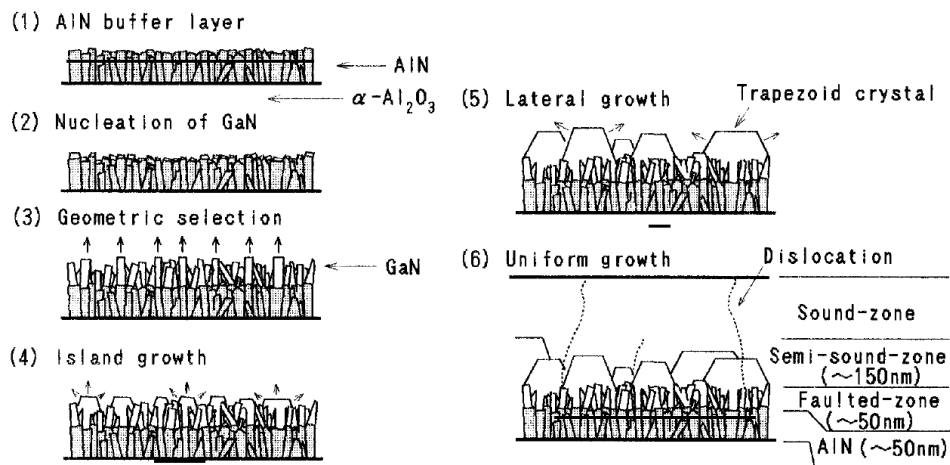


Figure 2.11: Conventional GaN growth mechanism using an AlN buffer layer reprinted with permission from [27].

The standard nucleation mechanism used in GaN structures grown on sapphire is a two step method first developed in MBE growth [28]. Before this, difficulties with nucleation of GaN on sapphire resulted in large dislocation density, buried conductive layers and high background doping levels. The two step method consists of initially growing low temperature AlN on the sapphire substrate, before growing the required GaN structure above. The result is an improved crystal quality and lower background doping profile due to the lower lattice mismatch between GaN and AlN than between GaN and sapphire. Akasaki and Amano et al. developed this two-step growth method further, and demonstrated high quality GaN grown on sapphire in 1988 grown by MOVPE methods [29]. Nakamura improved this method, by growing a low temperature GaN buffer layer [30].

The method developed by Akasaki et al. is illustrated in Figure 2.11. It consists of an initial low temperature GaN or AlN thin film, grown at below 550°C on the

nitridated sapphire substrate to a thickness of ~ 30 nm. This is the nucleation or buffer layer, and is initially an amorphous crystal. The second stage is an anneal at a temperature of over 1000°C , which forms polycrystalline nucleation islands. This provides a high density of nucleation sites for the bulk GaN layer to be grown above at a high temperature of over 1000°C . The nucleation sites act as growth centres with the same crystal orientation as the substrate, and promote coalescence (via micro-lateral overgrowth) and the formation of epitaxially flat films that are low in defects [24, 27].

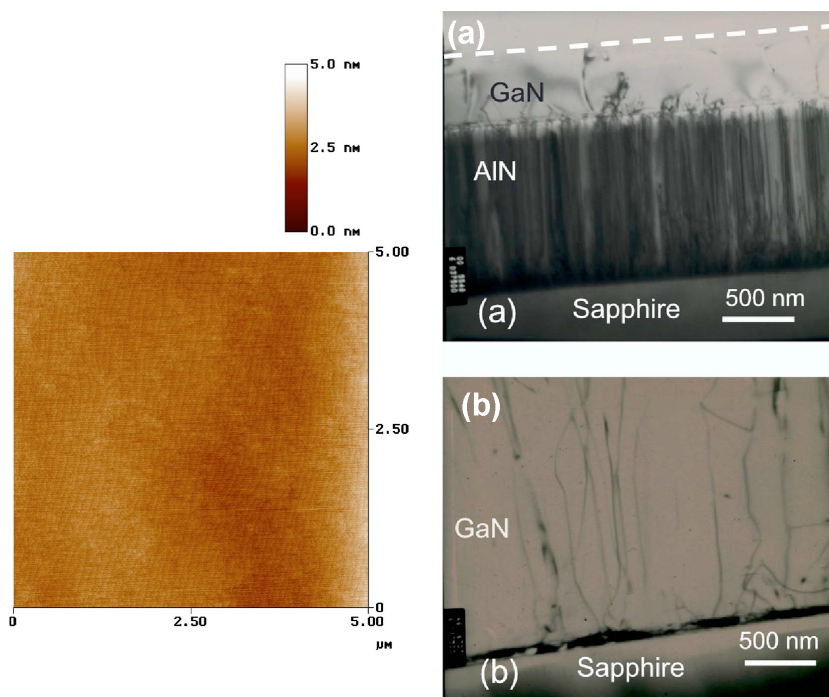


Figure 2.12: (Left) AFM image of the high temperature AlN buffer developed in Sheffield showing a very smooth surface with reduced step terminations. (Right) TEM images show the result of growing on the AlN buffer layer (a) with many fewer defects propagating to the surface than material grown with the conventional two step buffer layer method (b). Figures from [31] reprinted with permission.

A novel high temperature AlN buffer layer developed in Sheffield further improves the crystal quality and reduces cracking of epilayers during growth. An initial nucleation layer of AlN is grown at high temperature of 1150°C , resulting in an atomically flat AlN layer with very low density of threading dislocations, as illustrated in the AFM image on the left of Figure 2.12. Clear atomic steps are observed, which are quite straight and parallel, suggesting a step-flow growth mode. This means an almost two dimensional layer by layer epitaxial growth even at the early nucleation stage unlike the typical island based two step growth used conventionally. A very smooth surface results with a root mean square roughness of 0.2 nm, and very few step terminations observed in the AFM in Figure 2.12, suggesting a low concentration of dislocations. The full width at half maximum (FWHM) of the

x-ray diffraction (XRD) rocking curve from the AlN layer is measured at 59 arcsec in the (002) direction, one of the lowest values reported and suggesting a very low number of screw dislocations [31]. This is reproduced in Figure 2.13, and details of XRD are presented in section 3.3.3.

This high temperature AlN buffer provides an excellent substrate for overgrowth of the bulk GaN layer above. TEM images of GaN grown on the buffer layer are shown in Figure 2.12 (a), where a clear reduction in vertical lines (dislocations) is observed compared to the lower TEM image (b) grown on a conventional GaN nucleation layer.

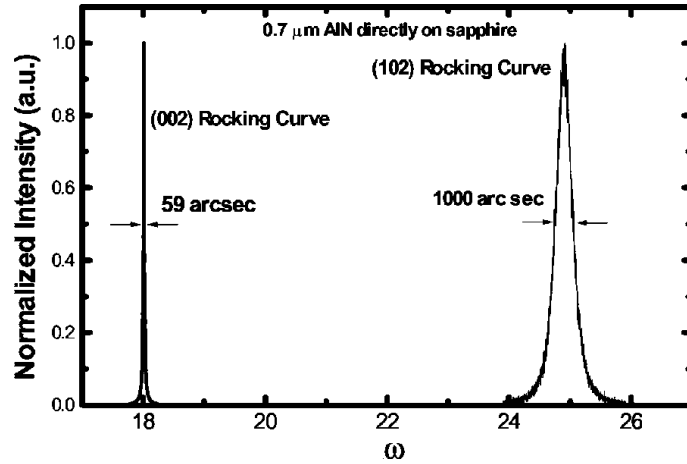


Figure 2.13: XRD rocking curves of novel AlN films showing a 59 arcsec width, the lowest reported at the time from [31] reprinted with permission.

The majority of the samples used in this work are grown by MOCVD using a Thomas Swan 3x2" shower-head reactor on c-plane sapphire substrates. For the InGaN/GaN SQW and MQW heterostructures used in this work, a thick bulk GaN layer of $\sim 1\mu\text{m}$ thickness is grown onto the novel high temperature AlN buffer layer, followed by a heterostructure composed of a series of InGaN/GaN QW layers grown at lower temperature. Typical InGaN QW thickness is between 2 and 3 nm, and typical GaN barrier layer thickness is 10 nm, which produces confinement in the InGaN QW and reduces carrier leakage. A QW sample will normally be capped by a final GaN barrier layer, however thicker GaN capping layers can be grown which can improve the sample surface.

InGaN Growth

The distribution of In, Al and Ga atoms in an unbalanced alloy is not uniform, and the inhomogeneous nature of these alloys produces important phenomena. The formation of InGaN is governed by several competing processes [7]: At temperatures above $\sim 600^\circ\text{C}$, the organometallic In source is fully decomposed, and In atoms on the

sample surface can take three paths: Either combine into a ternary alloy (InGaN, as required); migrate to a lower energy state and combine with other In atoms to form In surface droplets, or leave the growth surface entirely by a process of desorption.

The limiting factors to growing InGaN with high In content are due to temperature, growth rate and careful selection of III-V precursor ratios and carrier gas. This is especially true when growing InGaN thin films with good optical properties. During InGaN/GaN heterostructure growth, a rapid change in temperature from GaN growth at over $\sim 1000^\circ\text{C}$ to InGaN growth around $\sim 800^\circ\text{C}$ is required. Compounding this is a change in carrier gas, from hydrogen to nitrogen when growing InGaN. As a result of this, InGaN films with up to 40% In can be achieved with good optical properties, but further In incorporation is difficult to achieve with good uniformity and emission performance [7].

The lattice constants of AlN, InN and GaN are presented in Table 2.1, where clear discrepancies are observed between the three materials. When growing InGaN alloys, the lattice constant will be somewhere between the InN and GaN value, and increases with increasing indium content. This causes growth issues, especially with thin InGaN film heterostructures and nanostructures on GaN bulk layers, and an InGaN QW will generally be forced to have the same lattice constant as the underlying GaN layer, leading to strain in the well. Crystal defects also result in this change in lattice constant at InGaN/GaN material boundaries, and piezoelectric fields are generated which interfere with carriers in the structure. The main resulting issue, described as the quantum confined Stark effect, is discussed in greater detail in section 2.5.

2.3 Low Dimensional Structures

A semiconductor nanostructure is defined as a material with dimensions in the nanometre scale. In the strictest sense this is seen as structures below 100 nm in size [32], however a more broad definition is around the size of the de Broglie wavelength. The name can relate to atomic clusters, thin films, filament structures and bulk materials, and in many cases the physics associated with a nanostructure differ from the same material in a macrostructure or larger. Nanoscale materials and structures are not new, and are found in the natural world as well as materials engineering (for example, butterfly scales, and synthetic nanospheres - both producing iridescence). Characterisation of nanostructures was however a difficult task before the invention of x-ray diffraction and electron imaging techniques as features are too small to be observed with an optical microscope [32].

Development of nanostructures began with chemical synthesis to create solutions, colloids and powders of nanostructures with specific properties, and over the

past 50+ years many other methods have been developed to create features on the nanoscale. From a semiconductor point of view, advances in fabrication and processing techniques as well as growth advances in molecular beam and organometallic epitaxy led to the rise of semiconductor nanostructures such as quantum wells, dots and wires, the basis of current LEDs and other optical emitters.

Low dimensional structures such as quantum dots and quantum wells are used in emitters as a carrier confinement centre, to allow carriers to come together and recombine as photons. Initially developed in the 1970s, they are now used as a means of observing fundamental physics behind quantum mechanics, and are the basis of all commercial III-V emitters [10].

A semiconductor QW is a thin layer of low band-gap material between two layers of higher band-gap material. As illustrated in Figure 2.14, this structure produces confinement in the z direction, normally in the crystal growth direction, while allowing carrier movement in the x and y directions, perpendicular to the growth direction. When a particle is confined, the Heisenberg uncertainty principle states that movement in an axis of length Δx gives an uncertainty in momentum given by

$$p_x \approx \frac{h2\pi}{\Delta x} \quad (2.4)$$

In a semiconductor, the particle's (electron's) mass m means an energy of confinement is given by

$$E_{\text{con}} = \frac{p_x^2}{2m} \approx \frac{\hbar^2}{2m\Delta x^2} \quad (2.5)$$

and if this energy is greater than the thermal energy of the particle, kT , the above expression becomes

$$\Delta x \approx \sqrt{\frac{\hbar^2}{mkT}} \quad (2.6)$$

which, for for a typical electron mass in a semiconductor of $0.2m_0$ gives a confinement size Δx of ≈ 5 nm. Such thin regions mean quantum confinement can be difficult to achieve without advanced epitaxial semiconductor growth mechanisms. The result of equation 2.6 is equivalent to suggesting a QW width should be around the same magnitude as the electron de Broglie wavelength $\lambda_{\text{deBroglie}} = h/p_x$.

Confinement in one direction produces a quantum well, however quantum wires, with confinement in the x and y direction but movement in the z direction are also often used in semiconductors. A three dimensionally confined system, a quantum dot, is also used to explore quantum physics and for some optical devices where few discrete electron energy levels are required.

When a particle is confined, discrete energy levels are formed, shown as E_{1e} , E_{2e} , E_{1hh} and E_{1lh} in Figure 2.14. In the CB of an InGaN/GaN QW structure,

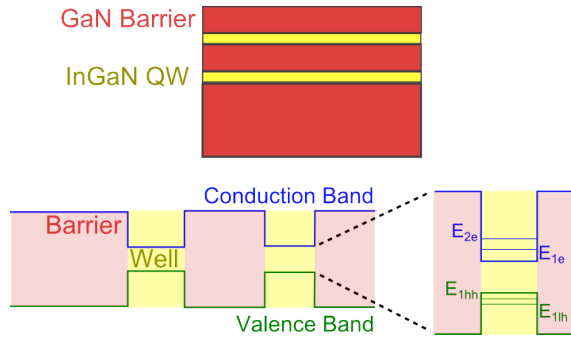


Figure 2.14: Illustration of a two quantum well (QW) heterostructure showing the material, energy bands, and electron and hole energy levels.

discrete levels of electrons are present, illustrated as E_{1e} and E_{2e} etc. in the figure. In the VB, these levels are formed by “different” carriers, and are shown as E_{1hh} and E_{1lh} in the figure. These correspond to heavy holes and light holes, and are characterised by their effective mass, which changes due to valance band splitting creating a complex overlapping band structure [7].

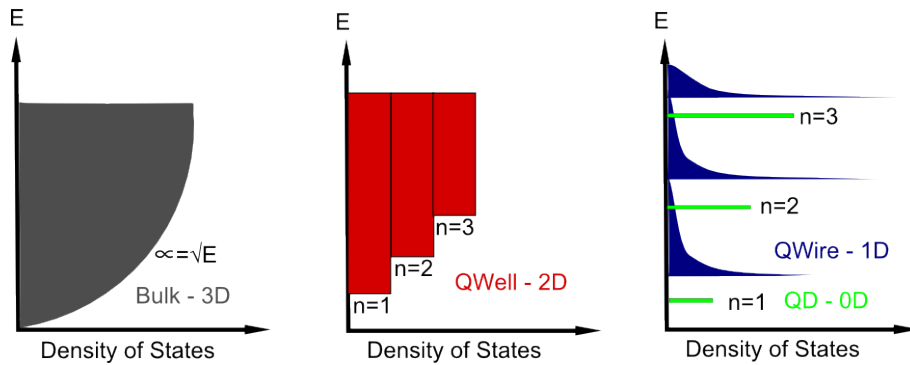


Figure 2.15: Density of states with energy for a bulk semiconductor (left), a semiconductor quantum well (centre), quantum wire (right - blue plot) and quantum dot (right - green plot).

The density of states (DOS), or distribution of energy levels within a quantum well, can be modified by changing the well’s shape, size and depth. Figure 2.15 shows the effect a QW has on the density of states compared to bulk material [16]. With a bulk material, the distribution of carriers broadens with increasing energy, allowing carriers to exist at a range of energy levels in the CB. With a QW structure, the carrier distribution is confined into specific levels or states due to the electron wave-function confinement [21].

Further confinement in two directions produces the quantum wire distribution in Figure 2.15, where a large density of states exists at specific energy levels, which then reduces dramatically due to the allowed movement in only one dimension. A quantum dot illustrated in the figure is the result of complete confinement in all directions, where only specific energy levels exist in the QD, creating a large density

of states only at these levels.

An important aspect of a quantum well structure is the increase in electron and hole wavefunction overlap. This effectively increases the photon emission probability, and therefore decreases the radiative recombination time. With a shorter lifetime to radiative recombination, carriers are more likely to emit as photons, increasing the efficiency of a structure. The nature of a quantum well, being thin enough to create carrier confinement, means these layers are often below the thickness required for dislocation formation in the crystal. This means in general that good quality crystals are grown, although issues such as strain are often compounded by the thin structures [10].

Excitons, as discussed in section 2.1.5, are a coupled pair of electron and hole, with important properties. A quantum structure acts to enhance the excitonic binding energy, by confining electrons and holes together, closer than would occur in a bulk semiconductor material. This improves the chance of electron and hole coupling together, and allows excitons to exist at higher temperatures than in a bulk system. As a result of the high exciton binding energy in GaN based emitters, most of the emission from a QW is via excitonically coupled carriers, leading to a comparatively narrow linewidth and good optical characteristics [1].

Fabricated Nanostructures

In this thesis a nanostructure will most often refer to a single or collection of columns, rods, wires and holes in the 10s to 100s of nm region. Fabricated or grown structures and arrays were recently developed as improvements in growth, nucleation and fabrication were made, and from the year 2000 onwards there has been an increase in research in this area [33]. Although initially taking the form of nanocolumns; disks, wires and other exotic shapes have now been engineered to allow various enhancements and physical phenomena to be observed. Typical uses of nanostructuring include improved crystal quality during growth [34], achieving stimulated emission for potential nanorod lasers [35, 36], changes of emission colour for potential white or colour changing LED applications [37], photonic crystals [38], and high power density LEDs [39].

Nanostructure fabrication is difficult to achieve as the nano features are below the wavelength of visible light, and therefore below the $\sim 1 \mu\text{m}$ minimum feature size attainable with conventional fabrication techniques using UV-curable polymer photo-resist masks. Sub-wavelength masking is possible using near field effects, but the most common method of masking is using electron beam lithography (EBL) [34], an adequate processing technique for research purposes, but usually too slow and costly for commercial use. Imprinting techniques can also be used, where a

pre-formed three dimensional mask is pressed into a sample to transfer the pattern [40]. Several other approaches to nanostructure masking use nano-particles as a mask: Silica nanospheres can be spun onto a sample, resolving nanostructures down to approximately 100 nm [36]. Metal films can also be used, where an anneal or the actual process of metal deposition create nanoparticles on the sample surface to be used as a mask [39, 41].

2.4 Carrier Localisation

Localisation of carriers in InGaN alloys is understood to be the reason for observations of high quantum efficiency despite a large number of threading dislocations and other defects in the crystal. Several key behaviours point to localisation as the main mechanism [42]:

- A wide FWHM observed even in single quantum well emitters - explained due to fluctuations in exciton energy as a result of localisation states.
- Variation in radiative recombination lifetime across the emission spectra and a bi-exponential time decay, suggesting multiple emission mechanisms from localised states.
- Blue shift in peak energy as a result of increasing current density - attributed to Coulomb screening of the piezoelectric field in a quantum well and band filling of localised energy states.
- The dependence of temperature on PL spectra and linewidth resulting in the characteristic “s-shift” in peak emission energy of nitrides with temperature. Caused by thermally induced de-localisation of excitons with increasing temperature.

The direct cause of this carrier localisation is generally attributed to two mechanisms. Random alloy fluctuations in the InGaN material cause a slight change in band energy on a small scale [43], and it has been suggested that holes can localise on individual In atoms [44] as well as at any potential In clusters. Slight fluctuations in the QW width also cause carriers to localise when combined with the large fields across a QW and QCSE, which results in further bending of the band-structure and hence a shift in the recombination energy at this localised level [45].

2.5 The Quantum Confined Stark Effect

2.5.1 Piezoelectric Effects

As discussed earlier in this chapter, the bond between metal and nitrogen atoms in the III-nitride Wurtzite structure is tetrahedral covalent, and is ionic in nature. The partially ionic bonding leads each individual atom of gallium or nitrogen to be charged, and any displacement of these atoms from the equilibrium position leads to a polarisation field. This is termed the piezoelectric effect, and III-nitrides are highly piezoelectric when grown in the c -direction [4].

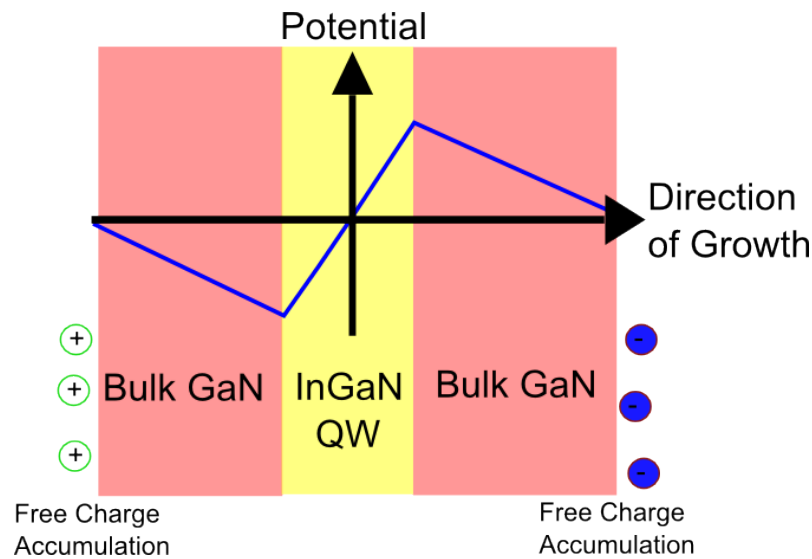


Figure 2.16: Potential profile across an InGaN QW due to piezoelectric effects showing a large electric field between the interfaces of the QW and bulk material. Charge accumulation in each bulk GaN region reduces the potential to zero some distance into the material.

Due to the inherent lattice mismatch between sapphire, GaN and InGaN in a heterostructure, strain acts on the materials, moving the atoms from equilibrium and causing piezoelectric polarisation. A GaN bulk layer will be somewhat strained due to the influence of the underlying sapphire substrates different lattice constant, however AlN buffer layers and a thick bulk layer can eliminate this strain, leaving the GaN material strain free, with equilibrium lattice constant.

Thin heterostructures such as InGaN QW layers however are sandwiched between comparably thick bulk GaN layers, and experience a large compressive strain. The InGaN QW is forced to have the same lattice constant as the underlying GaN layer, causing a strong piezoelectric field due to the atoms movement from equilibrium. The field consists of a charge at each InGaN/GaN interface, and results in a potential across the QW, with one interface positive and the other negative. The potential initially is therefore constant and positive in the underlying bulk GaN layer and

| Parameter | InN | GaN | AlN |
|-------------------------------|-------|-------|-------|
| C_{13} (GPa) | 95 | 106 | 108 |
| C_{33} (GPa) | 224 | 398 | 373 |
| e_{31} (cm^{-2}) | -0.45 | -0.37 | -0.62 |
| e_{33} (cm^{-2}) | 0.81 | 0.67 | 1.50 |

Table 2.3: Polarisation and elastic constants for III-nitride materials from [47].

constant and negative in the layer above the QW. The difference in this potential between each layer will result in free charges accumulating in the GaN bulk layers however, meaning the potential then falls away to zero outside the quantum well. This leaves a net field across the heterostructure, as illustrated by the blue line in Figure 2.16.

The magnitude of the piezoelectric polarisation due to strain in the heterostructure is given by equation 2.7, where a_s is the lattice constant under strain in the c-plane direction and a_u is the strain free lattice constant, together representing the in-plane strain [46].

$$P_{\text{pz}} = 2 \frac{a_s - a_u}{a_u} (e_{31} - e_{33} \left(\frac{C_{13}}{C_{33}} \right)) \quad (2.7)$$

The elastic constants C_{13} and C_{33} as well as piezoelectric coefficients e_{31} and e_{33} are listed in Table 2.3.

The direction of this polarisation depends on the crystal polarity, and whether the material is N- or Ga-polar. The samples used in this work are Ga-polar, resulting in a positive polarisation constant along the c-plane (0001) direction towards the sample surface.

The relationship between longitudinal field and carrier recombination in an In-GaN QW is illustrated in Figure 2.17. A clear link between carrier transition probability and piezoelectric field is observed, with the conventional polar c-plane axis (0001) having the highest piezoelectric field and corresponding lowest transition probability. This is due to the reduced carrier wave function overlap induced by the strong field across the QW. The non- and semi-polar axis observed in the figure show a reduction in piezoelectric field, corresponding to an increase in transition probability and observed as a reduction in QCSE [48]. This result shows that QCSE can potentially be managed by reducing the strain of the crystal lattice.

2.5.2 Spontaneous Polarisation

Due to the symmetry in the GaN Wurtzite crystal structure some polarisation exists even if the material is completely unstrained. This is termed spontaneous polarisation and is observed as a constant potential in the growth direction.

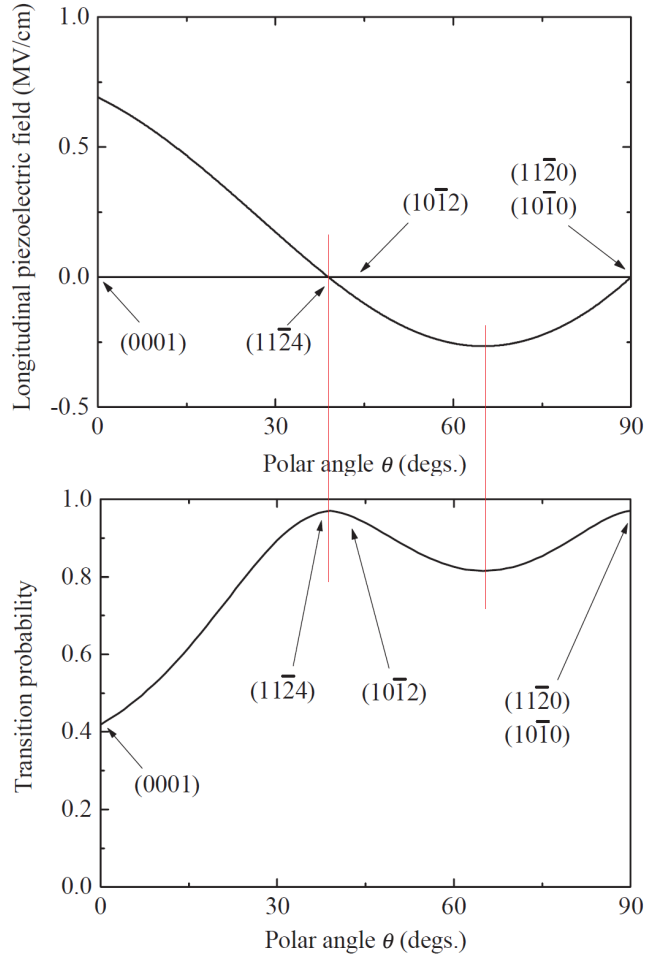


Figure 2.17: (Top) Graph of piezoelectric field against polar angle (from 0001 direction) in a strained InGaN QW. (Bottom) Transition probability vs polar angle for the same InGaN QW. A clear relationship between increased piezoelectric field and decreased transition probability is observed. Figure from [48] reprinted with permission.

In a bulk material, a surface charge will exist at the material interface, which is counteracted by free charge accumulation and results in no net charge. In a heterostructure however, the difference in spontaneous polarisation between a QW and the barrier regions will result in a field across the well.

Figure 2.18 shows the values of spontaneous polarisation constant for III-nitride materials. The change in spontaneous polarisation between InN and GaN is small, resulting in little change with InGaN alloys or GaN/InGaN heterostructures. Although a spontaneous polarisation field will be formed at the boundaries of GaN and InGaN layers, it is much smaller in magnitude than the piezoelectric polarisation resulting from a large difference in lattice constant.

The change in polarisation between AlN and GaN is large however, and results in strong spontaneous polarisation fields at the boundaries between these materials and in GaN/AlGaIn heterostructures. As the lattice constants of AlN and GaN

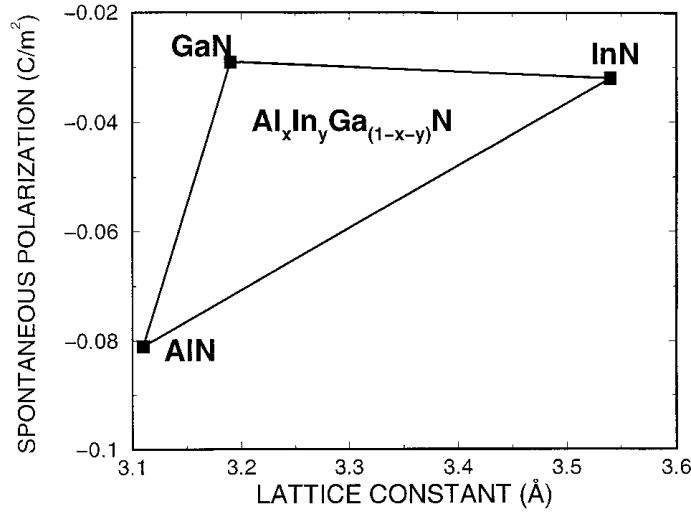


Figure 2.18: Spontaneous polarisation vs lattice constant for III-nitride materials derived by Bernardini et al. [46] reprinted with permission.

are close, piezoelectric fields are reduced, and spontaneous polarisation is likely to dominate [46].

Quantum Confined Stark Effect

The combined effect from both spontaneous and piezoelectric polarisation causes charge accumulation and carrier separation in structures, particularly at the interfaces between GaN and InGaN, and is termed the quantum confined stark effect (QCSE). The addition of both potentials creates a significant field acting on the crystal structure, although piezoelectric polarisation is usually the dominant factor, caused by strain between the GaN bulk material and thin InGaN QW structures.

The resultant built in electric field can be quantified by equation 2.8, where the subscript w represents values for the QW and subscript b values for the barrier region. P is the total polarisation on the barrier as a sum of spontaneous and piezoelectric polarisation constants, L is the layer thickness and ϵ is the permittivity (ϵ_0 is the permittivity of free space).

$$F_w = \frac{L_b(P_b - P_w)}{\epsilon_0(L_w\epsilon_b + L_b\epsilon_w)} \quad (2.8)$$

The field across the QW is quantified by equation 2.9, and can be on the order of the QW bandgap or higher [49].

$$E_w = F_w L_w \quad (2.9)$$

QCSE causes major problems with the optical and electrical performance of a device, as the field across the InGaN active region interferes with excited carriers.

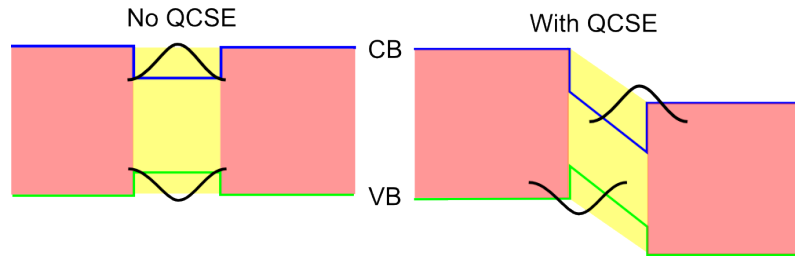


Figure 2.19: The effect of inbuilt strain in a QW, and resulting electron and hole wave functions in the CB and VB. On the left is a QW without the strain induced electric field, and on the right a QW that is deformed by this field.

The result of the inbuilt charge is illustrated in Figure 2.19, where the QW band structure is deformed by the large inbuilt electric field, causing a change in the electron and hole confinement levels and carrier wave functions. The electrons are attracted to the positively charged interface and the holes to the negatively charged, leading to a separation of carriers in the QW. The slanting of the band edges in Figure 2.19 is caused by the potential, and the CB minimum and VB maximum are separated. A red shift in peak emission wavelength, or lowering in bandgap energy, is caused by this band edge slanting.

The integral overlap between electron and hole wave functions is now effectively reduced, as carriers are separated. The optical transition oscillator strength is reduced due to this, therefore increasing the radiative lifetime of excited carriers in the system. A reduction in efficiency results, as carriers taking longer to radiatively recombine are more likely to encounter non-radiative recombination centres.

As well as a reduced bandgap energy caused by bending the band structure, and lowering the recombination efficiency by reducing the overlap between electron and hole wave functions, the exciton binding energy is also reduced slightly due to the spatial separation of carriers, resulting in fewer stable excitons at room temperature. In a bulk semiconductor, the excitons would be separated into individual electrons and holes by the a large electric field, but in a QW the carriers are confined in the z direction, and excitons still exist due to this confinement [10].

Increasing In composition in a QW increases the lattice constant of the InGaN alloy. This increases the strain and inbuilt field further. The GaN layers used in the InGaN heterostructure will force the lattice constant of the InGaN layer to a smaller value, which will increase the QCSE and further reduce the overlap of the electron and hole wavefunction. This is one of the main causes of low efficiency emission observed in nitrides and particularly in the green and above wavelength range, resulting in the green gap in LED emission [50].

2.6 Efficiency Droop

The optical emission efficiency of an InGaN/GaN based QW structure or LED device is not a constant over a large input power range. It begins low, quickly reaches a peak, and then reduces with increased carrier density. This can be observed in Figure 2.20.

The droop in efficiency at high carrier injection is currently a highly debated topic, and is likely due to several mechanisms. The three main mechanisms proposed are [51]:

- Auger recombination (exciton recombination promoting a third carrier instead of emitting a photon).
- Carrier leakage (carriers overflowing the QW active region resulting in non-radiative recombination outside the QWs).
- Defect related recombination - (carriers non-radiatively recombining via defects at high carrier density).

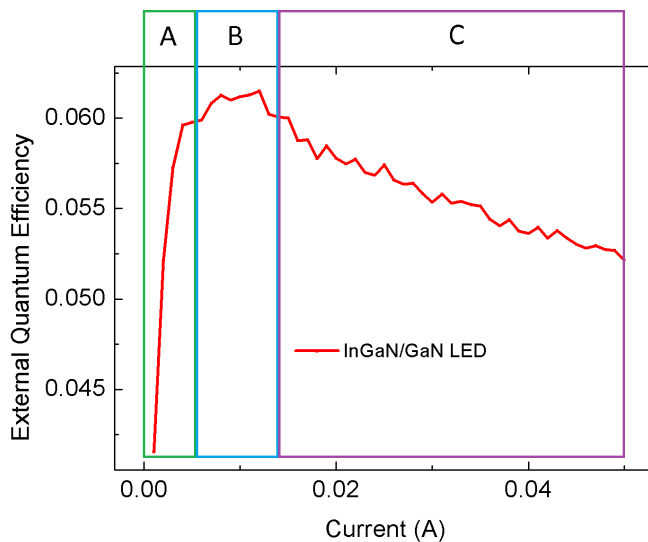


Figure 2.20: Efficiency droop of an InGaN LED structure with increasing current density, showing A, B, and C coefficient regions relating to changes in carrier loss mechanisms due to the amount of injected current.

Auger Recombination and the A,B,C Model

The change in efficiency with carrier density can be broadly described by the “A, B, C” model, shown in equation 2.10, where R is the recombination of carriers in an LED.

$$R = An + Bn^2 + Cn^3 \quad (2.10)$$

The terms A , B and C from equation 2.10 are labelled in Figure 2.20 along with the associated area of the efficiency curve of the LED.

At low carrier densities (low current in an LED), non-radiative recombination via defects will dominate via the Shockley-Read-Hall process, and results in a very low radiative efficiency as the majority of carriers recombine via defects in the semiconductor. This is termed A in equation 2.10 and takes place with individual carriers, hence the n term.

As carrier density increases to orders of magnitude above the defect level, bimolecular radiative recombination becomes the dominant factor, and the radiative efficiency begins to increase to a peak. This is the B term in equation 2.10, and consists of two carriers, an electron and hole recombining, hence the n^2 term in the equation.

At mid to high carrier density, Auger recombination, termed C in equation 2.10 becomes an issue. As an exciton recombines, there is a chance of transferring the resulting energy to a third carrier, and promoting it to a higher energy, instead of emitting a photon. This process effectively “costs” three carriers, the hole and electron forming the exciton, and the promoted third carrier, which then loses its excess energy in small phonon energy loss steps or is swept out of the device by an applied bias.

All InGaN based devices at any temperature show similar efficiency droop curves: an initial increasing efficiency up to a maximum point, followed by a decrease at large carrier density. Reducing the temperature can improve the initial low efficiency as defect recombination is reduced, but Auger based droop at high carrier density is difficult to improve upon and is a major challenge currently facing InGaN based LEDs [52].

Carrier Leakage

Importantly, Auger recombination cannot account for the complete efficiency droop curve, and several studies have shown an “A, B, C” model does not fit the droop curves obtained from InGaN based LEDs at very high injection current [51].

A second droop mechanism is carrier leakage, due to a lack of confinement in a QW or carriers overshooting the active region upon injection into the LED [54]. “Carrier leakage” encompasses several processes including a poor hole injection efficiency, ineffective electron blocking layer, poor electron capture by QWs and carrier escape from QWs.

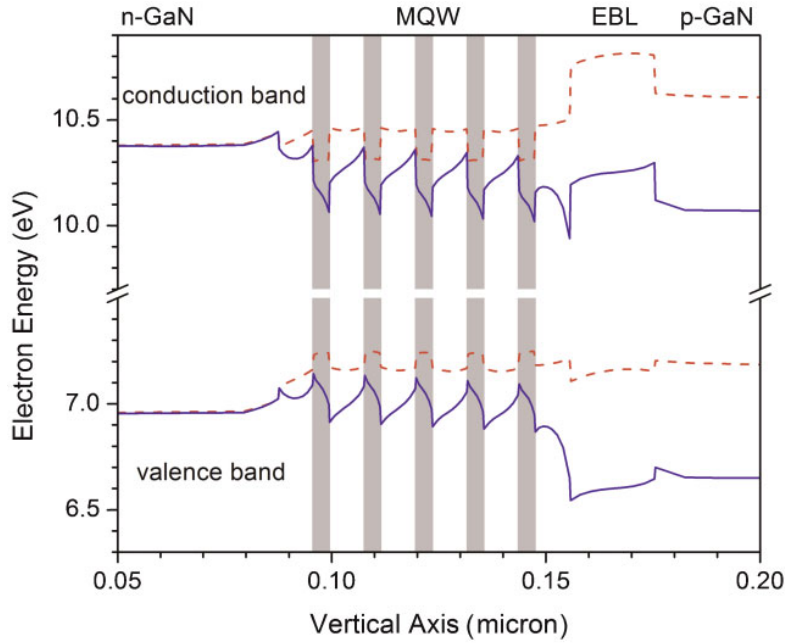


Figure 2.21: Deformed QW band structure (solid lines and grey area) as a result of the inbuilt polarisation in the QW. The dashed red line represents the same structure without a polarization effect. Reprinted with permission from [53].

An electron blocking layer of AlGaIn material is often inserted into the LED structure to create a barrier with large bandgap and thus reduce electron overflow (shown in Figure 2.21). This structure is unable to block all the injected electrons, and as injected current density increases the leakage rate is also enhanced.

Poor hole injection is a direct result of the electron blocking layer, as this region is grown prior to p-GaN growth, resulting in a barrier before the QW active region for incoming holes.

These mechanisms are enhanced further by QCSE, due to the inbuilt polarisation fields tilting the band structure of an InGaIn/GaN heterostructure. This is illustrated in Figure 2.21, where it is clear the tilted CB and VB will potentially allow injected carriers to overshoot the QW structures and leak out of the device. Charge accumulation due to the tilted bands can also cause reduced carrier capture in quantum wells, and carriers to escape confinement, especially at high current injection [55].

Defect Related Recombination

Recent work examining efficiency droop at high carrier concentration has suggested density-activated defect recombination (DADR) as a droop mechanism. This theory suggests as carrier concentration increases, the excited carriers fill defect free confined potential minima (due to fluctuations in the InGaIn QW). This forces newly injected carriers to exist at a higher energy outside the confined localisation points,

where they encounter more defects [56]. This process scales with increasing injected carrier density, as carriers continually fill confinement centres and exist at higher levels. Improved crystal quality has been shown to alleviate this issue, but droop is still apparent.

A combination of all three of the above mechanisms is the likely cause of droop, however recent work has suggested Auger recombination (and indirect Auger recombination specifically) may account for the largest percentage, suggesting an large improvement in device efficiency can be made by reducing the likelihood of Auger recombination [52].

2.7 Plasmonics

A plasmon in the scope of this work is an oscillation of electrons in a metal, or the stimulation and resulting response of an electron plasma by electromagnetic radiation. The interaction between electromagnetic waves and metals has been well studied, and can be described by Maxwell's equations even down to sub-wavelength size scales due to a high density of free carriers in metals, allowing small spacing between electron levels that are below the energy provided at room temperature. The first true description of a plasmon was described by Pines and Bohm in 1952, as a way of describing the energy losses of electrons passing through metal foils [57]. This definition of a plasmon is now regarded as a volume or bulk plasmon, and differs from surface plasmons, which were first described by Ritchie et al. in 1957 [58].

A surface plasmon is the interaction of a plasma oscillation of electrons at the surface of a metal, when the oscillation of surface charge occurs at an interface between metal with a negative permittivity and dielectric with positive permittivity [59]. A surface plasmon can exist at the interface between a metal and air, or a metal and semiconductor material (as is the main focus of the work in this thesis). Figure 2.22 further illustrates the electron oscillation between metal and dielectric material such as a semiconductor, showing the field propagating in materials with different dielectric constant.

Metals are generally reflective up to and including the visible wavelength spectrum, and therefore do not allow electromagnetic waves to pass through them. On a nanoscale at the surface of a metal however, certain energy levels can be absorbed, creating a surface plasmon (SP) or localised surface plasmon (LSP). This can be readily observed with nanoparticles of metal in solution, where the colour of the solution changes depending on nanoparticle size, due to the absorption, scattering and reflection of visible wavelength light [61]. Such a phenomenon has been used

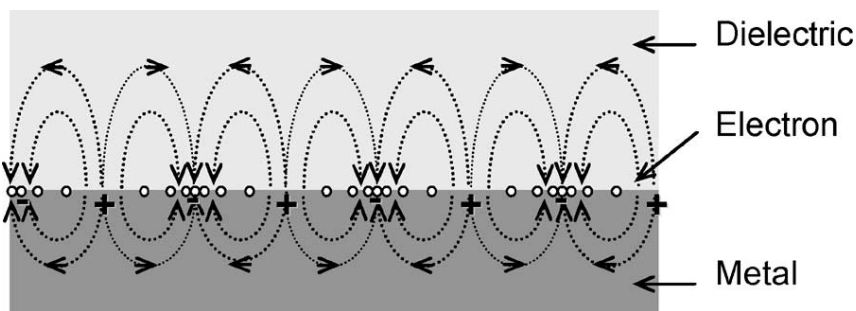


Figure 2.22: Surface plasmon oscillations generated at the interface between a metal and dielectric layer as suggested by Okamoto et al. [60]. Reprinted with permission.

for hundreds of years in stained glass, where silver and gold nanoparticles, which have LSP energies in the visible portion of the electromagnetic spectrum, are used as dopants in the glass to generate bright colours due to reflections and scattering [62].

Semiconductor - Surface Plasmon Interaction

An important phenomena developed in this thesis is the surface plasmon interaction between semiconductors and thin metal films. The SP propagation length depends on the permittivity of the metal and dielectric in its vicinity. Specific semiconductors and metals allow an increase in the SP propagation both along the length and depth of the metal film. A further important property is the interaction between an exciton (or electron hole pair coupling) and a SP. If an exciton with correct energy level exists in the vicinity of a SP, or close enough to a metal film to excite a SP, energy transfer between the two can take place. This has the potential to massively increase the efficiency of a semiconductor optical emitter, as an electron hole pair can transfer its energy to a photon via a potentially faster and more efficient emission method - a surface plasmon [63]. This is discussed in greater detail in the chapter 5, and is a method offering potentially massive increases in efficiency of an LED device or other optical emitter.

Although research into plasmonics and semiconductor material interaction is not new in other materials, promising results using GaN based emitters and Ag were only realised in 2004 [64]. Various metals were found to couple SPs to GaN, including Al, Au and Pt, [63, 65, 66] however Ag was found to be the most promising due to its plasmon energy range, which correlates well with the GaN/InGaN emission energy range [64].

In principle, a metal with a plasmon energy close to the bandgap energy of a semiconductor can create a coupling between the plasmon and excited carriers in the semiconductor. For the case of GaN based materials, especially InGaN QWs, the band-gap range of between 3.4 eV and ~ 2.25 eV corresponds to the surface plasmon

(SP) energy range of Ag, $< \sim 3.3$ eV - which reduces with shrinking Ag particle size and structure.

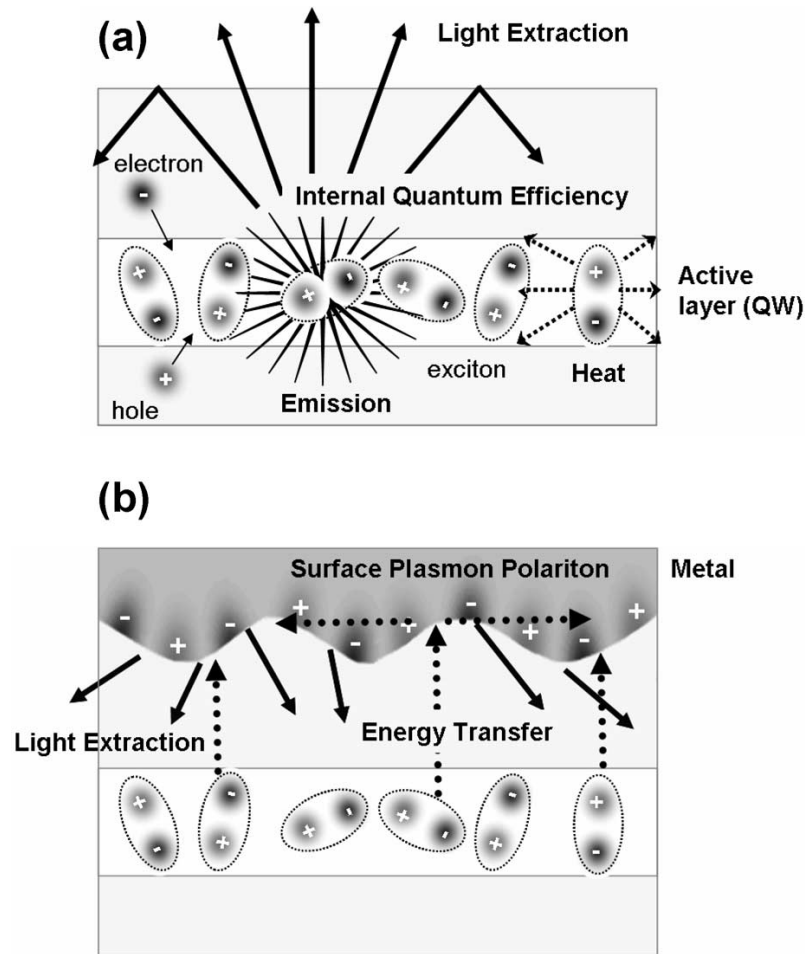


Figure 2.23: The recombination of an exciton via the normal route of electron-hole recombination (a) and by exciton-surface plasmon coupling to a metal film via an energy transfer process (b). From [60] reprinted with permission

If an Ag structure is in close proximity to an InGaN quantum well, any excitons present in the semiconductor are confined, and have a possibility of coupling their energy to a plasmon, or oscillation of electrons in the Ag. The coupling of exciton to Ag plasmon is theorised as an energy transfer process, as illustrated in Figure 2.23 and is shown to provide a faster recombination path via SP coupling than via normal radiative recombination [64]. The exciton and plasmon initially couple to form a polariton, and if the plasmon is confined as a localised SP, or meets a scattering site in the Ag, a photon is emitted at or close to the exciton energy. If there is no plasmon confinement or a scattering site is not met, as would likely be the case with coupling to a bulk plasmon in a large amount of Ag, the energy would be dissipated into the metal as a decaying bulk plasmon with ohmic losses.

Because a SP is an oscillation of electrons, the resulting evanescent wave will only

penetrate a short distance into a neighbouring dielectric. This coupling distance depends on equation 2.11, where Z is the SP-QW coupling distance and ϵ_{GaN} and ϵ_{metal} are the real dielectric constants for the semiconductor (GaN) and metal (Ag) layers respectively [63].

$$Z = \frac{\lambda}{2\pi} \left(\frac{\epsilon_{\text{GaN}} - \epsilon_{\text{metal}}}{\epsilon_{\text{metal}}} \right)^{\frac{1}{2}} \quad (2.11)$$

From this equation, it is clear that coupling strength decreases rapidly with distance. The theoretical maximum distance between SP and QW where coupling can still take place is ~ 47 nm for Ag films on GaN. An InGaN QW in a structure will have a capping layer, usually of GaN, to complete the quantum well and avoid oxidation, and this capping layer must be kept thin in order to allow SP enhancement.

References

- ¹H. Morkoç, *Nitride Semiconductors and Devices* (1999).
- ²M. Levinshtein, S. Rumyantsev, and M. Shur, *Properties of Advanced Semiconductor Materials: GaN, AlN, InN, BN, SiC, SiGe* (Wiley, 2001).
- ³M. Bass, C. DeCusatis, J. Enoch, V. Lakshminarayanan, G. Li, C. MacDonald, V. Mahajan, and E. Van Stryland, *Handbook of Optics, Third Edition Volume IV: Optical Properties of Materials, Nonlinear Optics, Quantum Optics*, Handbook of Optics (Mcgraw-hill, 2009).
- ⁴S. Nakamura and S. Chichibu, *Introduction to Nitride Semiconductor Blue Lasers and Light Emitting Diodes* (Taylor & Francis, London and New York, 2000).
- ⁵S. Nakamura, T. Mukai, and M. Senoh, “Si-Doped InGaN Films Grown on GaN Films”, *Japanese Journal of Applied Physics* **32**, 16–19 (1993).
- ⁶R. Madar, G. Jacob, J. Hallais, and R. Fruchart, “High pressure solution growth of GaN”, *Journal of Crystal Growth* **31**, 197–203 (1975).
- ⁷J. I. Pankove and T. D. Moustakas, *Gallium Nitride (GaN) I* (Academic Press, 1998), page 28.
- ⁸S. Nakamura, N. Iwasa, M. Senoh, and T. Mukai, “Hole Compensation Mechanism of P-Type GaN Films”, *Japanese Journal of Applied Physics* **31**, 1258–1266 (1992).
- ⁹H. Amano, M. Kito, K. Hiramatsu, and I. Akasaki, “P-Type Conduction in Mg-Doped GaN Treated with Low-Energy Electron Beam Irradiation (LEEBI)”, *Japanese Journal of Applied Physics* **28**, 2112–2114 (1989).
- ¹⁰M. Fox, *Optical Properties of Solids*, Oxford Master Series in Physics (Oxford University Press, 2008), page 131.
- ¹¹S. Bloom, G. Harbeke, E. Meier, and I. B. Ortenburger, “Band Structure and Reflectivity of GaN”, *Physica Status Solidi (B)* **66**, 161–168 (1974).
- ¹²M. Suzuki, T. Uenoyama, and A. Yanase, “First-principles calculations of effective-mass parameters of AlN and GaN”, *Physical Review B* **52**, 8132–8139 (1995).
- ¹³V. Davydov, A. A. Klochikhin, V. V. Emtsev, S. V. Ivanov, V. V. Vekshin, F. Bechstedt, J. Furthmüller, H. Harima, A. V. Mudryi, A. Hashimoto, A. Yamamoto, J. Aderhold, J. Graul, and E. E. Haller, “Band Gap of InN and In-Rich InGaN alloys”, *Physica Status Solidi (B)* **230**, 4–6 (2002).
- ¹⁴B. Monemar, “Fundamental energy gap of GaN from photoluminescence excitation spectra”, *Physical Review B* **10**, 676 (1974).

- ¹⁵T. Onuma, S. F. Chichibu, T. Sota, K. Asai, S. Sumiya, T. Shibata, and M. Tanaka, “Exciton spectra of an AlN epitaxial film on (0001) sapphire substrate grown by low-pressure metalorganic vapor phase epitaxy”, *Applied Physics Letters* **81**, 652 (2002).
- ¹⁶K. Takahashi, A. Yoshikawa, and A. Sandhu, *Wide Bandgap Semiconductors* (Springer Berlin / Heidelberg, 2007).
- ¹⁷M. A. Reshchikov and H. Morkoç, “Luminescence properties of defects in GaN”, *Journal of Applied Physics* **97**, 61301 (2005).
- ¹⁸J. L. Lyons, a. Janotti, and C. G. Van de Walle, “Carbon impurities and the yellow luminescence in GaN”, *Applied Physics Letters* **97**, 152108 (2010).
- ¹⁹E. F. Schubert, *Light-Emitting Diodes* (Boston Univ., 2002).
- ²⁰Q. Wang, Y. P. Gong, J. F. Zhang, J. Bai, F. Ranalli, and T. Wang, “Stimulated emission at 340 nm from AlGaIn multiple quantum well grown using high temperature AlN buffer technologies on sapphire”, *Applied Physics Letters* **95**, 161904 (2009).
- ²¹C. Klingshirn, *Semiconductor optics*, Advanced texts in physics (Springer-Verlag Berlin Heidelberg, 2007).
- ²²F. Binet, J. Y. Duboz, N. Laurent, C. Bonnat, P. Collot, F. Hanauer, O. Briot, and R. L. Aulombard, “Realization and optical characterization of etched mirror facets in GaN cavities”, *Applied Physics Letters* **72**, 960 (1998).
- ²³S. Bush, *Plessey GaN-on-silicon LED sampling*, 2013.
- ²⁴I. Akasaki, H. Amano, Y. Koide, K. Hiramatsu, and N. Sawaki, “Effects of AlN buffer layer on crystallographic structure and on electrical and optical properties of GaN and GaAlN films grown on sapphire substrate by MOVPE”, *Journal of Crystal Growth* **98**, 209–219 (1989).
- ²⁵J. I. Pankove, *Gallium-Nitride (GaN) II* (Academic Press, 1998).
- ²⁶N. K. van der Laak, R. a. Oliver, M. J. Kappers, and C. J. Humphreys, “Role of gross well-width fluctuations in bright, green-emitting single InGaIn-GaN quantum well structures”, *Applied Physics Letters* **90**, 121911 (2007).
- ²⁷K. Hiramatsu, S. Itoh, H. Amano, I. Akasaki, N. Kuwano, T. Shiraishi, and K. Oki, “Growth mechanism of GaN grown on sapphire with AlN buffer layer by MOVPE”, *Journal of Crystal Growth* **115**, 628–633 (1991).
- ²⁸S. Yoshida, “Epitaxial growth of GaN/AlN heterostructures”, *Journal of Vacuum Science & Technology B: Microelectronics and Nanometer Structures* **1**, 250 (1983).

- ²⁹H. Amano, N. Sawaki, I. Akasaki, and Y. Toyoda, “Metalorganic vapor phase epitaxial growth of a high quality GaN film using an AlN buffer layer”, *Applied Physics Letters* **48**, 353–355 (1986).
- ³⁰S. Nakamura, “GaN growth using GaN buffer layer”, *Japanese Journal of Applied Physics* (1991).
- ³¹J. Bai, T. Wang, P. Comming, P. J. Parbrook, J. P. R. David, and A. G. Cullis, “Optical properties of AlGaIn/GaN multiple quantum well structure by using a high-temperature AlN buffer on sapphire substrate”, *Journal of Applied Physics* **99**, 023513 (2006).
- ³²C. Koch and G. McGuire, *Nanostructured Materials: Processing, Properties, and Applications*, 2nd (William Andrew).
- ³³J. Li, D. Wang, and R. R. LaPierre, editors, *Advances in III-V Semiconductor Nanowires and Nanodevices* (Bentham Science Publishers, Mar. 2012).
- ³⁴S. Hersee and X. Sun, “The controlled growth of GaN nanowires”, *Nanoletters* **221** (2006).
- ³⁵R. Araki, K. Kishino, S. Ishizawa, K. Yamano, K. Nagashima, and A. Kikuchi, “Green region stimulated emission in optically pumped InGaIn/GaN MQW nanocolumn arrays of triangular lattice”, in *Semiconductor laser conference (islc), 2010 22nd ieee international*, Vol. 17, 2009 (2010), pages 23–24.
- ³⁶R. Chen, H. D. Sun, T. Wang, K. N. Hui, and H. W. Choi, “Optically pumped ultraviolet lasing from nitride nanopillars at room temperature”, *Applied Physics Letters* **96**, 241101 (2010).
- ³⁷H. Sekiguchi, K. Kishino, and A. Kikuchi, “Emission color control from blue to red with nanocolumn diameter of InGaIn/GaN nanocolumn arrays grown on same substrate”, *Applied Physics Letters* **96**, 231104 (2010).
- ³⁸T. Xu, S. Yang, S. Nair, and H. Ruda, “Confined modes in finite-size photonic crystals”, *Physical Review B* **72**, 045126 (2005).
- ³⁹Y.-J. Lee, S.-Y. Lin, C.-H. Chiu, T.-C. Lu, H.-C. Kuo, S.-C. Wang, S. Chhajed, J. K. Kim, and E. F. Schubert, “High output power density from GaN-based two-dimensional nanorod light-emitting diode arrays”, *Applied Physics Letters* **94**, 141111 (2009).
- ⁴⁰H. K. Cho, J. Jang, J.-H. Choi, J. Choi, J. Kim, J. S. Lee, B. Lee, Y. H. Choe, K.-D. Lee, S. H. Kim, K. Lee, S.-K. Kim, and Y.-H. Lee, “Light extraction enhancement from nano-imprinted photonic crystal GaN-based blue light-emitting diodes”, *Optics Express* **14**, 8654–60 (2006).

- ⁴¹B. Li, H. Zhuang, C. Xue, and S. Zhang, “Growth and characterization of pine-needle-shaped GaN nanorods by sputtering and ammoniating process”, *Superlattices and Microstructures* **43**, 262–267 (2008).
- ⁴²D. Watson-Parris, M. J. Godfrey, R. A. Oliver, P. Dawson, M. J. Galtrey, M. J. Kappers, and C. J. Humphreys, “Energy landscape and carrier wave-functions in InGaN/GaN quantum wells”, *Physica Status Solidi (C)* **7**, 2255–2258 (2010).
- ⁴³D. Watson-Parris, M. J. Godfrey, P. Dawson, R. A. Oliver, M. J. Galtrey, M. J. Kappers, and C. J. Humphreys, “Carrier localization mechanisms in InGaN/GaN quantum wells”, *Physical Review B* **83**, 115321 (2011).
- ⁴⁴L. Bellaiche, T. Mattila, L.-W. Wang, S.-H. Wei, and A. Zunger, “Resonant hole localization and anomalous optical bowing in InGaN alloys”, *Applied Physics Letters* **74**, 1842–1844 (1999).
- ⁴⁵J. Narayan, H. Wang, J. Ye, S.-J. Hon, K. Fox, J. C. Chen, H. K. Choi, and J. C. C. Fan, “Effect of thickness variation in high-efficiency InGaN/GaN light-emitting diodes”, *Applied Physics Letters* **81**, 841–843 (2002).
- ⁴⁶F. Bernardini and V. Fiorentini, “Spontaneous versus Piezoelectric Polarization in III–V Nitrides: Conceptual Aspects and Practical Consequences”, *Physica Status Solidi (B)* **216**, 391–398 (1999).
- ⁴⁷I. Vurgaftman and J. R. Meyer, “Band parameters for nitrogen-containing semiconductors”, *Journal of Applied Physics* **94**, 3675–3696 (2003).
- ⁴⁸T. Takeuchi, H. Amano, and I. Akasaki, “Theoretical study of orientation dependence of piezoelectric effects in wurtzite strained GaInN/GaN heterostructures and quantum wells”, *Japanese Journal of Applied Physics* **39**, 413–416 (2000).
- ⁴⁹F. Bernardini and V. Fiorentini, “Polarization fields in nitride nanostructures: 10 points to think about”, *Applied Surface Science* **166**, 23–29 (2000).
- ⁵⁰J. Piprek, *Semiconductor Optoelectronic Devices* (Academic Press), page 194.
- ⁵¹J. Cho, E. F. Schubert, and J. K. Kim, “Efficiency droop in light-emitting diodes: Challenges and countermeasures”, *Laser & Photonics Reviews* **7**, 408–421 (2013).
- ⁵²E. Kioupakis, P. Rinke, K. T. Delaney, and C. G. Van de Walle, “Indirect Auger recombination as a cause of efficiency droop in nitride light-emitting diodes”, *Applied Physics Letters* **98**, 161107 (2011).
- ⁵³J. Piprek, “Efficiency droop in nitride-based light-emitting diodes”, *Physica Status Solidi (A)* **207**, 2217–2225 (2010).
- ⁵⁴K. J. Vampola, M. Iza, S. Keller, S. P. DenBaars, and S. Nakamura, “Measurement of electron overflow in 450 nm InGaN light-emitting diode structures”, *Applied Physics Letters* **94**, 61116 (2009).

- ⁵⁵M. F. Schubert, J. Xu, Q. Dai, F. W. Mont, J. K. Kim, and E. F. Schubert, “On resonant optical excitation and carrier escape in GaInN/GaN quantum wells”, *Applied Physics Letters* **94**, 81114 (2009).
- ⁵⁶J. Hader, J. V. Moloney, and S. W. Koch, “Density-activated defect recombination as a possible explanation for the efficiency droop in GaN-based diodes”, *Applied Physics Letters* **96**, 221106 (2010).
- ⁵⁷D. Pines and D. Bohm, “A collective description of electron interactions: II. Collective vs individual particle aspects of the interactions”, *Physical Review* **85** (1952).
- ⁵⁸R. Ritchie, “Plasma losses by fast electrons in thin films”, *Physical Review* **106** (1957).
- ⁵⁹D. Sarid and W. Challener, *Modern Introduction to Surface Plasmons* (Cambridge University Press, 2010).
- ⁶⁰K. Okamoto and Y. Kawakami, “High-Efficiency InGaN/GaN Light Emitters Based on Nanophotonics and Plasmonics”, *IEEE Journal of Selected Topics in Quantum Electronics* **15**, 1199–1209 (2009).
- ⁶¹G. Shvets and I. Tsukerman, *Plasmonics and Plasmonic Metamaterials: Analysis and Applications* (World Scientific Pub. Co. Inc, 2011).
- ⁶²S. A. Maier, *Plasmonics: Fundamentals and Applications* (Springer Science and Business Media, LLC, 2007).
- ⁶³I. Gontijo, M. Boroditsky, E. Yablonovitch, S. Keller, U. Mishra, and S. DenBaars, “Coupling of InGaN quantum-well photoluminescence to silver surface plasmons”, *Physical Review B* **60**, 11564 (1999).
- ⁶⁴K. Okamoto, I. Niki, A. Shvartser, Y. Narukawa, T. Mukai, and A. Scherer, “Surface-plasmon-enhanced light emitters based on InGaN quantum wells”, *Nature Materials* **3**, 601–605 (2004).
- ⁶⁵T. S. Oh, H. Jeong, Y. S. Lee, J. D. Kim, T. H. Seo, H. Kim, A. H. Park, K. J. Lee, and E.-K. Suh, “Coupling of InGaN/GaN multi-quantum-wells photoluminescence to surface plasmons in platinum nanocluster”, *Applied Physics Letters* **95**, 111112 (2009).
- ⁶⁶K. Okamoto, A. Scherer, and Y. Kawakami, “Enhanced Light Emission by Exciton Surface Plasmon Coupling”, *Materials Research* **1055**, 8–12 (2008).

Experimental Techniques

3.1 Optical Characterisation

Optical characterisation is a useful tool allowing the measurement and comparison of the light emitting properties of a structure. The main technique used in this work is photoluminescence (PL), which uses a radiation source from short wavelength X-ray to infra-red to excite a sample. Carriers are generated in the material if the incident radiation has energy above the bandgap, and they may recombine and re-emit photons at material specific energies. This technique causes minimal sample damage, and can be performed without time consuming device fabrication at various steps along the development chain. It can be used to characterise a structure and provide data on performance and efficiency as well as detailed carrier dynamics.

Details of the main PL systems used in this work are presented in the following subsections:

Photoluminescence Background

Illuminating a structure using a laser or other source that has higher photon energy than the band-gap of the sample material will excite electrons from the valence band in a material (leaving behind a hole), as illustrated in Figure 3.1. These carriers will quickly relax to the band edge of the structure, losing energy by emitting phonons in small steps. At the bottom of the CB, electrons can recombine via several paths, each emitting energy by photon or phonon, as discussed in chapter 2. During the main radiative recombination path, an electron at the bottom of the CB must be able to interact with a hole in the VB, and both carriers must possess the same momentum in k-space, or have influence from a phonon to provide momentum if the band structure is indirect. Carriers generally have a short radiative lifetime, typically in the 10^{-9} s range, but this is much slower than the carrier relaxation lifetime, meaning any recombining carriers are generally at the bottom energy level

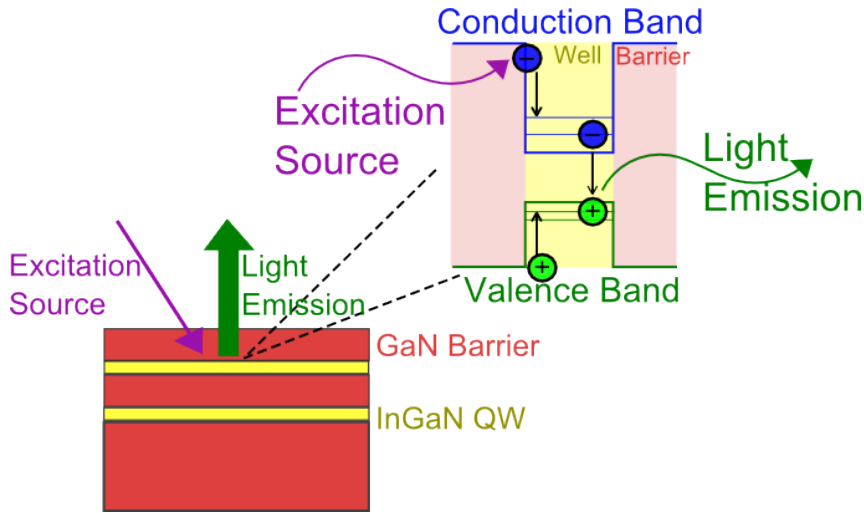


Figure 3.1: Illustration of the physics behind photoluminescence (PL). An incoming photon of energy higher than the QW band-gap generates carriers which relax to the band-gap edge, before recombining to produce a photon at the band-gap energy.

of the CB. The photons emitted have a spread of energy, resulting in a broad emission spectra, due to thermal distribution as electrons and holes gain thermal energy and reside at different states at the bottom of the conduction and valence bands, and due to the density of allowed states in a structure and localisation. [1].

In an InGaN QW structure, the initial CB to VB edge emission is a broad Gaussian spectra, normally with a line-width larger than 10 nm at room temperature. Due to problems with In incorporation during growth, a QW structure may have regions of high and low In content on a small scale. When illuminated with a laser of beam size in the μm scale, regions of both low and rich In will be illuminated, creating emission over slightly different wavelengths. This is compounded further with a MQW structure, where several QWs stacked together may have slightly different In segregation [2]. Aside from band to band emission, the recombination paths discussed in chapter 2 section 2.1.5 also cause a change in emission shape, as well as the general broadening of emission spectra found due to thermal distribution. The photon energy emitted from a QW will have a higher energy than that emitted from a bulk material, due to the quantum confinement of the well, creating specific allowable energy levels which are above the absolute band edge. This results in a change in confinement and hence emission energy of the QW structure with a change in well width. The In incorporated into the structure also changes bandgap, with increasing In content lowering the bandgap energy.

At low to moderate excitation power, the optical properties of a structure such as an InGaN/GaN QW are dominated by single electron-hole pairs as either excitons or free carriers recombining. As power density is increased and more carriers are generated in the structure, excitons begin to interact and scattering occurs, as

does the formation of bi-excitons. Further increase in power density will cause the number of electron-hole pairs to increase beyond where excitons can form, creating an electron-hole plasma [3]. The observed spectra from such a QW structure can be made up of any of these processes, depending on the measurement system used and overlap between these regimes.

3.1.1 Conventional PL Set-up

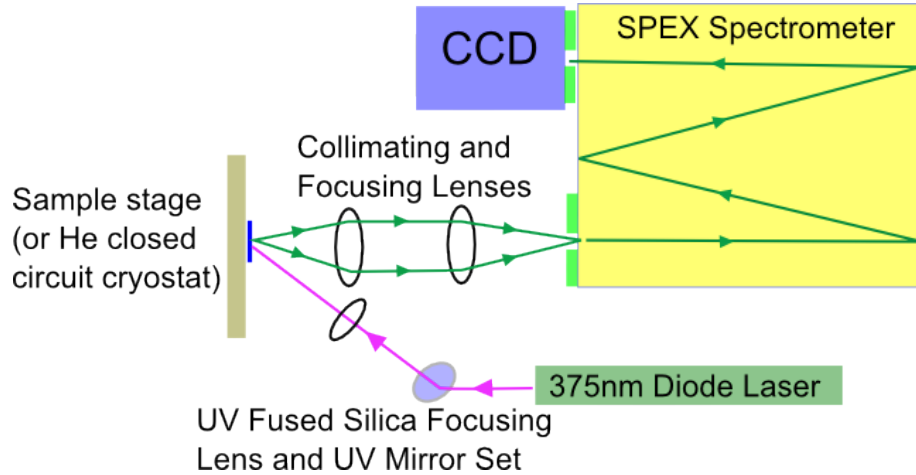


Figure 3.2: Diagram of basic photoluminescence (PL) set-up. Stage, detector and excitation source can be changed to perform various experiments.

Figure 3.2 illustrates the main PL setup used for experimentation in this report. It consists of a Jobin Yvon SPEX 0.75 m monochromator with attached charge coupled device (CCD) or photomultiplier tube (PMT) detection and a variety of laser excitation sources.

A typical sample is attached to an aluminium plate with black light absorbing backing, and placed onto a 3-axis stage with micrometer adjustment, allowing accurate sample alignment. Laser light is focused onto a sample at an incidence angle of $\sim 40^\circ$ through a series of mirrors, and sample emission is collected perpendicular to the sample, where an area from the emission cone is focused into the monochromator.

This alignment method allows the bulk of the reflected laser power to be directed off the sample and holding stage away from the monochromator entrance, allowing the CCD to have a high sensitivity to sample emission, while avoiding signal noise and damage from excitation laser radiation. The light entering the monochromator is directed to a grating, designed to split up the incoming light and disperse a wavelength range onto the CCD chip. The gratings used in this work allow a range of ~ 30 nm to be observed by the CCD - for large range scans, the grating is moved slightly, changing the dispersed wavelengths landing on the CCD. This allows a

spectra to be built from multiple scans as the control software adds the individual ranges together.

In PMT operating mode, a thin slit is placed before the PMT allowing a small range of the spectrum to enter the device. When photons are absorbed a current is produced by the PMT, which is translated to a signal by the control software. The width of the slit changes the measurement range and resolution - which can be as small as in the angstrom range. The grating in the monochromator is again scanned, as with a CCD, however only a very small range of spectrum is detected by the PMT, meaning the grating must make many small movements in an experiment to create a full spectrum.

A sample can be illuminated with several lasers (with energy above and below the GaN bandgap energy) that can be switched into the PL system with minimal re-alignment of mirrors and lenses.

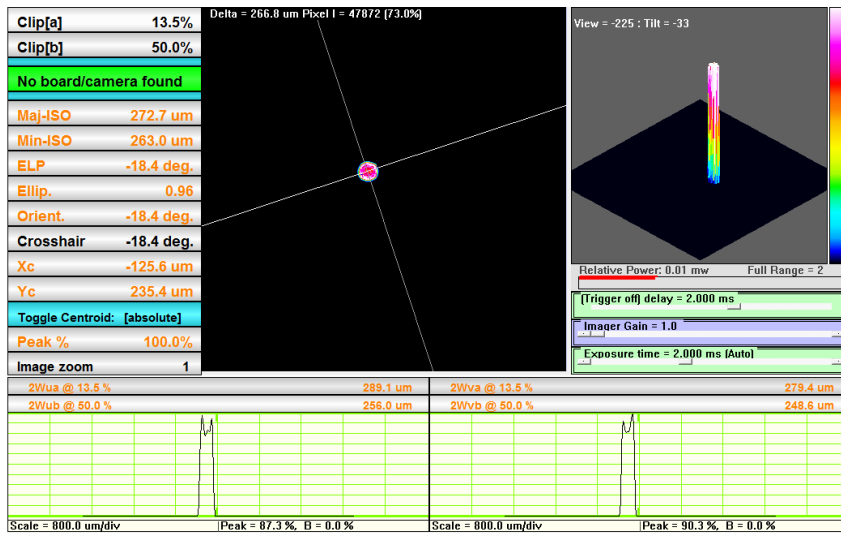


Figure 3.3: Laser beam profiles obtained with Beamage CCD beam profiling system of a 325 nm He-Cd laser.

Diode lasers of wavelength 375 nm and 405 nm with power 60 mW and 80 mW respectively are the main illumination sources, and are programmable to operate in pulsed or continuous wave (CW) mode. These diode lasers excite only the InGaN active region, and a He-Cd 325 nm laser is also used to probe the GaN bandgap. The mirrors used in the system are optimised to have very high reflectivity of $>99\%$ at wavelengths between 300 nm and 550 nm. A pulsed diode-pumped solid-state (DPSS) 266 nm high power laser is also used to inject a large number of carriers into a sample, used to measure efficiency droop, and obtain stimulated emission properties from a structure.

The power of the excitation laser can be adjusted to a wide range of values using a computer controlled interface and UV enhanced rotating graded attenuator. This

allows the study of input radiation power dependence of a sample, and allows for safe laser alignment using a low power before measurement at high power.

Lasers, particularly the laser spot size, shape and profile, are characterised by various methods: A CCD laser beam characterisation system is initially used to evaluate the laser beam as it propagates through the system. Diode lasers generally show a Gaussian-like profile and are often slightly elliptical, whereas gas lasers such as the He-Cd 325 nm laser generally have a flat top profile, as can be seen in Figure 3.3.

Knowledge of the accurate beam size and shape of the illuminating light is very important for calculating power density when performing PL. A method developed to find beam size and shape without inserting a camera into the system is by using a sample or glass slide coated in a UV photo-resist polymer. Because the lasers used are UV or near UV, they can very quickly cure photo-resist and, after illuminating and developing a resist coated sample, a microscope or SEM can be used to accurately measure the beam size and shape, as illustrated in Figure 3.4.

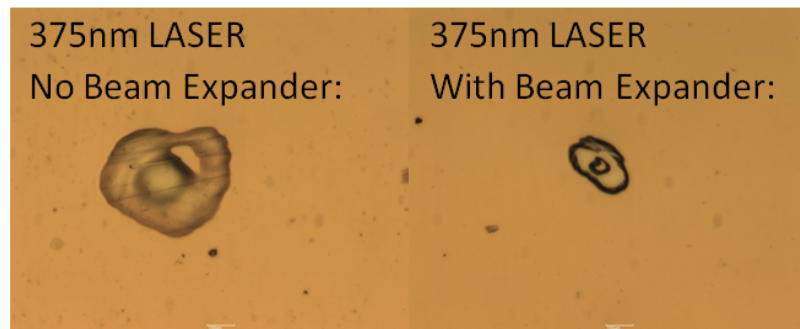


Figure 3.4: Laser beam profiles obtained by curing a photo-resist polymer coated onto a glass slide with a laser. On the left is the profile obtained without a beam expander, and on the right the profile after beam expansion and therefore improved focus.

A small uniform laser spot is vital for accurate PL measurement. Ideally a round “top-hat” or flat top beam profile is required, with a uniform energy distribution. This allows unvarying excitation of a sample under the complete laser spot. In reality, lasers are often Gaussian in profile, which can cause uniformity problems due to a high excitation power at the centre and lower edge excitation.

To combat the Gaussian shape, beam homogenisation can be accomplished using a flat top generator. This system of lenses is designed for a specific laser and can convert a Gaussian profile to flat top. These systems are expensive and difficult to align, and will reduce the transmitted laser power; a compromise therefore is a small beam size. Due to lens and laser aberrations, a small spot is difficult to produce, and improvements can be achieved using various optics. The main tool for

reducing spot size is a beam expander; a larger beam size passing into a focusing lens will utilise more of the lens surface and allow for a smaller spot size at the focal point. Adjustable beam expanders for various laser wavelengths are a cost effective way of greatly improving a PL system, by expanding a beam, and providing better coherence.

The typical beam diameter of a 375 nm diode laser is 1 mm before focusing. After propagating to the sample via mirrors and focusing lenses, the size is found to be $\sim 250 \mu\text{m} \times \sim 200 \mu\text{m}$ in diameter and elliptical in shape in the set-up used here. If a beam expander is used, it must be inserted parallel to the beam between mirrors while the laser beam is still in line with the originating diode to avoid losses and aid in sample focussing. Using a five-times beam expander, the laser spot becomes ~ 5 mm in diameter before the focussing lens, and has improved coherence. This leads to a spot size of $\sim 50 \mu\text{m}$ in diameter at the stage after focusing, approximately 5 times smaller than without an expander. This is demonstrated in Figure 3.4 using the photo-resist method of evaluating spot size discussed earlier in this section, where it is clear that a beam expander results in a smaller and cleaner laser spot. Typically, power density without a beam expander is 50 W/cm^2 for a laser power of 10 mW. Using a 5x beam expander, a density closer to 1000 W/cm^2 can be achieved at the same 10 mW excitation power.

Low Temperature PL

A vacuum stage with attached cryostat and heater can be incorporated into the PL set-up in Figure 3.2 in place of the normal three-axis sample stage. The cryostat, a CTI model modified by Janis to incorporate a vacuum stage with optical access allows PL measurements to be taken in a vacuum and at a range of temperatures. A minimum temperature of below 10 kelvin (K) can be reached with the CTI Cryogenics cryostat, and an accurate temperature monitor and heater controller by Lakeshore allows PL at a wide range of temperatures up to 350K. Low temperature PL allows various optical properties to be observed and is an important measurement tool for understanding the properties of a structure. As thermal energy is reduced with lowered temperature, the line-width of the spectra will narrow as carriers lose thermal energy. As temperature is reduced further, carriers begin to confine at potential minima in the band structure as they have very little thermal energy to move around, allowing observation and comparison of band structure and band filling effects between samples.

Angular Resolved PL

Measurement of emission angle can be performed using an angular resolved PL system, consisting of a moveable excitation source and light collection source mounted on a goniometer, with the device under test at the centre. Individual spectra are taken at increasing angle in relation to the device, and a spectra matrix is built of emission intensity against angle. The system consists of a 375nm diode laser used for excitation, usually held at a constant position. A fibre optic cable mounted on a bar and piezoelectric computer controlled rotation stage is used to collect light. The sample is mounted directly above the rotational stage centre, and the fibre can move around it collecting emission at angles between 0° and 180° . The fibre is coupled to a Horiba spectrometer with either a CCD or PMT used for detection of the emission spectra.

3.1.2 High Power PL

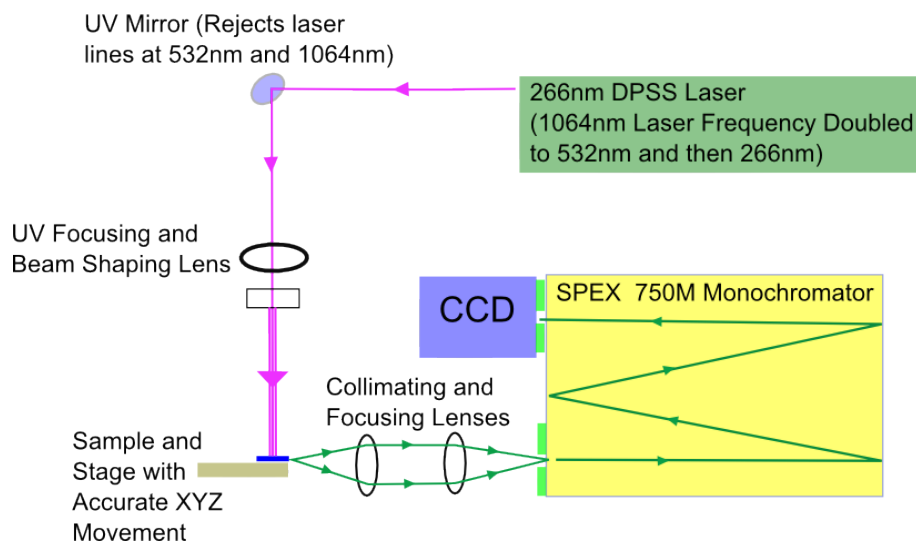


Figure 3.5: Schematic of the edge emission high power PL set-up used in this work. A high power laser is directed perpendicular to a sample, and emission is collected from the edge of the wafer.

Very high excitation power PL using a similar detection set-up to conventional PL measurements can be performed with a variety of lasers. Typically the lasers will operate in pulsed mode, with a very short pulse width and low repetition rate. This allows a high excitation energy to fall on the sample, generating a large number of carriers, but reduces the heating effect associated with a CW laser as the sample is allowed to cool (and carriers allowed to relax) between pulses.

In this work, the main high power laser used is an Nd:YAG DPSS 266 nm laser, consisting of an array of infra-red lasers emitting at 1064 nm, which are frequency

doubled twice to produce a final deep UV emission at 266 nm. This laser has a minimum pulse width of 9 ns and adjustable frequency which is set to 850 Hz in normal operation. An average maximum power of 2 mW produces a peak pulse power density of over 2 MW/cm² when correctly focused to a spot size of diameter 200 μ m. Such a high excitation power creates a large number of carriers, and allows efficiency droop to be observed for InGaN QW structures.

This system can also be used to generate stimulated emission from a sample in edge-emission alignment. A diagram of this system is illustrated in Figure 3.5.

The excitation laser (a 266 nm DPSS laser used here) is incident perpendicular to the sample, and focussed into a rectangle \sim 5 mm long x \sim 0.5 mm wide. The active region of the sample excited by this elongated laser spot acts as a gain region.

The resulting PL emission is collected from the edge of the sample, and directed into a highly accurate 0.75 m long monochromator by focussing lenses, before entering into a TEC cooled CCD. This results in very accurate spectral resolution well below 1 nm.

If a suitable sample is cleaved well, the edges of the sample can act as facets, providing a highly reflective surface which allows the emission to reflect inside the sample. This confinement of the light emission in a cavity combined with population inversion due to the high laser excitation power can generate stimulated emission.

3.1.3 Time Resolved PL

Time resolved photoluminescence (TRPL) is a method of exploring the decay rate of photon generated carriers in a structure. Knowledge of the lifetime of radiative and non-radiative carriers allows the carrier dynamics in a system to be understood.

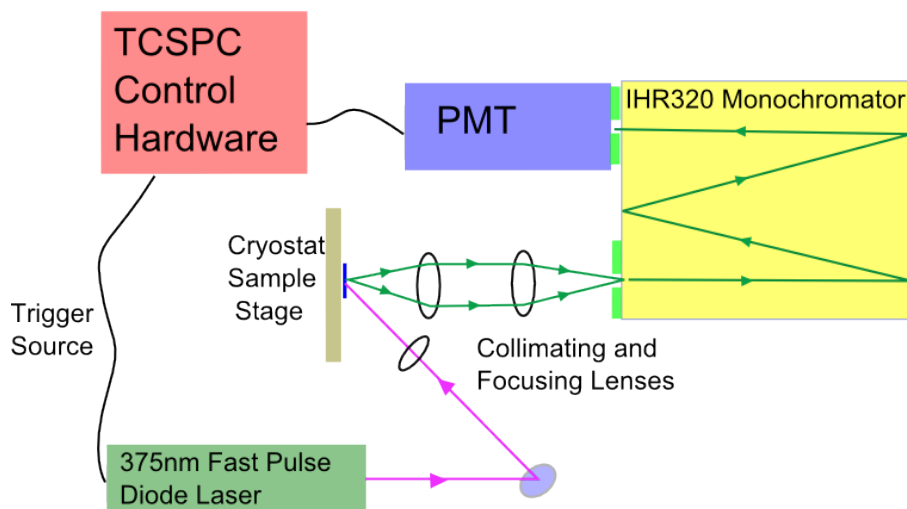


Figure 3.6: Diagram of time resolved photoluminescence (PL) set-up used in this work. A very fast pulsed laser excites a sample, and a highly sensitive detector measures the decay rate of the resultant excited carriers.

The system used for measuring carrier decay times used in this thesis is described in Figure 3.6. It utilises a laser with very short pulse width, on the order of 80 ps, and a highly sensitive time correlated single photon counting (TCSPC) system as a detector able to collect the sample emission through a Horiba iHR320 monochromator.

The laser excites carriers in the structure under test for a very short period of time, with a comparably long off time. Operating at a wavelength of 375 nm, this allows the laser to pass through the GaN layers and only excite the InGaN active region. The density of the generated carriers in the sample can be estimated based on the structure, as well as laser power and pulse conditions.

From the initial rise of the laser pulse, a single photon counting detector begins timing and detecting emission from the structure. With a laser pulse width of 80 ps, which is faster than the lifetime of carriers in an InGaN/GaN QW sample, carriers can be quickly excited in the QW and then allowed to relax and recombine without further carrier generation. As the detector collects the emission, time decay information is gathered that can be fit with exponential functions to model the carrier relaxation and recombination mechanisms of a sample [1].

3.2 Sample Fabrication

Samples used in this work consist both of InGaN/GaN based heterostructures, grown specifically to investigate the physical properties of a material and investigate potential improvements, and full device wafers consisting of InGaN/GaN quantum structures plus p- and n- doped regions.

Structures such as InGaN/GaN quantum wells grown on a layer of bulk GaN with no intentional doping cannot be used for LED devices or electroluminescent measurements. They can however allow the investigation of physical properties of a QW to be used in an LED, and allow experiments to be performed using other analytical techniques such as photoluminescence. Crucially, these structures are much easier to grow and process than a complete LED structure, as optimisation of doping is not required, and time consuming device fabrication and contact formation can be omitted.

3.2.1 Preparation of Samples

The majority of samples used in this work were grown on 2 inch sapphire wafers, and are cleaved into smaller pieces to reduce wastage and improve the uniformity between samples. Cleaving of sapphire with a GaN epilayer grown on the surface is a difficult process, and is usually accomplished manually instead of using a conventional scribe and break machine. A diamond tipped pen is used to scribe the back of a wafer

| Evaporation Method | Rate Monitor | Deposition Rate (nm/minute) @ Current | Vacuum Level (mTorr) | Dielectric Material |
|--------------------|-------------------------|---------------------------------------|----------------------|-------------------------|
| Thermal | QCM/Weight of material. | 0.1-4 @ 10-20 A (tungsten coil) | $\leq 1e-5$ | No |
| e-beam | QCM | 0.01-1 @ 12-30 mA (e-beam source) | $\leq 1e-6$ | Yes (SiO ₂) |

Table 3.1: Comparison between e-beam and thermal evaporation, showing important parameters of each method.

along the axes parallel and perpendicular to the wafer flat - corresponding to crystal orientations. After creating a scribe mark, raising the wafer on a glass slide and aligning the scribe and slide edge allows a cleave with enough pressure applied. Typical sample sizes used are approximately 5 mm x 5 mm square and taken from near the centre of the wafer to avoid poor uniformity of the structure often found at the wafer edge. Typical sapphire substrates are 300 $\mu\text{m}+$ in thickness, with several μm of GaN material above this creating the device structure.

3.2.2 Metal Deposition

Metal deposition is performed in a vacuum via e-beam or thermal evaporation, allowing a large range of metals to be deposited as well as some dielectrics. Table 3.1 compares both methods and details some specific parameters of each method.

Deposition is monitored with a quartz crystal monitor (QCM), to an accuracy of at least 0.1 nm/s in both e-beam and thermal evaporators. Thermal deposition thickness can also be calculated using the weight of the metal used in the deposition.

In the Edwards E306 thermal evaporator used in this work, metals are placed into a tungsten coil carrier, and samples are affixed next to a QCM 12 cm away (giving an even coat and reducing sample heating). The system is pumped down to a vacuum level of $\sim 10^{-6}$ mTorr. A large current is passed through the tungsten coil (typically 10s of Amps) and as this heats and melts the metal, it evaporates due to the low pressure environment, coating the entire chamber including the sample and QCM.

For e-beam systems a vacuum chamber is also utilised, however the coating metal is placed in a crucible at the bottom of the chamber with the sample and QCM located above it. An electron beam is generated and focused into the crucible, which heats and evaporates the source metal. E-beam evaporation systems can also be employed to deposit layers of SiN or SiO₂ insulating materials, and transparent conducting materials such as indium tin oxide (ITO).

| Material | Process and Gas | Deposition RF Power | Deposition Rate (nm/minute) | Temperature (°C) |
|------------------|---|---------------------|-----------------------------|------------------|
| SiN | PECVD - SiH ₄ and O ₂ | 50 W | 10 | 300 |
| SiO ₂ | SiH ₄ and NH ₃ | 20 W | 100 | 20, 200 or 300 |

Table 3.2: Deposition parameters for SiN and SiO₂.

3.2.3 Dielectric Material Deposition by Chemical Vapour Methods

Plasma enhanced chemical vapour deposition (PECVD) is used to deposit layers of insulating material such as SiO₂ and SiN to a high accuracy with good uniformity. Insulating layers are useful in device fabrication to separate areas and contacts in a structure, avoiding short circuits, or to passivate or cover areas of a sample which may be susceptible to damage or oxidation.

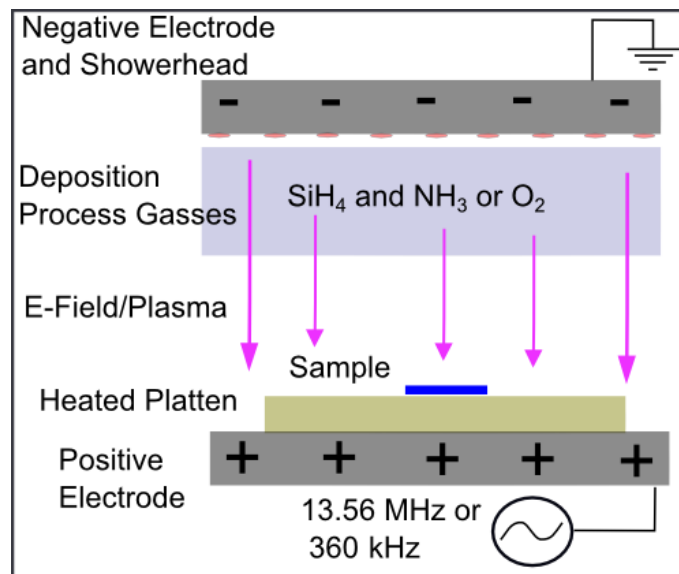


Figure 3.7: Diagram of a plasma enhanced chemical vapour deposition system.

The tool used in this work is a Plasma-Therm 790 series PECVD, and the basic process of chemical vapour deposition is illustrated in Figure 3.7. Carrier gasses flow through a showerhead into a vacuum chamber which contains the samples to be coated on a heated platen, typically at 300°C. A plasma generated by a RF electromagnetic field operating at 13.56 MHz causes the gasses to ionise and be accelerated towards the sample, where they react on the surface. The material grown can often cause stresses on the underlying wafer, and therefore a low stress deposition can be accomplished by oscillating between a high (13.56 MHz) and low (360 kHz) RF frequency, creating two layers of opposing stress to provide an overall neutral effect. The layers grown are epitaxially flat, and good insulators, which also

work well as a robust hard masking material.

The deposition rate and thickness of a layer can be accurately monitored using ellipsometry, either in the process chamber or after processing in a dedicated ellipsometry system. If a coherent beam of light is reflected off the surface of a film at different angles, the change in polarisation of the beam can be used to determine material refractive index and thickness. Broad spectrum light sources or individual wavelength lasers can be used, depending on the transparency of the material under test. An interference technique can also be used, where the incidence and reflected light interfere creating maxima and minima at a detector that change depending on film thickness. Measurement of the interference pattern produced from a film allows accurate thickness to be deduced [4].

3.2.4 Rapid Thermal Processing

Low temperature processing is a desirable technique for semiconductor fabrication, as it reduces the distribution of impurities and diffusion, which is potentially damaging to the material. Some high temperature processing is unavoidable however, and a compromise is to reduce the time spent at this high temperature, and improve uniformity of the temperature gradient to reduce wafer bowing. Rapid thermal processing is used to accomplish this, and provides a way of quickly heating and cooling a wafer in a thermally isolated system with very good repeatability.

The system used in this work is a Mattson rapid thermal processing system consisting of a sealed chamber with quartz sample loading tray. A Si carrier wafer rests on small quartz pins on the loading tray, which are chemically stable and have low thermal conductivity, so as not to draw heat away from the wafer. A sample is placed onto this carrier, and a second Si wafer is placed above, suspended by the quartz pins so as not to touch the sample surface. After loading, the process chamber is purged with nitrogen before introduction of the gas to be used in the annealing procedure, either nitrogen or dry air (nitrogen:oxygen 80:20). The heating action is performed by an array of tungsten-halogen lamps with a broad beam to quickly and uniformly heat the wafer to temperatures of up to 1200°C. After annealing, the chamber is cooled quickly at a controlled rate using a nitrogen gas purge.

A typical process is:

- An initial nitrogen purge of the chamber is performed to remove oxygen and other impurities from the process chamber.
- The temperature is ramped to 300°C and held during initialisation of the feedback systems.

- The temperature is ramped very quickly to the selected value, controlled accurately by continual pyrometer and thermocouple feedback.
- The temperature is held for the process time (typically several minutes).
- A rapid cool of the chamber is performed along with a nitrogen purge.

Process times are on the order of a few minutes, instead of tens of minutes used in a typical furnace. Ramping and cooling times are performed quickly and repeatedly, controlled using thermocouples and pyrometers to provide fast feedback and allow accurate temperature control [4].

3.2.5 Dry Etching of Semiconductor and Dielectric Materials

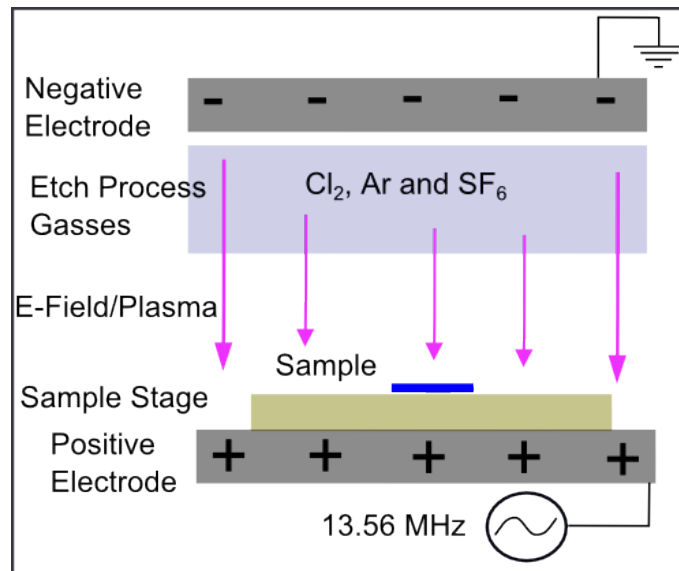


Figure 3.8: Diagram of a reactive ion etching system.

Reactive ion etching (RIE) is a technique developed to provide a highly anisotropic etch with high selectivity, and can be used to etch various materials using a range of gasses. For tougher materials such as GaN, an inductively coupled plasma (ICP) RIE can be used to allow fast and highly selective etching with a more powerful and highly directional plasma generated by an oscillating strong magnetic field, as illustrated in Figure 3.8.

The process uses an electromagnetic field varying at high frequency, typically 13.56 MHz, which allows the formation and accurate control of a plasma. Process gasses are introduced to the chamber, and the selected gas ions formed in the plasma react with the sample surface to remove material. Processing is performed under specific pressure and temperature to effectively create and maintain the plasma and

| Material | Process and Gas | Etch Rate (nm/minute) @ RF Etch Power | Mask Mate- rial | Endpoint |
|------------------|--|--|-------------------------------------|-----------------|
| GaN | RIE-ICP - Cl ₂ , Ar, SF ₆ | 100 @ 50 W (+450 W ICP) | SiO ₂ , Pho- toresist | 532 nm Laser |
| SiO ₂ | RIE - CHF ₃ , SF ₆ | 20 @ 80 W | Ni, Photore- sist | 633 nm Laser |

Table 3.3: Etching parameters for GaN and SiO₂.

control etch conditions, and the sample is often cooled to avoid excess damage due to localised heating.

The main details and etch parameters for GaN based materials and SiO₂ dielectric material is illustrated in table 3.3.

For III-nitride based materials, chlorine based gasses are used during etch processes to effectively react with GaN. Chlorine etches allow good selectivity of the etch using hard masks such as SiO₂, and the waste product is easier to process than bromide or iodide based etches. Argon gas is also often included in an etch recipe to bombard the crystal structure and further improve etching rate via sputtering. The Ar gas also helps with anisotropic etching, as it directionally bombards the surface of the sample, but not the sidewalls of the structure.

The ICP-RIE tool used in this work is an Oxford PlasmaPro system. A typical process recipe used in the fabrication of structures in this work contains both Cl₂ and Ar, as well as SF₆ to improve etch rate if required. The gas ratio is of the order 45:12 Cl₂:Ar and a relatively low etch power is normally used to avoid damaging active regions in the sample, such as QWs. A low etch power also allows the etch mask to withstand etching for longer, and reduces damage and material sputtering to the sidewalls of the structure. This damage reduction is especially important for LED structures containing QWs, where surface states caused by sidewall damage can drastically reduce the efficiency of a device by allowing carrier recombination non-radiatively at the etched surface [5].

The etching rate and depth can be monitored using an endpoint system, as illustrated in Figure 3.9, which works in a similar way to ellipsometry however is incident perpendicular to the sample (reflectometry). A laser is focused onto the sample to be etched, and the reflection detected. From known parameters of laser wavelength, refractive index and reflectivity of the materials, as well as an estimate at the sample structure, a model of the etch conditions is produced, shown in the upper trace in Figure 3.9. As the sample is etched, the interference caused by the laser reflecting between different epitaxial layers, in this case the changes in refractive index between sapphire substrate and GaN, and GaN surface and air,

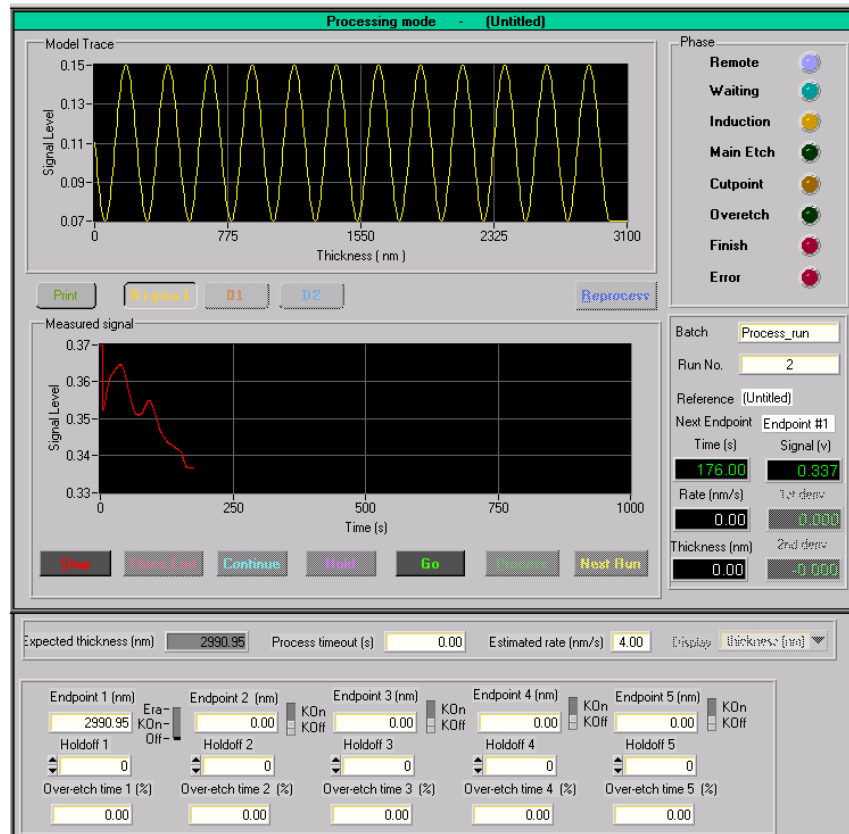


Figure 3.9: Endpoint etch monitoring system, showing the model of the material and etch conditions above (yellow trace) and actual in etch monitoring below (red trace).

allow thickness to be calculated by comparing the real laser response and modelled response in the lower trace of Figure 3.9.

As etching is performed and the GaN layer is thinned, the laser interference pattern changes, which allows an estimation of the current etch rate and depth [4]. As is observed in the Figure, the real laser response (red trace) doesn't follow the model exactly, especially when etching small structures such as nano-features, where some areas under the laser stay at the original height, and some areas are etched. The trace clearly shows oscillations however, and matching the peaks and troughs to the model allows accurate depth gauging while performing the etch.

3.2.6 LED Fabrication

The structure illustrated in Figure 3.10 is of a typical InGaN/GaN MQW LED grown on sapphire. The p-GaN and n-GaN regions are illustrated, separated by a thin InGaN/GaN MQW heterostructure region. The MQWs are inside the depletion region of the LED, which is formed between the p- and n-GaN layers and extends into them for some distance, on the order of 10s to 100s of nm, depending on dopant concentrations. Typical commercial LEDs will vary from low power indicator type

emitters using this structure, up to high power LEDs used for illumination purposes that have more complex structure, often involving flip chip or vertical LED geometry to aid in heat extraction [6].

Due to the insulating nature of the sapphire substrate used, a top down approach to LED fabrication is required, as oppose to a vertical LED structure. During fabrication, the wafer is etched with a mask such as the one illustrated in Figure 3.10 inset to expose the n-GaN region, allowing a thick low resistivity contact to be deposited. A thin semi-transparent p-GaN contact is then deposited, which is used for light extraction on basic LED structures, but can have poor ohmic properties. A thicker metal bond pad contact is often deposited in the corner of the p-region, to create a good ohmic contact during wafer bonding yet still allow light to emit through the majority of the contact [7].

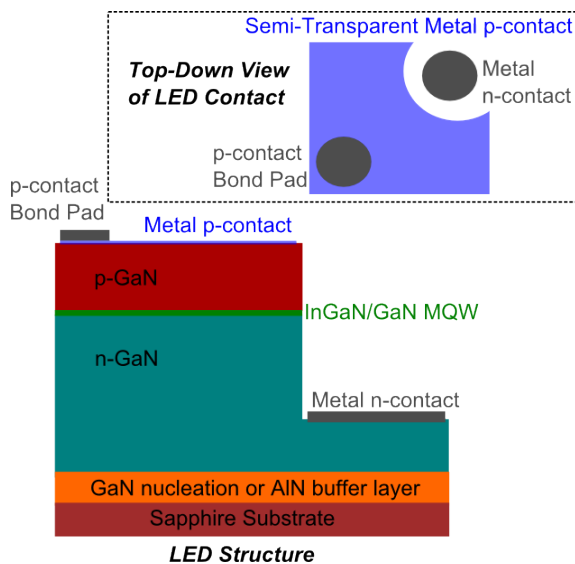


Figure 3.10: Typical GaN based LED structure and top-down view of an LED contact (inset).

Several improvements to the basic LED structure have been developed, however most are complex procedures which drive up the overall cost of the emitter. From a growth perspective, various buffer layers and patterned sapphire substrates allow improved light extraction and crystal quality, which improves device efficiency by reducing defects [8]. Mask structures and contacts have been developed incorporating current spreading layers which reduces localised current “hot spots” which lower overall efficiency due to current crowding and heating [9]. Transparent conductors such as indium tin oxide (ITO) and thin metal alloys have also allowed improvements to light extraction and conductivity. A further method of improving light extraction and heat dissipation is the use of “flip chip” or lift off devices [10]. With this method, the device is flipped, allowing light extraction from the back side sapphire of the device or the substrate to be removed entirely. In this system, the

p-contact can be thicker and have improved ohmic properties as it does not transmit light. Often this contact can act as a mirror to effectively improve light extraction by reflecting light back towards the sapphire emission surface.

3.3 Structure Characterisation

3.3.1 Atomic Force Microscopy

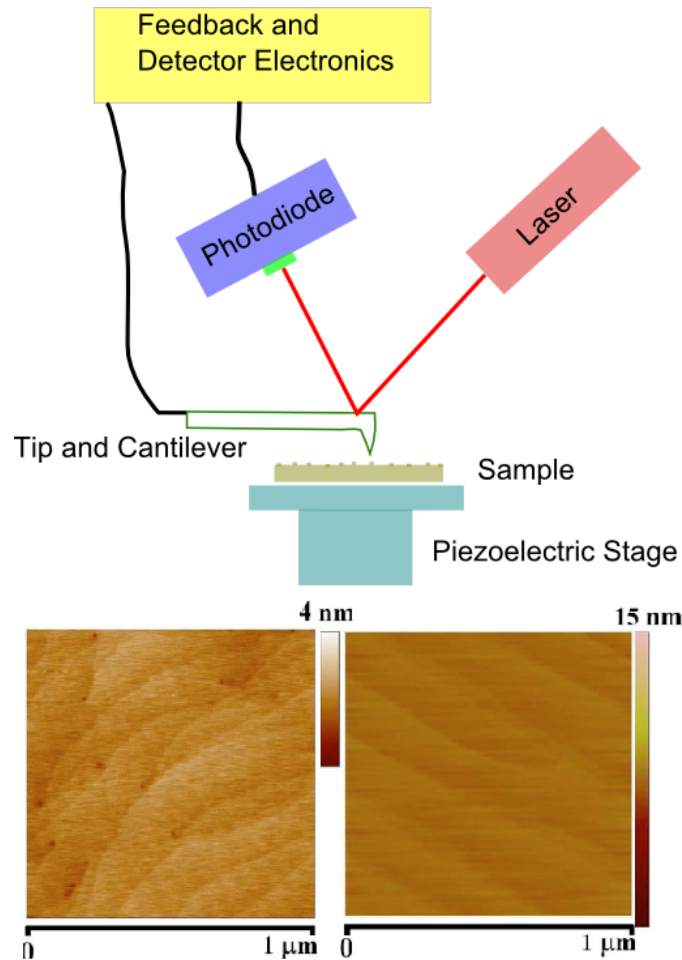


Figure 3.11: (Top) Schematic of AFM system used in this work. (Bottom) Example of GaN sample surface by AFM with a $1 \mu\text{m} \times 1 \mu\text{m}$ scan area. Screw defects and crystal plane steps are clearly visible on the left image grown with a conventional two-step method. The right image is of a GaN surface grown using the novel AlN high temperature buffer layer developed at Sheffield, showing improved crystal quality and reduced defect level [11].

A VEECO atomic force microscope (AFM) is used to obtain surface morphology information of samples. A schematic diagram of the system is illustrated in Figure 3.11

Typically this system is used in tapping mode, with a SiC μMasch cantilever and

tip of diameter ~ 10 nm. A laser in the red wavelength range is manually focused onto the SiC cantilever, with the reflected laser light focused onto a photo detector.

As the tip and cantilever are displaced by a surface morphology, the resulting change in laser reflectance measured at the photodiode is transmitted to feedback and control hardware. From this an image is constructed of the change in tip position in the z-axis as a sample is moved under the tip with very high accuracy. This change in height is converted to a scaled image with changing contrast representing a change in morphology.

AFM is used in this work both to study the surface of GaN and the surface of materials deposited onto GaN based samples.

AFM is less suited to structured surfaces, and a maximum surface roughness exists, which depending on the hardness of the surface can be between 100 - 200 nm. The tip physically touches the sample surface, meaning tips are often damaged by the hardness of GaN samples or by surfaces with roughness profiles of 100 s of nm. The vertical resolution can be very high, with observable features such as GaN crystal steps in the low nm range, as can be seen in Figure 3.11.

3.3.2 Scanning Electron Microscopy

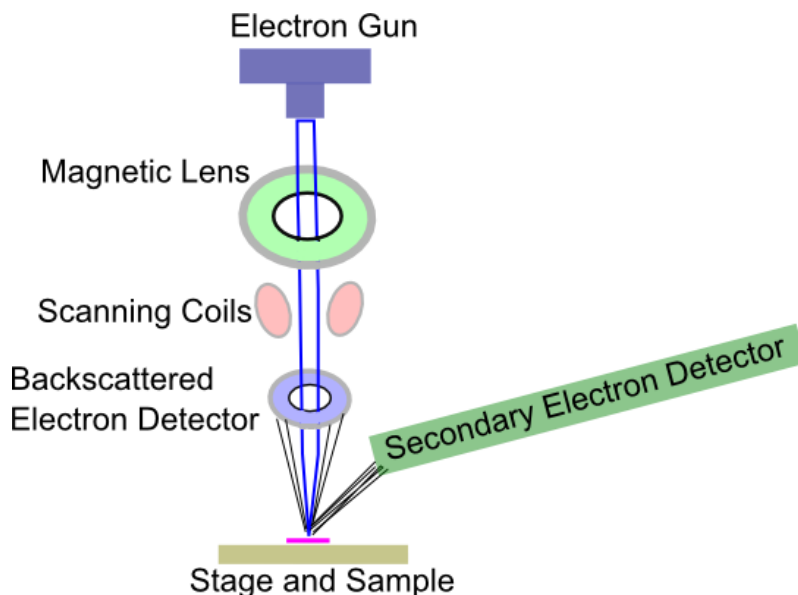


Figure 3.12: Schematic diagram of SEM system used in this work.

Fast device processing feedback can be obtained using a Philips XL30 FEGSEM. A schematic diagram illustrates the SEM procedure in Figure 3.12. An electron beam, originating from an electron gun containing a hot tungsten filament of field emission gun, is focused with apertures and magnetic fields to a sample stage. The sample is placed onto a conductive aluminium sample holder which is clipped into a

motorised transitional sample stage capable of XYZ and rotation movement. Electrons in a beam are focused to a spot several nm in diameter, and rastered across the sample in a rectangular pattern resulting in absorption and reflection from the surface. The resulting reflected electrons are detected using a backscattered or secondary electron detector to build an image of the sample.

Due to a large influx of electrons, sample charging is a problem; this can be alleviated by attaching samples to the conducting stage with a conductive sticky carbon pad, or a silver conductive permanent epoxy. Although better results are obtainable with conductive epoxy, any sample attached in this way is permanently bonded to the stage, therefore carbon pads are more readily used for fast structure feedback. Under backscattering mode, sample features can be resolved accurately to a resolution of ~ 200 nm. Further magnification often results in a blurred image due to the insulating nature of a GaN sample's sapphire substrate, allowing a build up of electrons and hence negative charge, which diverts and distorts the incoming electron beam.

Top down, angular and cross section images are used to characterise the size, shape and arrangement of various samples and nanostructures in this work.

3.3.3 X-Ray Diffraction

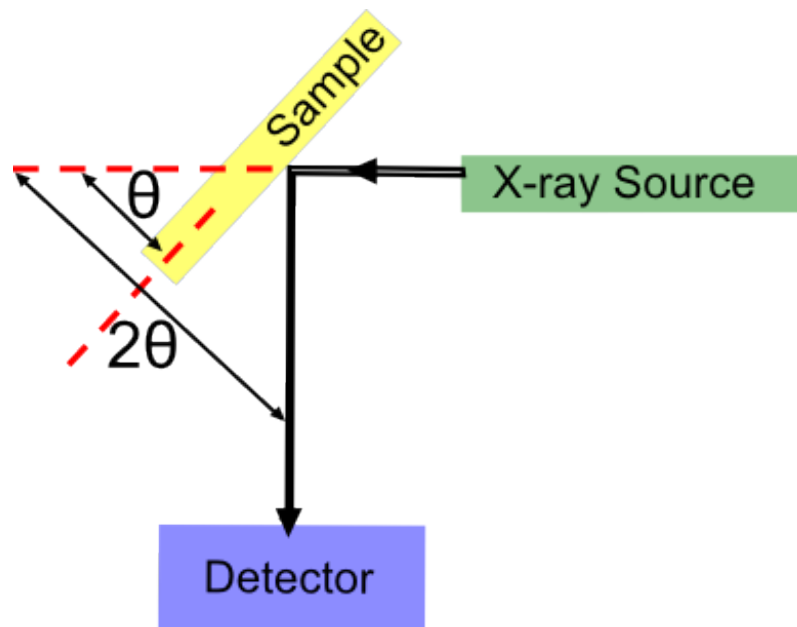


Figure 3.13: Schematic of the XRD system used in this work.

X-ray diffraction (XRD) is a widely used tool for investigating the crystal structure and quality of samples as well as strain state and thin film compositions. The atomic structure of a crystal can be determined using an incident beam of X-rays, which is diffracted by the crystal in specific directions. The intensity of the diffracted

X-rays allows the position of atoms in a crystal to be determined, and this data can be used to determine defect density and the structure of thin film layers. The X-rays incident on a crystal interact with the electrons surrounding individual atoms and are scattered, producing a detectable signal in certain directions where the scattered X-rays constructively interfere. This interference pattern can be described by Bragg's law, presented in equation 3.1, where n is the order of diffraction, λ is the X-ray source wavelength, d_{hkl} is the distance between crystal planes in the lattice with h, k, l Miller indices and θ is the Bragg angle.

$$n\lambda = 2d_{hkl} \sin \theta \quad (3.1)$$

The system used in this work is a BEDE D2000 X-ray diffraction system with a Cu X-Ray source with wavelength 0.154 nm, which is similar in magnitude to the spacing between atomic planes in a semiconductor crystal and allows significant diffraction. Electrons are bombarded onto the Cu target, creating X-rays that are focused onto a sample. The resulting diffraction of X-rays from the crystal lattice planes are detected, and by rotating the sample, a data set is produced allowing the crystal to be analysed. Two specific measurement conditions are used to obtain characteristics of a sample, ω and $\omega - 2\theta$ scans.

In an ω scan a rocking curve plot is generated by moving (or rocking) the sample around the Bragg angle θ in a small range of $\Delta\omega$. The detector is fixed at the Bragg reflection, and the intensity of the diffracted X-rays are collected and plot against $\theta \pm \Delta\omega$. The FWHM of this plot is related to the dislocation density, and allows the crystal quality to be quantified, as demonstrated by Figure 2.13 in section 2.2. The strain of a material is estimated based on the shift of the peak position of the diffraction signal, which suggests a change in lattice constant and hence strain.

For an $\omega - 2\theta$ scan, the sample is moved through a specific Bragg angle and the detector is scanned at twice the angle, allowing the thickness, composition and period of thin films and the plot of reciprocal space maps (RSM) [12]. This method is used to determine the parameters of a thin film by comparing the intensity peaks to modelled values and to the underlying substrate. RSM plots are presented in Figure 4.15 in the following chapter.

References

- ¹M. Fox, *Optical Properties of Solids*, Oxford Master Series in Physics (Oxford University Press, 2008), page 131.
- ²R. Martin, P. Edwards, R. Pecharroman-Gallego, C. Liu, C. Deatcher, I. Watson, and K. O'Donnell, "Light emission ranging from blue to red from a series of InGaN/GaN single quantum wells", *Journal of Physics D: Applied Physics* **35**, 604 (2002).
- ³C. Klingshirn, *Semiconductor optics*, Advanced texts in physics (Springer-Verlag Berlin Heidelberg, 2007).
- ⁴S. A. Campbell, *The Science and Engineering of Microelectronic Fabrication*, The Oxford Series in Electrical and Computer Engineering (Oxford University Press, 2001).
- ⁵J.-M. Lee, C. Huh, D.-J. Kim, and S.-J. Park, "Dry-etch damage and its recovery in InGaN/GaN multi-quantum-well light-emitting diodes", *Semiconductor Science and Technology* **18**, 530–534 (2003).
- ⁶E. F. Schubert, *Light-Emitting Diodes* (Boston Univ., 2002).
- ⁷H. Kim, J.-M. Lee, C. Huh, S.-W. Kim, D.-J. Kim, S.-J. Park, and H. Hwang, "Modeling of a GaN-based light-emitting diode for uniform current spreading", *Applied Physics Letters* **77**, 1903 (2000).
- ⁸D. Wu, W. Wang, W. Shih, R. Horng, C. Lee, W. Lin, and J. Fang, "Enhanced output power of near-ultraviolet InGaN-GaN LEDs grown on patterned sapphire substrates", *IEEE Photonics Technology Letters* **17**, 288–290 (2005).
- ⁹I. Y. Evstratov, V. F. Mymrin, S. Y. Karpov, and Y. N. Makarov, "Current crowding effects on blue LED operation", *Physica Status Solidi (C)* **3**, 1645–1648 (2006).
- ¹⁰O. B. Shchekin, J. E. Epler, T. a. Trottier, T. Margalith, D. A. Steigerwald, M. O. Holcomb, P. S. Martin, and M. R. Krames, "High performance thin-film flip-chip InGaN/GaN light-emitting diodes", *Applied Physics Letters* **89**, 071109 (2006).
- ¹¹S. C. Davies, D. J. Mowbray, Q. Wang, F. Ranalli, and T. Wang, "Influence of crystal quality of underlying GaN buffer on the formation and optical properties of InGaN/GaN quantum dots", *Applied Physics Letters* **95**, 101909 (2009).
- ¹²D. Bowen and B. Tanner, *High Resolution X-Ray Diffractometry And Topography* (Taylor and Francis, 2005).

Optical Investigation of InGaN/GaN Nanorod Array Structures as a Method of Improving Efficiency and Efficiency Droop Characteristics

Fabricating nanostructures is a widely accepted method of reducing the inbuilt strain and QCSE in InGaN/GaN QWs caused by internal electric fields [1, 2]. The relaxation of this strain allows enhanced performance of InGaN based emitters, and a variety of nanostructure techniques have therefore been developed to utilise this technique. The following chapter contains details of an effective self aligned mask process used to fabricate nanostructures and greatly improve the performance of devices.

4.1 Nanostructure Fabrication

Several methods of nanostructure creation exist, which fall into two broad categories. These are “top down” and “bottom up” processes.

A bottom up approach will involve growing nanostructures, normally after masking a substrate or by creating specific growth conditions to generate areas with and without growth. From here a carefully controlled growth method can result in grown GaN nanorods and LEDs incorporating InGaN QW regions. A catalyst free growth method can be accomplished by MBE, and MOCVD growth by vapour-liquid-solid techniques or on patterned templates can produce nanorod LEDs [3–5].

A top down approach utilises fabrication and etching methods to remove material from a conventional planar wafer, leaving behind nanostructures. This post-growth fabrication approach will typically begin with forming a nano-mask on a grown

wafer, followed by a dry etch process to selectively remove material and create the nanostructure [6, 7]. The use of top down fabrication methods allows greater control in the shape and size of the nanorods compared to growth techniques, and is easily scaled for large area fabrication [8].

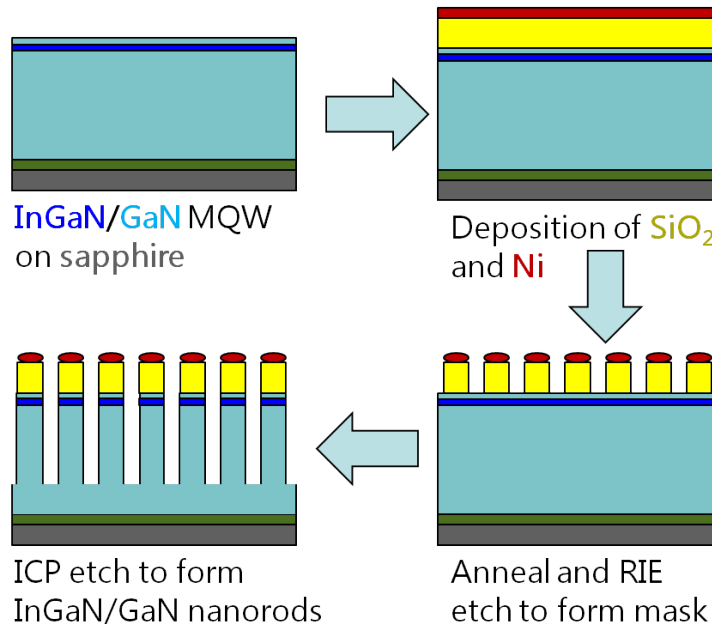


Figure 4.1: Nanorod fabrication process used in this work.

4.1.1 Nanorod Array Fabrication

The main nanorod creation process used in this work is illustrated in Figure 4.1. The nanorods created here utilise a top down approach and are fabricated using a thin annealed Ni film mask, which creates self aligned Ni nano-particles (or nano-islands) on the sample surface. The Ni particles act as a mask to allow etching around them, creating nanorods with similar dimensions. This method of nanorod fabrication involves simple and repeatable fabrication steps, and could be transferred into a commercial LED fabrication process with little need for any adaptation over a standard LED fabrication method [2].

The steps involved in the fabrication are:

- Deposition of SiO_2 planar layer by CVD techniques
- Deposition of Ni mask by thermal evaporation
- High temperature rapid thermal anneal to produce Ni nano-islands which act as a mask
- RIE dry etch of SiO_2 layer to transfer Ni nano-mask into underlying dielectric

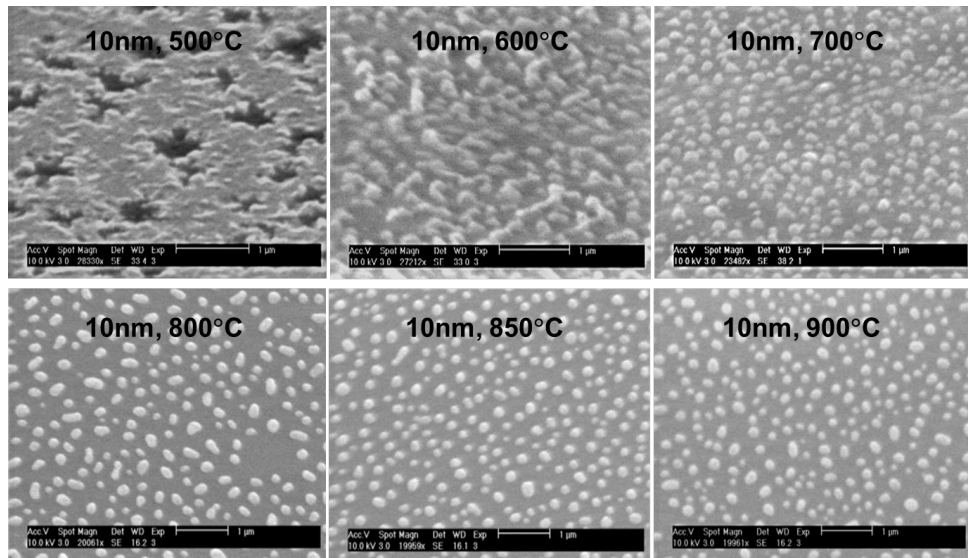


Figure 4.2: SEM images of a series of InGaN/GaN samples with a 10 nm Ni film on the surface annealed at increasing temperature in a nitrogen ambient for 1 minute.

- Removal of Ni mask with nitric acid etch
- ICP-RIE etch of GaN material to transfer mask into nanorods
- Removal of SiO₂ layer with hydrofluoric (HF) acid etch

The mask creation parameters are important as the thickness of the Ni film and annealing conditions produce a varying size nano-mask. Figure 4.2 shows 10 nm Ni films annealed at increasing temperature from 500°C to 900°C, where it is clear that the Ni nano-islands become circular and more uniform in size with increasing temperature. Temperatures above 850°C can potentially damage the InGaN/GaN QW active region in a sample and so are not readily used in this work, but little mask improvement is found beyond this temperature.

The dependence of Ni film thickness on the Ni nano-island morphology is illustrated in Figure 4.3, where a series of film thickness from 5 nm to 20 nm are annealed at 850°C for 1 minute in a nitrogen ambient. It is clear from this data that a 10 nm Ni film provides the optimal size, shape and uniformity between nano-islands, allowing uniform nanorods to be fabricated with diameter of ~ 250 nm.

A SiO₂ dielectric layer of 200 nm is initially deposited onto a sample by PECVD, which produces a smooth surface good for Ni mask creation. A thermally evaporated thin Ni film of 9 - 10 nm thickness is deposited onto this SiO₂ layer, and after annealing in a nitrogen ambient at 800°C a Ni mask is produced. The SiO₂ layer is then etched with a standard RIE system and gasses SF₆ and CHF₃ at a medium power of 80 W. This selective etch process will remove only SiO₂ and does not etch GaN or Ni, allowing the Ni mask to be transferred into a thicker and more robust

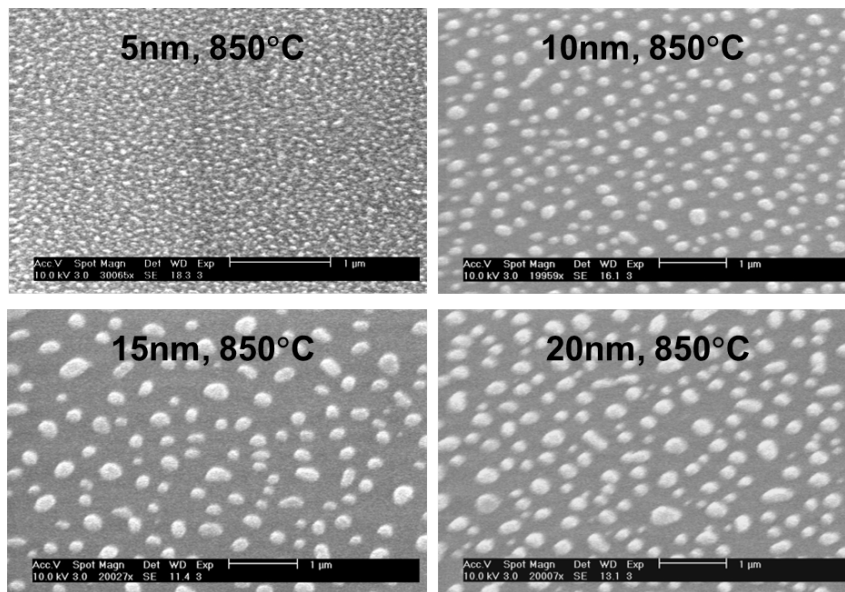


Figure 4.3: SEM images of a series of InGaN/GaN samples with increasing thickness Ni films on the surface annealed at 850°C in a nitrogen ambient for 1 minute.

SiO₂ nanorod mask with straight sidewalls. This robust mask allows etching deep into the underlying GaN structure, and also allows the initial Ni mask to be removed to avoid etch chamber contamination often encountered when using a metal mask.

The GaN material is etched with an ICP RIE system and the gasses Cl₂ and Ar, which selectively etches only the underlying GaN and InGaN material, keeping the SiO₂ mask mostly intact.

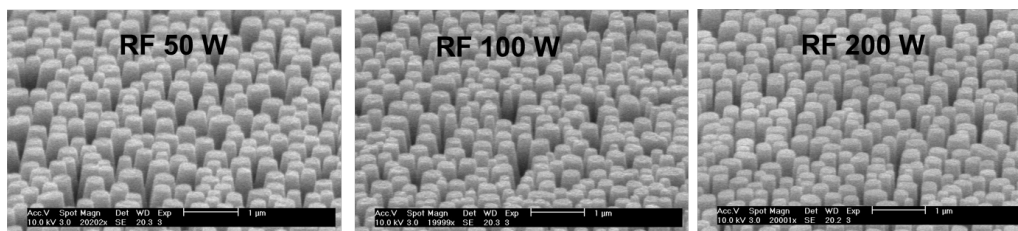


Figure 4.4: SEM images of a series of InGaN/GaN nanorod samples etched with increasing ICP RF power. A reduction in nanorod sidewall angle is observed with increasing etch power, however an increase in etch damage of the InGaN active region is expected.

The dependence of ICP etch power on the nanorod array is illustrated in Figure 4.4, where a clear relationship between sidewall profile and etch power is observed. An etch power of 50 W reduces the damage to the underlying GaN material and InGaN active region, however it produces slightly inclined nanorod sidewalls. A 100 W etch power reduces the sidewall angle, but can potentially damage the InGaN active region. A 200 W ICP etch power creates almost parallel nanorod sidewalls, however etch damage could cause a loss of performance in the InGaN active region.

The SiO₂ mask will be sputtered slowly during a GaN etch by the Ar gas and increased etch power, and a 200 nm thick mask is suitable for a GaN etch of $\sim 1 \mu\text{m}$ at an ICP etch power of 50 W. A thicker SiO₂ mask can be deposited if longer GaN nanorods are required, to reduce damage to the top of the nanorod if the SiO₂ mask is heavily sputtered.

After ICP RIE etching the SiO₂ mask is removed by HF acid wet etch processing to leave an array of flat topped GaN nanorods while causing minimal damage to the underlying sample.

4.1.2 Nano-mask Characterisation

Characterisation of the nanorods and nano-mask used during fabrication allows accurate comparisons to be made between structures. As well as using SEM and optical PL characterisation techniques, a specific image processing technique can be used to obtain data about the mask or nanorods. The public domain program used is ImageJ, developed by the US National Institutes of Health [9]. Originally designed for analysing cells and radiology images, this program works well for any similar image of particles on the nanometre size scale. The nano-masks used in this work can be accurately analysed and characterised using this program from top down SEM scans, or high resolution optical microscope images if the diameter of the structures is greater than $1 \mu\text{m}$. The density of nanorods can be calculated, as well as average size and shape variations, allowing useful comparisons to be made between fabrication runs.

Figure 4.5 shows an example image of a Ni nano-mask analysed by ImageJ showing average size and distribution as well as particle density. Beginning with a clear SEM image, the scale bar is used to set the scale in the software, allowing accurate size analysis of the particles. The image is converted to binary and threshold levels set to clearly display the particles. The image is then analysed using the software and predetermined constraints on minimum and maximum particle size and shape, which outputs an image showing each individual particle, in this case 230 Ni nano islands. Finally the output data is evaluated to give particle count, total area of the sample imaged, average size (area) of individual particles and percentage coverage. This technique allows rapid feedback regarding the Ni nano-mask used, allowing different samples to be compared.

4.2 Characterisation of As Grown Sample

The sample used initially in this work to investigate enhancements due to nanorod fabrication is a 10QW InGaN/GaN sample with structure illustrated in Figure 4.6.

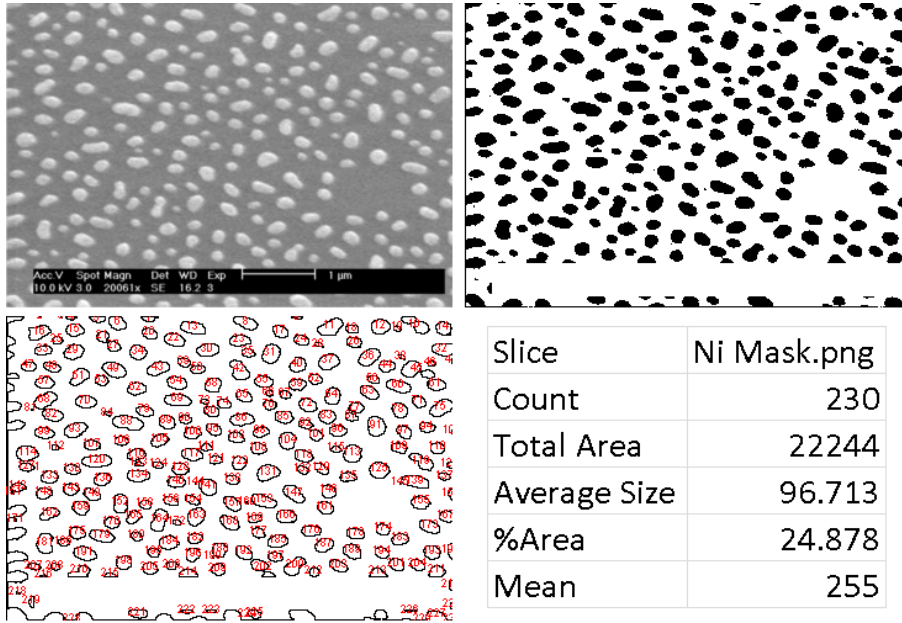


Figure 4.5: The steps involved in analysing an image using ImageJ; including creating a binary image and analysing particles using predefined constraints to form a results table of average size, area covered etc.

The emission of the planar MQW structure is shown in the right hand graph of Figure 4.6, where a clear PL spectra is observed with a peak at 450 nm. The In content of this sample is estimated by XRD to be 16% based on simulations to measured $\omega - 2\theta$ data. This is illustrated as the black plot in Figure 4.7, showing clear satellite peaks from the InGaN QW layers.

The $\omega - 2\theta$ data fit and parameters are illustrated in Figure 4.7 (red plot) and table 4.1. The QWs are estimated to be 2 nm wide, and GaN barriers 8.7 nm wide from this simulation.

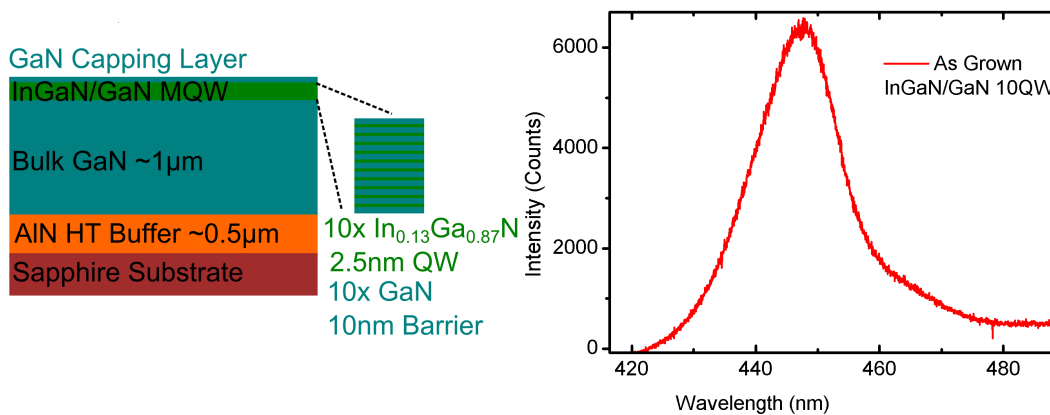


Figure 4.6: Structure (left) and PL emission at room temperature (right) of InGaN/GaN MQW sample used in this work.

| Material | Thickness (nm) | Indium Content - x | Periods |
|---------------|----------------|--------------------|---------|
| GaN | 8.7 | 0 | 10 |
| In(x)Ga(1-x)N | 2.0 | 0.16 | 10 |

Table 4.1: Simulation data used to model XRD $\omega - 2\theta$ scan.

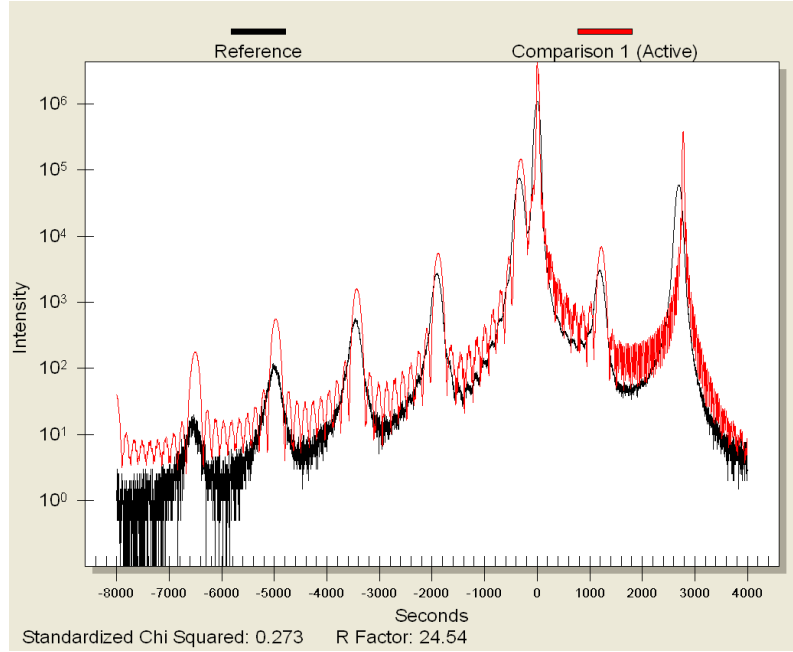


Figure 4.7: $\omega - 2\theta$ scan using an XRD system (black trace). Modelled $\omega - 2\theta$ of InGa_N 10QW structure showing a good fit to the XRD data (red trace).

4.3 Study of Internal Quantum Efficiency of Nanorod Structures

Perhaps the most important improvement offered by nanostructuring is a change of strain when the QW heterostructures are etched, causing enhanced internal quantum efficiency. This was first documented in InGa_N QW micro disks [10], where a partial reduction in strain is found which reduces the in-built piezoelectric field in a QW. As the diameter of the structures is reduced to a nanorod scale, further reduction in strain is recorded [11, 12].

The strain in the QW structures causes a reduction in the InGa_N QW optical performance due to the QCSE as discussed in section 2.5. This results in a red shift in the peak emission wavelength, and reduced overlap of the electron and hole wave functions, reducing the number of carriers recombining radiatively. The disruption of the lattice by etching the sample into nanorods allows the crystal structure to relax outwards, relieving some of the inbuilt strain. This produces a blue shift in the spectra of the nanorod sample emission, and an increase in emission intensity due to a more efficient recombination process, as illustrated in Figure 4.8.

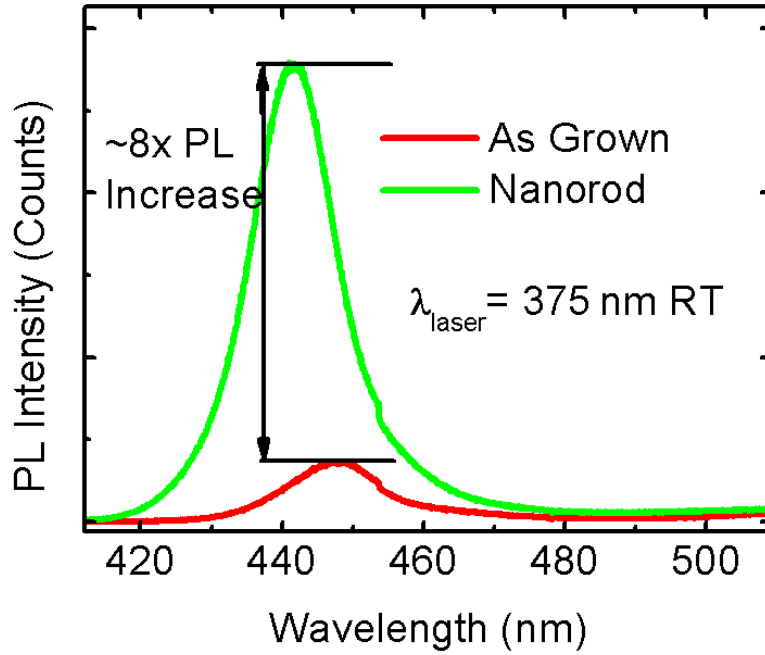


Figure 4.8: PL increase and peak emission blue shift in an InGaN/GaN MQW structure after nanorod processing.

The reduction in strain caused by the nanorod fabrication allows the electron and hole wave functions, previously separated by the QCSE, to overlap further as the band structure tilt is reduced. This increases the recombination rate by allowing increased direct carrier recombination to optical modes [13]. As the In content of a QW structure increases, the InGaN crystal structure lattice constant expands further, creating a higher level of strain. Because of this, green wavelength QWs with higher In content show increased strain relaxation (and hence radiative emission enhancement) and increased peak wavelength blue shift when nanorod processed [2]. This is further illustrated in the data in Figure 4.17 discussed in the next section.

Temperature dependant PL can be used to quantify the increase in internal quantum efficiency (IQE) over any increase found due to extraction efficiency. The IQE of a material is the ratio of excited carriers to the carriers that recombine to emit a photon. In a structure such as an InGaN/GaN QW or array of QWs, as temperature is reduced, the emission efficiency of the wells will increase.

With the capability to reduce temperature to below 10K in a helium cryostat, loss mechanisms such as defects and phonons are almost completely frozen out as carriers are localised, leaving a structure with high efficiency [14, 15]. If the temperature is raised, the loss in efficiency can be observed as a loss in spectral intensity, allowing the room temperature efficiency to be estimated based on the assumption that low temperature efficiency is very close to 100%. Plotting an Arrhenius graph of the normalised integrated PL intensity data with changing temperature allows

the change in efficiency between various samples to be investigated [1]. This is illustrated in equation 4.1, where η_{IQE} is the efficiency of the structure and $I_{300\text{K}}$ and $I_{10\text{K}}$ are the integrated PL intensities at 300K and 10K respectively.

$$\eta_{\text{IQE}} = \frac{I_{300\text{K}}}{I_{10\text{K}}} \quad (4.1)$$

Initially the nanorod and planar as grown samples are cooled to 10K and PL measurements are taken. They are then heated to 300K (\sim room temperature) at 10K intervals and spectra are obtained at each temperature. The excitation laser position remains constant for the duration of the experiment, to ensure the exact point on a sample is measured at each temperature. Integrating the gathered spectra and plotting this on an Arrhenius graph of inverse temperature against normalised integrated PL allows the IQE of a sample to be estimated, as shown in Figure 4.9.

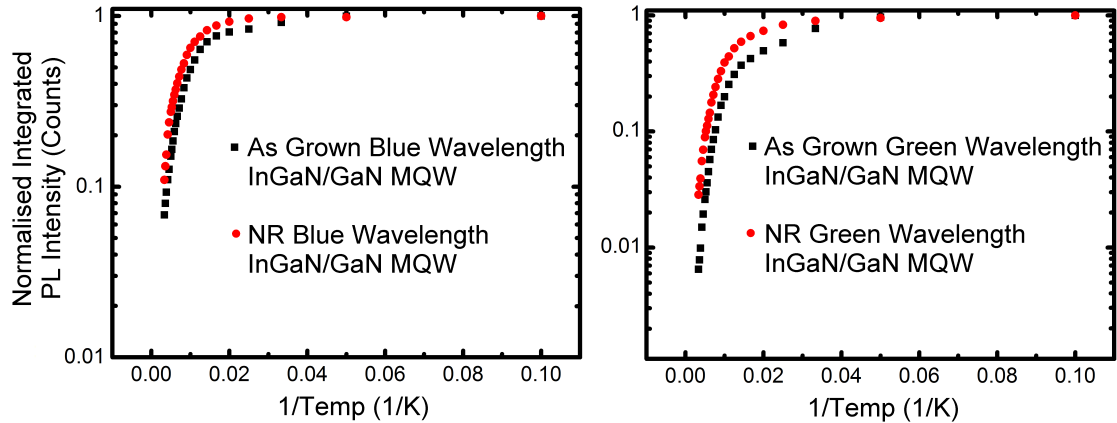


Figure 4.9: Arrhenius plots of temperature dependant PL for a blue and green wavelength as grown sample and corresponding NR fabricated structure.

Figure 4.9 shows temperature dependant PL plots of blue and green InGaN/GaN 10QW samples, showing an increase in IQE after nanostructuring for both wavelength ranges. The blue sample is increased from 6% for an as grown sample to 10% IQE after NR processing, an almost doubling of the radiative efficiency of the structure. The green sample shows a larger increase, with the IQE of the as grown sample being 0.65% compared to 2.5% after nanorod fabrication.

Figure 4.10 shows the PL spectra for a blue wavelength as grown sample (left) and NR fabricated sample (right), showing a clear increase in emission intensity and narrower linewidth with the NR structure. The linewidth narrowing is possibly due to a change in the exciton-LO phonon coupling, and is discussed later in this chapter.

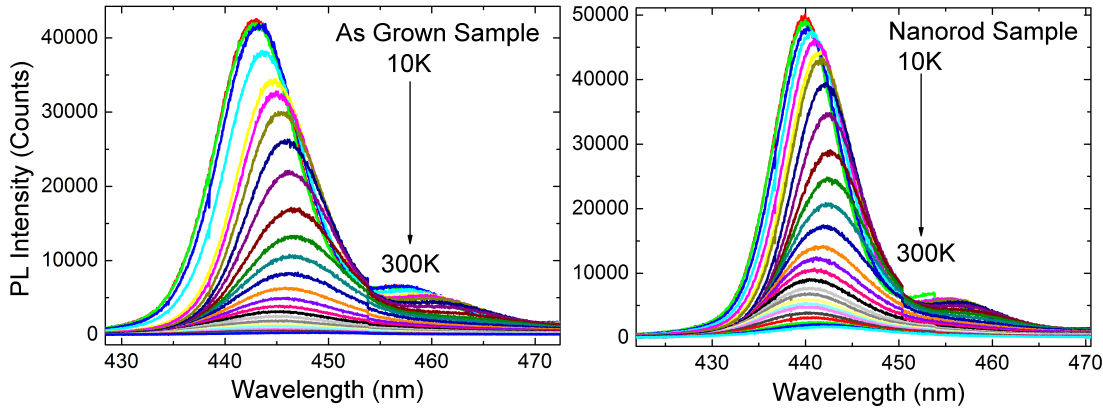


Figure 4.10: PL Spectra obtained at temperatures between 10K and 300K of a blue emitting InGaN MQW as grown and NR sample.

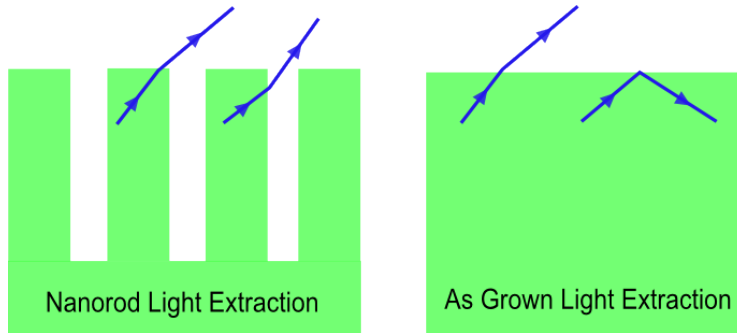


Figure 4.11: Example of light extraction improvement with a nanorod structure due to a reduction in internal reflections.

4.3.1 Increased Extraction Efficiency

The difference in enhancement rate between standard PL measurements in Figure 4.8 and the IQE enhancement in Figure 4.9 is due to the altered shape of the sample surface after nanorod fabrication. A change in light extraction efficiency is found when changing the emitting surface of a sample from an epitaxial flat surface to a structured or roughened one [5]. The nanorod fabrication technique used in this work effectively roughens the surface of the sample and allows light to propagate out through the nanorods at angles that would be internally reflected with a flat surface, as illustrated in Figure 4.11.

This result is demonstrated in angular resolved PL measurements performed on a green wavelength InGaN/GaN MQW sample in Figure 4.12, where the extraction angle is seen to increase from 26° for an as grown planar sample to 40° with a nanorod sample fabricated using a self aligned Ni mask. The top graph shows a measurement from 0° to 90° of the normalised intensity of a sample excited by a 375nm laser. The black line showing the as grown sample has a clear substrate mode at a very shallow angle around $\sim 5^\circ$ and a cone of light increasing in propagation at higher angle. The

red line representing the nanorod structure shows increased emission at almost all angles. No substrate mode is observed for this sample, as the substrate cavity has now effectively been disrupted by the nanorod etching process. The lower plots show wavelength intensity with angle, again showing the nanorod sample has an increase at all angles as well as an increase in overall emission efficiency.

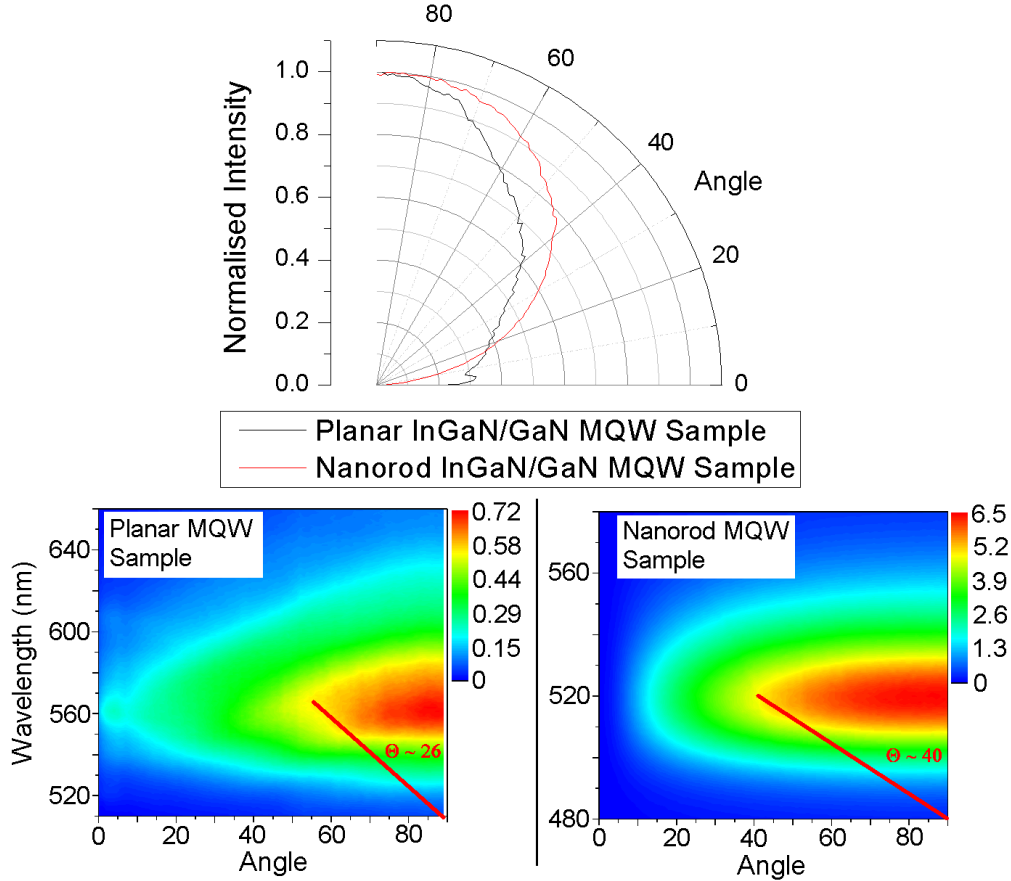


Figure 4.12: (Top): Angular resolved PL measurements showing increased extraction efficiency of a green wavelength InGaN/GaN MQW nanorod sample compared to as grown planar sample. (Bottom): Two plots of photoluminescence intensity spectra with angle for nanorod and as grown samples showing a clear increase in emission for the nanorod sample at all angles.

A further explanation for the difference between the 8x increase observed for standard PL measured in Figure 4.8 and the 2x increase in IQE in Figure 4.9 is a change in laser absorption during the PL measurement. The shape of the nanorod structure could cause an increased laser absorption by the QWs, due to the increased surface roughness causing laser scattering and reflections not present with an epitaxially flat as grown sample.

This becomes apparent in Figure 4.10, where the emission from the nanorod sample at 10K is higher than the as grown sample at the same temperature. As both samples are assumed to be approximately 100% efficient at this low temperature, any increase in emission is due to an increased light extraction or laser absorption.

4.4 PL Investigation of Localisation in Nanostructures

A so called “s-shift” in peak wavelength is observed in Figure 4.10, due to carrier de-localisation as the sample is heated from 10K. This is highlighted in Figure 4.13 where peak wavelength values are plot against temperature [16].

The s-shift due to localised states presents itself first as a red shift in peak emission wavelength as carriers hop between localisation states. Due to the low thermal energy at temperatures below 100K, carriers in the shallowest localisation centres can escape. They are then captured by other deeper localised minima, resulting in a reduction of the emission energy. This is also enhanced by the dominance in radiative recombination at this temperature range (when IQE is very high and lifetime is long), which results in carriers having more time to relax to band minima before recombining.

When temperature $T = \frac{E_0}{k_B}$ (where E_0 is the bandgap energy at absolute zero and k_B is the Boltzmann constant), the carriers have equal chance of escaping a shallow localisation state and being captured by another state at higher or lower energy. As temperature increases carriers are thermally excited into higher localisation centres, resulting in a blue shift in emission wavelength. Along with this mechanism, the reduction in lifetime due to non-radiative recombination results in carriers recombining before reaching the band minima.

Finally at temperatures above 200K bandgap shrinkage occurs as a result of thermal expansion which begins to red shift the emission peak.

Very little change in peak wavelength shift with temperature is observed between planar as grown and nanorod structures, suggesting nanorod fabrication does not change the localisation mechanisms in the InGaN QWs.

A slight reduction in the carrier hopping process is observed in the NR sample at temperatures between 10K and 100K. At this temperature range, carriers may obtain enough energy to overcome a shallow localisation point, however they then may fall into deeper localisation states, causing an initial red shift in emission energy. A strained QW (such as the as grown sample here) is tilted as previously discussed due to the field across the well and resulting QCSE. The carriers escaping a shallow localisation point in a strained QW are more likely to fall down the tilted QW into deeper localisation states. A NR sample however has partially unstrained QWs, causing a reduction in the QW tilt due to the reduced piezoelectric field. As a result there is a reduced initial red shift due to carriers overcoming shallow localisation states and falling into deeper ones.

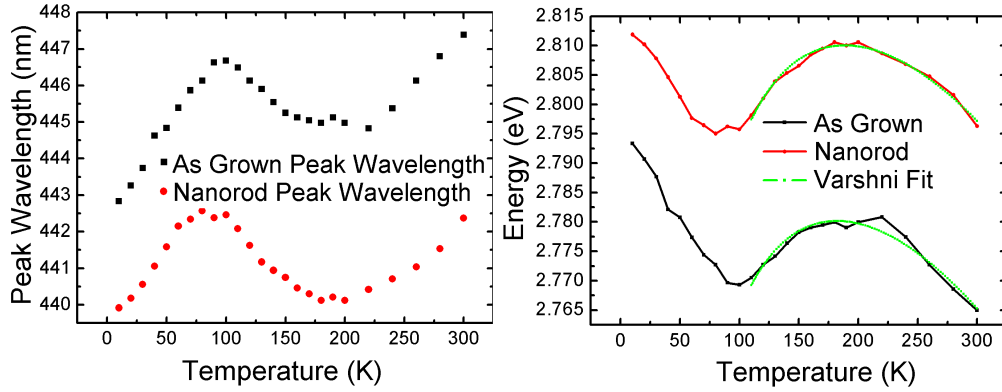


Figure 4.13: Peak wavelength shift with temperature for blue emitting InGaN as grown and NR samples.

| Sample | $E_g(0)$ (eV) | α (meV) | β (K) | σ (eV) |
|----------|---------------|----------------|-------------|---------------|
| As Grown | 2.836 | 0.591 | 741.46 | 0.0236 |
| Nanorod | 2.866 | 0.561 | 792.92 | 0.0241 |

Table 4.2: Varshni fitting parameters of the temperature dependant peak wavelength s-shift for an as grown sample and corresponding nanorod structure.

4.4.1 Varshni Fitting

The de-localisation of carriers above 100K due to increased thermal energy shows little change between nanorod and as grown samples. This is demonstrated in Figure 4.13 on the right hand graph, showing Varshni fitting lines in green to the peak wavelength with temperature data (wavelength converted to energy). The fit uses the modified Varshni fitting equation 4.2, allowing an estimation of the localisation degree [17].

$$E_g(T) = E_g(0) - \frac{\alpha T^2}{\beta + T} - \frac{\sigma^2}{k_B T} \quad (4.2)$$

From equation 4.2, $E_g(0)$ is the peak emission energy (bandgap energy) at absolute zero temperature, α and β are the standard Varshni fitting parameters and σ is the fitting parameter related to localisation degree.

The results of Varshni fitting to the temperature dependant s-shift in peak wavelength are illustrated in Table 4.2. The α , β and σ values are largely unchanged, suggesting the exciton localisation effect remains fairly constant between samples. This is to be expected, as the samples are from the same wafer. This does suggest however that a reduction in QCSE in the nanorod sample improves emission efficiency by reducing strain, but does not change the de-localisation of carriers due to temperature above 100K.

4.4.2 In-Plane Exciton Localisation in Nanorods

A significant change in the radiative decay time is observed with nanorod processed samples. This is demonstrated with time resolved photoluminescence measurements performed with similar structures and fabrication methods to the ones used in this work by Liu et al [18]. Three InGaN/GaN 5QW samples with In content between 10% and 30% were grown under identical conditions other than with a change in precursor flow and temperature for the heterostructure growth section. Nanorod fabrication was performed using a self aligned Ni mask process as detailed earlier in this chapter, and time resolved photoluminescence data was acquired using a time correlated single photon counting detector coupled to a Horiba spectrometer with a 375 nm pulsed laser excitation source with a minimum pulse width of ~ 80 ps.

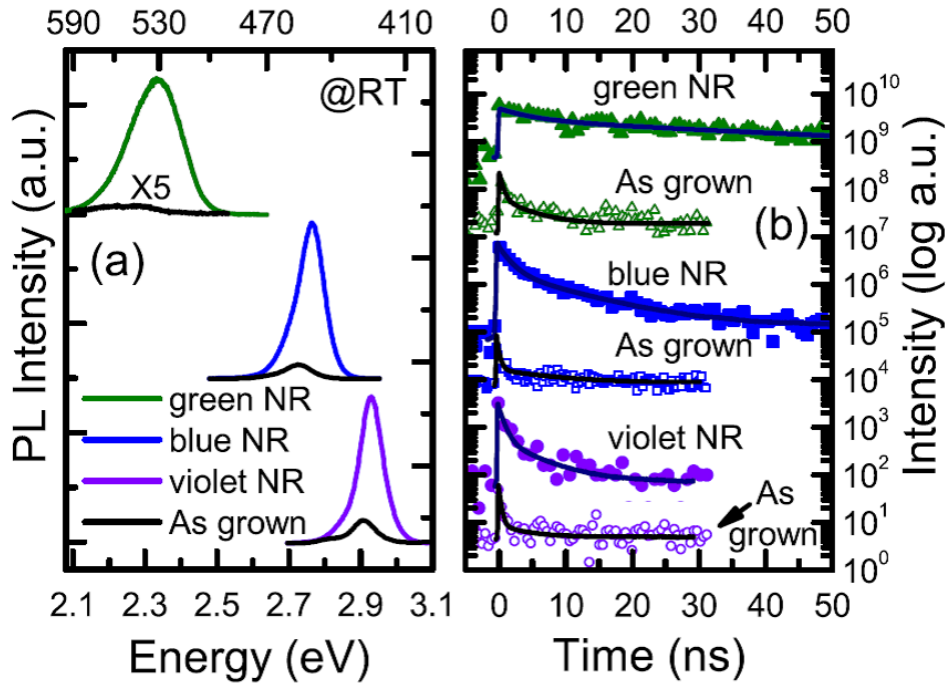


Figure 4.14: (a) Room temperature PL spectra of violet, blue, green NR and corresponding as grown samples. (b) TRPL decay traces of the as grown and corresponding NR structures. The symbols represent the sample decay line and the solid lines are modelled decay traces fitted to the gathered data using a typical bi-exponential model. Reprinted with permission from [18].

As shown on the left of Figure 4.14, the PL intensity of the nanorod samples shows a large increase over a planar structure from the same wafer. As discussed earlier in this chapter, with increasing In content, the enhancement factor between NR and as grown increases, with the green wavelength sample showing a very large increase due in part to the large inbuilt strain found in the planar sample, which is reduced by NR fabrication.

The time decay for each sample shown on the right of Figure 4.14 demonstrates

a change in lifetime characteristics between NR and planar samples. The NR decay traces all show an increase over the as grown planar sample from the same wafer, suggesting a longer radiative decay lifetime after NR processing. This phenomena is explained due to the carrier diffusion length in InGaN QWs of over 250 nm, compared to the average NR diameter of ~ 220 nm. The density of defects resulting in non-radiative recombination centres is high for InGaN heterostructures, and spacing is usually in the sub μm scale. Due to the disruption of the QWs on the nm scale after NR fabrication, generated excitons have extra in-plane confinement, and therefore a lower chance of diffusing to a defect and recombining non radiatively. This increases the number of carriers available that can emit radiatively, increasing the optical efficiency.

4.5 Study of Strain Relaxation

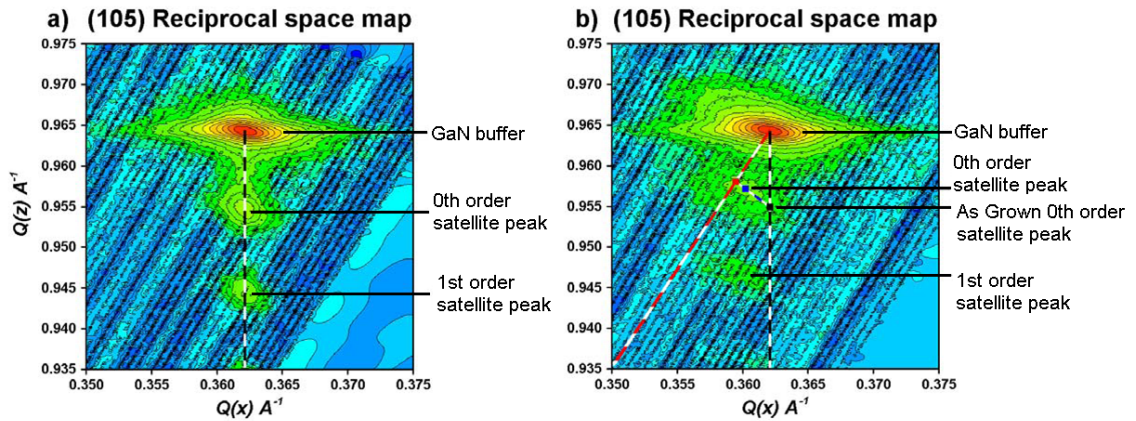


Figure 4.15: XRD reciprocal space maps of InGaN/GaN as grown epiwafer (left) and nanorod etched (right) structures. A strong peak is observed for the underlying GaN buffer layer, with lower intensity satellite peaks below corresponding to the InGaN/GaN MQW structure. The black dashed line represents the lattice constant of the underlying GaN material. The red dashed line represents the theoretical lattice constant of fully relaxed InGaN, increasing with In content.

The reduction in strain in a nanorod sample can be measured with X-ray diffraction (XRD), as shown in Figure 4.15. Measuring the reciprocal space maps of a nanorod and as grown epiwafer allows the underlying bulk GaN and InGaN QW satellite peaks to be observed. For the as grown sample, the bulk GaN satellite peak has the strongest intensity, and has satellite peaks corresponding to the InGaN QWs directly below it. As these peaks are all in line (linked by the black dashed line), it can be assumed that the QW has the same lattice constant as the underlying bulk GaN layer. In this instance, as the QW lattice constant is compressed to that

of the underlying layer, the QWs are completely strained to the maximum for an InGaN/GaN heterostructure. For the nanorod etched structure on the right in Figure 4.15, the same high intensity bulk GaN peak can be observed, but the InGaN QW satellite peaks are now shifted away from the black dashed “fully strained” line towards the red dashed line. This line is the theoretical fully relaxed line for InGaN material with increasing In content. If the first InGaN satellite peak lies on this line, the lattice constant will be that of unstrained InGaN, and as such the InGaN QW causing the satellite peak would be fully relaxed. The shift of the InGaN QW satellite peaks can be quantified into a strain relaxation value by obtaining lattice constants and using equation 4.3, where $a(L)$ is the real lattice constant of the layer (InGaN QW), $a_o(L)$ is the theoretical lattice constant of the layer, and $a_o(S)$ is the real lattice constant of the substrate (underlying bulk GaN).

$$R = \frac{a(L) - a_o(S)}{a_o(L) - a_o(S)} \quad (4.3)$$

The values of lattice constant found from the satellite peaks, and theoretical constants from literature, can be used to obtain a value of strain relaxation as a percentage. Typically, values of up to 80% strain relaxation are observed for the individual QW structures in a nanorod compared to their as grown counterpart.

As previously discussed, the increase in emission and sample blue shift due to nanostructuring can be explained by a reduction in strain due to a disruption of the crystal structure [13]. Further modelling and electron microscopy work has concluded that a QW in a nanorod may have a strain profile, consisting of lesser strained QW material on the nanorod edge, and a higher strain towards the centre [19].

4.6 Reduction in Longitudinal-Optical Phonon - Exciton Interaction

4.6.1 Background

As discussed in chapter 2; when exciton recombination occurs in an InGaN quantum well structure, a localised electron and hole will produce a photon of a specific energy. This energy can have a broad range, due to recombination mechanisms and In fluctuations in the well, giving rise to a broad PL spectrum. An exciton can also couple with a phonon during recombination, where the phonon provides momentum to allow electrons and holes to recombine.

This phonon-exciton interaction will reduce the energy of the emitted photon by the phonon energy, which typically results in a small reduction of 10 s of meV. Phonon-exciton coupling will occur for a proportion of the recombining carries, depending on the localisation and strain of a particular QW structure. The result of the interaction are sidebands or replicas of a main PL peak at a reduced energy. The sidebands appear similar in shape to the main PL peak, but are reduced in intensity and shifted in wavelength by the phonon energy. The most common phonon-exciton coupling process for InGaN QW structures is via a longitudinal-optical (LO) phonon, which produces a photon energy reduction of ~ 90 meV in GaN. Figure 4.16 shows an example of LO phonon replica side peaks on a log scale, where clear Gaussian peaks are observed. At this wavelength range, a 90 meV energy red shift from 450 nm corresponds to 464 nm, suggesting the satellite peaks found here are a result of LO phonon interaction.

Previous studies in InAs QDs on a GaAs surface have shown a relationship between increased phonon-exciton interaction and the piezoelectric effect causing strain in crystals. Exciton localisation is also discussed as a mechanism that enhances the interaction [20]. These two effects become pronounced in InGaN systems, where the large inbuilt piezoelectric field results in a strong interaction between excitons and phonons, especially as a larger quantity of In is incorporated to reduce the bandgap of a structure and hence increase emission wavelength [21]. This has been demonstrated experimentally by Martin et al. [22] and Kalliakos et al. [23] on a series of samples with increasing In content, where the change in exciton-phonon coupling is at least partly linked to changes in strain.

4.6.2 Investigation of Phonon-Exciton Coupling

An important observation made after fabricating an InGaN QW planar structure into nanorods is an apparent reduction in the phonon satellite peaks, suggesting a reduction in LO-phonon - exciton interaction in these structures.

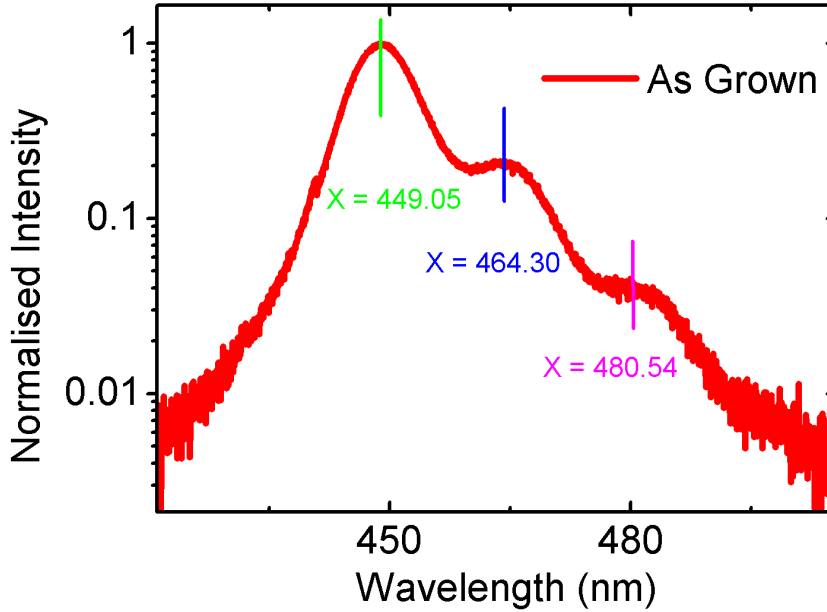


Figure 4.16: PL spectra of an as grown 10 QW blue InGaN/GaN structure. Clear satellite peaks (with central wavelength labelled) are observed to the right of the main PL peak.

| As Grown Peak Wavelength (nm) | Indium Content (%) | FWHM (nm) |
|-------------------------------|--------------------|-----------|
| Sample 1: 423 | 10 | 8.3 |
| Sample 2: 449 | 13 | 9.0 |
| Sample 3: 470 | 17 | 12.6 |
| Sample 4: 502 | 23 | 18.2 |

Table 4.3: Characteristics of four as grown samples used to study phonon-exciton interaction in nanorod structures.

To investigate this further, a series of four samples with different In content and hence emission wavelength were fabricated into nanorod structures. Characteristics of the as grown planar samples are presented in Table 4.3, showing a wide range of In content spanning the blue to green emission wavelength range.

After nanorod fabrication, the PL of the as grown and nanorod structures is measured at 10K to allow clear observation of the phonon replica side peaks. A clear change in the phonon replica intensity can be observed in normalised PL measurements in figure 4.17.

The phonon-exciton coupling strength can be quantified analytically using the ratio of the main and satellite peaks (obtained by data fitting) and the Huang-Rhys factor.

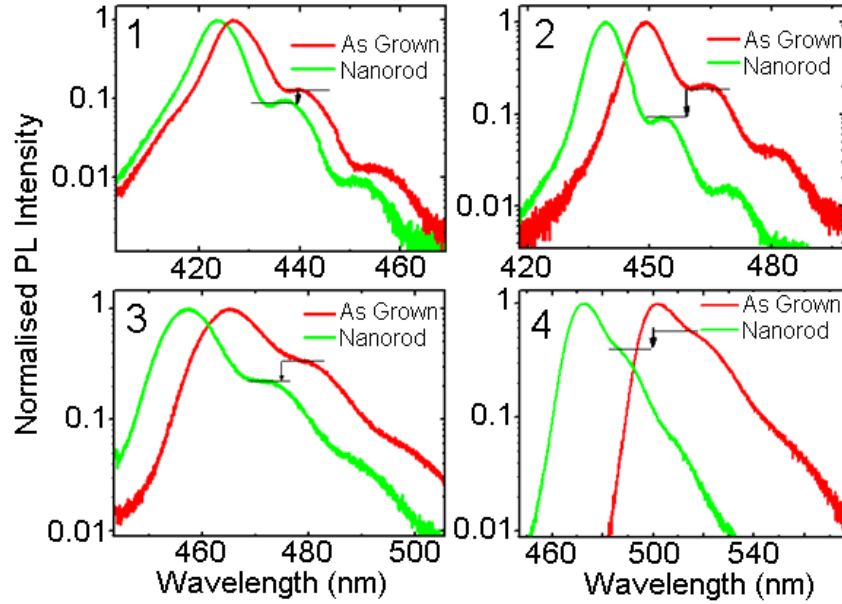


Figure 4.17: PL spectra of four samples with increasing wavelength and In composition. Peak wavelength is 423nm, 429nm, 470nm and 502nm corresponding to sample 1, 2, 3 and 4 respectively. The as grown spectra (red line) and nanorod spectra (green line) are taken at low temperature (10K) and normalised on a log scale. Clear phonon replica satellite peaks are observed, and the nanorod samples show a clear reduction in side peak intensity.

Analysing Exciton-Phonon Coupling with the Huang-Rhys Factor

The Huang-Rhys (HR) factor can be used to quantify the size of the sideband or phonon replica peak observed in a spectra [24]. This ratio can give the coupling strength between excitons and LO-phonons for a particular sample.

The HR factor is given by equation 4.4, where I is the integrated intensity of each Gaussian curve (either main PL peak, or subsequent phonon side peaks), n is the side peak number and S is the Huang-Rhys factor [25].

$$\frac{S_n}{n+1} = \frac{I_{n+1}}{I_n} \quad (4.4)$$

To obtain the area under each Gaussian peak in the PL spectra, multiple Gaussian peak fitting is employed on the data using equation 4.5.

$$y = y_0 + \frac{A}{w\sqrt{\frac{\pi}{2}}} \exp^{-2\frac{x-x_c}{w}} \quad (4.5)$$

The standard Gaussian function in equation 4.5 is composed of the following components: A is the area of the peak, x_c is the central wavelength of the peak and w is the peak width (FWHM).

To ensure an accurate fit, the separation between the peaks (difference between x_c in equation 4.5) is assumed to be approximately 90 meV, the well documented

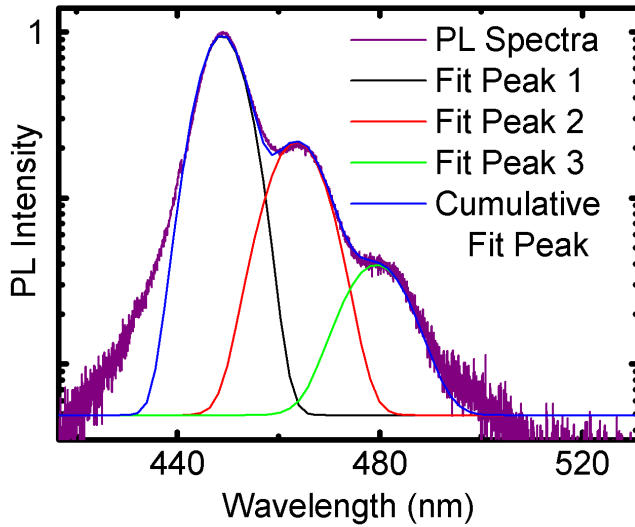


Figure 4.18: Normalised spectra of an as grown InGaN/GaN MQW structure on a log-linear scale showing clear satellite peaks. Three Gaussian peaks are fitted to the data, allowing the area under each peak to be estimated for HR factor calculation.

| Area (Normalised Counts) A | Centroid (nm) x_c | FWHM (nm) w |
|------------------------------|---------------------|---------------|
| Main Peak: 9.54048 | 448.8 | 8 |
| 1st Satellite Peak: 2.6721 | 463.3 | 10 |
| 2nd Satellite Peak: 0.50935 | 479.3 | 11.7 |

Table 4.4: Fitting parameters of three Gaussian peaks of an as grown sample illustrated in Figure 4.18.

GaN LO-phonon energy [26]. As shown in Figure 4.18, accurate data fitting can be accomplished to obtain individual peak area, used to calculate HR factor. The calculated fitting parameters are displayed in Table 4.4.

Several studies have shown that increasing In composition leads to increased phonon coupling [22, 23]. This is because with increased In composition, the inbuilt piezoelectric strain increases, along with exciton localisation. This results in an increase in the coupling of localised excitons to phonons, and hence an increased HR factor. Typically HR factors as high as 0.6 are observed with InGaN/GaN structures [27, 28], compared to 0.014 found in a typical InAs/GaAs system with very low strain [20], which further highlights the relationship between a high degree of strain in an InGaN system and coupling between phonons.

After fitting each sample, the S_0 values of HR factor in Table 4.5 are obtained. This is in agreement with literature that, as strain is increased with increasing In composition, the phonon-exciton interaction increases. It is also clear from Table 4.5 that when a structure is nanorod processed, the HR factor, and hence phonon-

| As Grown Peak Wavelength (nm) | As-Grown S_0 | Nanorod S_0 |
|-------------------------------|----------------|---------------|
| 423 | 0.15 | 0.11 |
| 449 | 0.30 | 0.26 |
| 470 | 0.44 | 0.40 |
| 502 | 0.58 | 0.36 |

Table 4.5: Table of S_0 (Huang-Rhys factor) values for as grown and nanorod samples with increasing emission wavelength.

exciton coupling, is significantly reduced [29].

The higher order satellite peaks (caused by interaction with multiple phonons during emission) also show a reduction in phonon-exciton coupling for all samples after nanorod processing, as observed in Figure 4.17. The magnitude of peaks S_1 and S_2 is observed to decrease after nanorod processing at approximately the same rate as the reduction in S_0 , suggesting a decrease in multiple phonon-exciton coupling events. Obtaining calculated data for these peaks is problematic due to difficulties encountered in fitting the second and third satellite peaks for the longer wavelength samples (due to increased overlap as FWHM increases) as well as reduced intensity due to the low efficiency of green emission InGaN QWs, however the blue wavelength samples show a similar reduction for higher order satellite peaks [28].

4.7 Reduction of Efficiency Droop in Nanorods

Reducing efficiency droop in a GaN based LED is a major challenge currently facing III-nitride development [30]. The current state of the art high power LEDs operate at significantly below their maximum efficiency as a result of running at high injection current. Some LEDs may droop to half their maximum internal quantum efficiency when operating at their rated current. Recent work has suggested that Auger recombination is the primary cause of efficiency droop in InGaN based devices [31]. Although other issues such as carrier overflow, crystal quality and increased device heating also contribute to reduced efficiency at high current density.

Kioupakis et al. [32] recently confirmed that the majority of Auger recombination is via an indirect process assisted by phonons. The basis behind indirect Auger recombination (IAR) is a phonon interaction that provides the momentum required for an exciton to promote a third carrier, instead of emitting a photon. This process appears as a result of QCSE in InGaN heterostructures, where the separated wave functions of electrons and holes due to piezoelectric fields in the structure require a change in momentum to recombine (provided by a phonon interaction). Several different phonon-exciton interactions are said to contribute to IAR, and LO-phonons

make up a significant part of this [32].

To investigate the influence a reduction in LO-phonon-exciton coupling has on efficiency droop, a series of high power PL measurements were performed after nanorod processing on a 10QW InGaN/GaN sample with central emission wavelength of 449 nm.

A 266 nm Nd:YAG high power pulsed laser is used, with short pulse width as low as 9 ns and repetition rate of 850 Hz. This ensures a very high excitation power is incident onto the sample during a pulse, potentially over 2 MW/cm^2 , but allows the sample to cool between pulses, minimising damage to the structure. A large range of excitation power is used, between approximately 2 kW/cm^2 and 2 MW/cm^2 , with PL spectra obtained at each power interval.

The integrated intensity of each PL spectrum can be plot as the intensity divided by the input excitation power. This calculation does not give an accurate value of efficiency, but provides a relative value and allows the change in efficiency to be observed between different excitation power levels, if all other parameters remain constant. This method allows an observation of efficiency droop to be made without knowing exact values for input and output collected optical power, which is difficult to accomplish with PL testing [33].

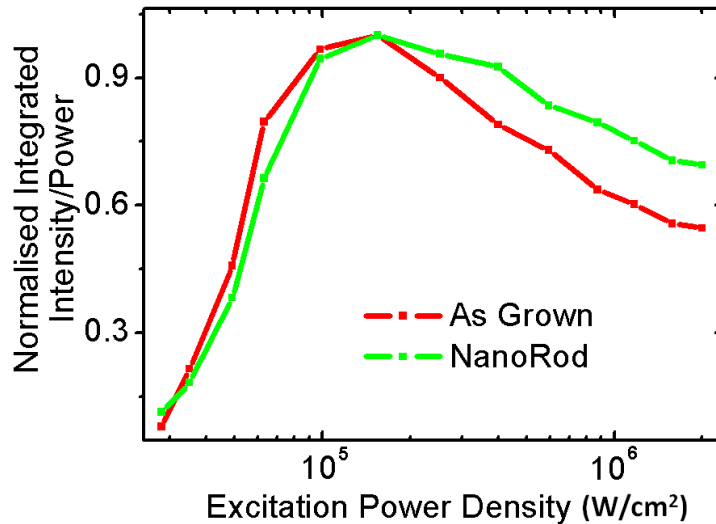


Figure 4.19: Change of efficiency with excitation power for a nanorod and corresponding as grown sample. A clear rise in efficiency is observed at low power density, followed by a fall or droop in efficiency at high power density.

Figure 4.19 illustrates the efficiency droop of as grown and nanorod InGaN MQW samples emitting in the blue wavelength region. The data is normalised, and an increase in efficiency is observed at low excitation power, followed by a peak and then a reduction in efficiency at high power.

The nanorod sample shows a clear alleviation of efficiency droop compared to the as grown sample, as a result of a reduction in the LO-phonon exciton interaction previously discussed. This result has important consequences for future LED development by improving efficiency droop and allowing devices to operate more efficiently at higher operating power.

4.8 Conclusions

In summary, a nanorod fabrication process has been developed based on a Ni self aligned mask which results in enhanced optical emission from InGaN/GaN heterostructure samples. An initial study on a blue wavelength sample illustrated strong enhancement due to nanorod array fabrication. The internal quantum efficiency is found to increase as a direct result of strain relaxation due to nanorod creation, and exciton localisation has been studied, where a change in in-plane localisation is found. The reduction in strain in the structures is quantified using XRD analysis, showing a clear relaxation of the InGaN heterostructure in the nanorods.

A series of InGaN/GaN MQW nanorod array structures have been fabricated with different In content (corresponding to different central emission wavelength) in the blue to green wavelength range. Detailed optical characterisation was carried out on the nanorod samples and their corresponding as-grown counterparts, where in all cases, clear phonon replica peaks are observed. A reduction in the replica peak intensity is discovered for all nanorod fabricated samples compared to the corresponding as grown samples.

The phonon replica characteristics are analysed by data fitting, where a multiple Gaussian function is fitted to all PL spectra, allowing values of the phonon replica amplitude, central wavelength and FWHM to be extracted. The HR factor is calculated using this data, and shows a clear reduction in HR factor for all the nanorod structures compared to their corresponding as grown samples. This suggests that all nanorod samples have reduced LO-phonon-exciton coupling as a direct result of nanorod fabrication.

This reduction in phonon replica intensity is related to a reduction in strain relaxation found when fabricating nanorods, and leads to a reduction in efficiency droop at high excitation power. This is evaluated by excitation power dependent PL measurements, and strongly supports the theoretical prediction proposed by Kioupakis et al. [21], that a reduction in phonon-exciton coupling can weaken the IAR mechanism and thus improve efficiency droop characteristics.

References

- ¹V. Ramesh, A. Kikuchi, K. Kishino, M. Funato, and Y. Kawakami, “Strain relaxation effect by nanotexturing InGaN/GaN multiple quantum well”, *Journal of Applied Physics* **107**, 114303 (2010).
- ²J. Bai, Q. Wang, and T. Wang, “Characterization of InGaN-based nanorod light emitting diodes with different In compositions”, *Journal of Applied Physics* **111**, 113103 (2012).
- ³H.-M. Kim, D. S. Kim, D. Y. Kim, T. W. Kang, Y.-H. Cho, and K. S. Chung, “Growth and characterization of single-crystal GaN nanorods by hydride vapor phase epitaxy”, *Applied Physics Letters* **81**, 2193 (2002).
- ⁴W. Bergbauer, M. Strassburg, C. Kölper, N. Linder, C. Roder, J. Lähnemann, A. Trampert, S. Fündling, S. F. Li, H.-H. Wehmann, and A. Waag, “Continuous-flux MOVPE growth of position-controlled N-face GaN nanorods and embedded InGaN quantum wells”, *Nanotechnology* **21**, 305201 (2010).
- ⁵S. Li and A. Waag, “GaN based nanorods for solid state lighting”, *Journal of Applied Physics* **111**, 071101 (2012).
- ⁶C. H. Chiu, T. C. Lu, H. W. Huang, C. F. Lai, C. C. Kao, J. T. Chu, C. C. Yu, H. C. Kuo, S. C. Wang, C. F. Lin, and T. H. Hsueh, “Fabrication of InGaN/GaN nanorod light-emitting diodes with self-assembled Ni metal islands”, *Nanotechnology* **18**, 445201 (2007).
- ⁷Q. Li, K. R. Westlake, M. H. Crawford, S. R. Lee, D. D. Koleske, J. J. Figiel, K. C. Cross, S. Fatholouloumi, Z. Mi, and G. T. Wang, “Optical performance of top-down fabricated InGaN/GaN nanorod light emitting diode arrays”, *Optics Express* **19**, 25528 (2011).
- ⁸D. Paramanik, A. Motayed, G. S. Aluri, S. Krylyuk, A. V. Davydov, M. King, S. McLaughlin, S. Gupta, H. Cramer, and B. Nikoobakht, “Optimization and shape control of GaN nanopillars fabricated by inductively coupled plasma etching”, in *Micro- and nanotechnology sensors, systems and applications iv*, Vol. 8373 (May 2012), page 8373.
- ⁹W. Rasband, *ImageJ*, Bethesda, Maryland, USA, 2012.
- ¹⁰L. Dai, B. Zhang, J. Y. Lin, and H. X. Jiang, “Comparison of optical transitions in InGaN quantum well structures and microdisks”, *Journal of Applied Physics* **89**, 4951 (2001).

- ¹¹H.-M. Kim, Y.-H. Cho, H. Lee, S. I. Kim, S. R. Ryu, D. Y. Kim, T. W. Kang, and K. S. Chung, “High-Brightness Light Emitting Diodes Using Dislocation-Free Indium Gallium Nitride/Gallium Nitride Multiquantum-Well Nanorod Arrays”, *Nano Letters* **4**, 1059–1062 (2004).
- ¹²T.-H. Hsueh, J.-K. Sheu, H.-W. Huang, Y.-H. Chang, M.-C. Ou-Yang, H.-C. Kuo, and S.-C. Wang, “Fabrication and Characterization of InGaN/GaN Multiple Quantum Wells Embedded in Nanorods”, *Japanese Journal of Applied Physics* **44**, 7723–7725 (2005).
- ¹³Q. Wang, J. Bai, Y. P. Gong, and T. Wang, “Influence of strain relaxation on the optical properties of InGaN/GaN multiple quantum well nanorods”, *Journal of Physics D: Applied Physics* **44**, 395102 (2011).
- ¹⁴T. Akasaka, H. Gotoh, H. Nakano, and T. Makimoto, “Blue-purplish InGaN quantum wells with shallow depth of exciton localization”, *Applied Physics Letters* **86**, 191902 (2005).
- ¹⁵D. M. Graham, P. Dawson, M. J. Godfrey, M. J. Kappers, P. M. F. J. Costa, M. E. Vickers, R. Datta, C. J. Humphreys, and E. J. Thrush, “High quantum efficiency InGaN/GaN structures emitting at 540 nm”, *Phys. Status Solidi (c)* **3**, 1970–1973 (2006).
- ¹⁶Y.-H. Cho, G. H. Gainer, A. J. Fischer, J. J. Song, S. Keller, U. K. Mishra, and S. P. DenBaars, “S-shaped temperature-dependent emission shift and carrier dynamics in InGaN/GaN multiple quantum wells”, *Applied Physics Letters* **73**, 1370 (1998).
- ¹⁷T. Wang, J. Bai, S. Sakai, and J. K. Ho, “Investigation of the emission mechanism in InGaN/GaN-based light-emitting diodes”, *Applied Physics Letters* **78**, 2617 (2001).
- ¹⁸B. Liu, R. Smith, J. Bai, Y. Gong, and T. Wang, “Great emission enhancement and excitonic recombination dynamics of InGaN/GaN nanorod structures”, *Applied Physics Letters* **103**, 101108 (2013).
- ¹⁹Y. Wu, C. Chiu, and C. Chang, “Size-dependent strain relaxation and optical characteristics of InGaN/GaN nanorod LEDs”, *Selected Topics in Quantum Electronics* **15**, 1226–1233 (2009).
- ²⁰R. Heitz, I. Mukhametzhanov, O. Stier, Madhukar, A, and D. Bimberg, “Enhanced Polar Exciton-LO-Phonon Interaction in Quantum Dots”, *Physical Review Letters* **83**, 4654–4657 (1999).
- ²¹E. Kioupakis, P. Rinke, A. Schleife, F. Bechstedt, and C. G. Van de Walle, “Free-carrier absorption in nitrides from first principles”, *Physical Review B* **81**, 2–5 (2010).

- ²²R. Martin, P. Edwards, R. Pecharroman-Gallego, C. Liu, C. Deatcher, I. Watson, and K. O'Donnell, "Light emission ranging from blue to red from a series of InGaN/GaN single quantum wells", *Journal of Physics D: Applied Physics* **35**, 604 (2002).
- ²³S. Kalliakos, X. B. Zhang, T. Taliercio, P. Lefebvre, B. Gil, N. Grandjean, B. Damilano, and J. Massies, "Large size dependence of exciton-longitudinal-optical-phonon coupling in nitride-based quantum wells and quantum boxes", *Applied Physics Letters* **80**, 428–430 (2002).
- ²⁴K. Huang and A. Rhys, "Theory of light absorption and non-radiative transitions in F-centres", *Proceedings of the Royal Society of London. Series A, Mathematical and Physical Sciences* **204**, 406–423 (1950).
- ²⁵D. Mowbray, O. Kowalski, M. Skolnick, M. Hopkinson, and J. David, "Optical spectroscopy of AlGaInP based wide band gap quantum wells", *Superlattices and Microstructures* **15**, 313 (1994).
- ²⁶S. Nakamura and S. Chichibu, *Introduction to Nitride Semiconductor Blue Lasers and Light Emitting Diodes* (Taylor & Francis, London and New York, 2000).
- ²⁷R. Pecharromán-Gallego, P. Edwards, R. Martin, and I. Watson, "Investigations of phonon sidebands in InGaN/GaN multi-quantum well luminescence", *Materials Science and Engineering B* **93**, 94–97 (2002).
- ²⁸Y. S. Park, M. J. Holmes, Y. Shon, I. T. Yoon, H. Im, and R. a. Taylor, "GaN nanorods grown on Si (111) substrates and exciton localization", *Nanoscale research letters* **6**, 81 (2011).
- ²⁹P. Renwick, H. Tang, J. Bai, and T. Wang, "Reduced longitudinal optical phonon-exciton interaction in InGaN/GaN nanorod structures", *Applied Physics Letters* **100**, 182105 (2012).
- ³⁰J. Piprek, "Efficiency droop in nitride-based light-emitting diodes", *Physica Status Solidi (A)* **207**, 2217–2225 (2010).
- ³¹J. Iveland, L. Martinelli, J. Peretti, J. S. Speck, and C. Weisbuch, "Direct Measurement of Auger Electrons Emitted from a Semiconductor Light-Emitting Diode under Electrical Injection: Identification of the Dominant Mechanism for Efficiency Droop", *Physical Review Letters* **110**, 177406 (2013).
- ³²E. Kioupakis, P. Rinke, K. T. Delaney, and C. G. Van de Walle, "Indirect Auger recombination as a cause of efficiency droop in nitride light-emitting diodes", *Applied Physics Letters* **98**, 161107 (2011).

- ³³Q. Dai, M. F. Schubert, M. H. Kim, J. K. Kim, E. F. Schubert, D. D. Koleske, M. H. Crawford, S. R. Lee, a. J. Fischer, G. Thaler, and M. A. Banas, “Internal quantum efficiency and nonradiative recombination coefficient of GaInN/GaN multiple quantum wells with different dislocation densities”, *Applied Physics Letters* **94**, 111109 (2009).

Study of the Enhancement of InGaN QWs by Surface Plasmon Coupling

Improving the emission properties of an InGaN QW by surface plasmon (SP) coupling is a potentially cost effective method of greatly improving the efficiency of an LED. The following chapter contains details of efficiency improvements of InGaN QW structures due to SP coupling.

5.1 Introduction to Exciton-Plasmon Interaction

As discussed in greater detail in the background chapter, section 2.7, an exciton in a semiconductor can couple to an oscillation of electrons in a metal, generating a plasmon. Plasmons localised in foils or grating structures are termed surface plasmons (SP) and are confined in one direction but may propagate along a film or surface. If a SP meets a scattering site, or is generated in a nanoparticle and is therefore confined in all dimensions, it becomes localised and is termed a localised surface plasmon (LSP) [1]. LSPs are plasmons restricted by the dimensions of nanoparticles or thin films to a specific energy range, instead of being allowed to move around a metal structure as with a plasmon or SP (which has the potential to establish a range of energy states but also lose energy via ohmic losses [2]). The shape and confinement in a nanoparticle or thin rough film may allow LSP resonance, creating a restoring force when the LSP is in the presence of an electromagnetic field, which allows field amplification in the particle and potentially in any surrounding dielectric. This process may give rise to an enhancement of the IQE of an InGaN QW, allowing a direct emission method via a SP which is faster than the normal radiative recombination lifetime [3].

In a spherical nanostructure of metal, when the dimensions approach the sub wavelength scale an SP energy level occurs due to confinement of the oscillating

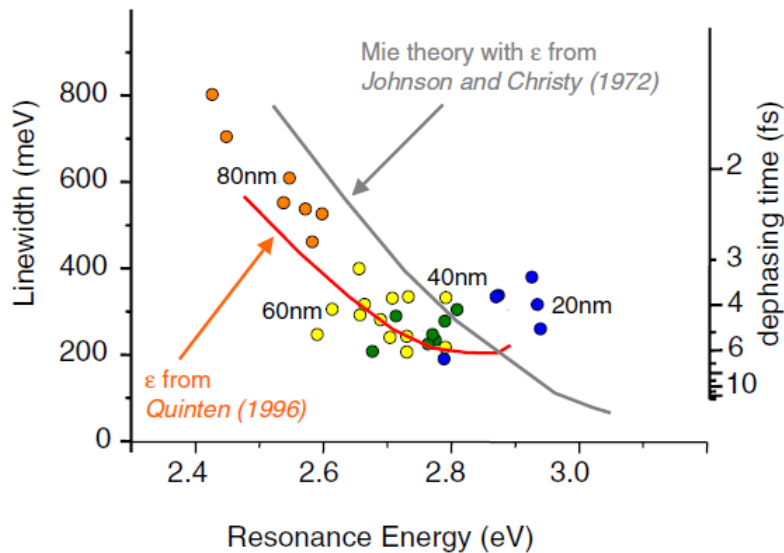


Figure 5.1: Diameter, line-width and cluster size of Ag nanoparticles measured experimentally as well as Mie theoretical calculations by Sönnichsen et al. from [4] (with permission).

electrons. An electromagnetic field such as a coupled electron and hole (exciton) in close proximity to the sphere induces a dipole moment of a specific magnitude (which can be calculated using the Frolich condition if no dielectric is in the vicinity of the particle [4].)

For any shape other than a perfect sphere, determining the SP energy is complex, and dielectric materials in the vicinity of the structure add to this complexity. Estimates can be made using Mie theory and the modelled dielectric constant of a metal, which match well with experimental results as performed by Sönnichsen et al., and shown in Figure 5.1 [4]. The resonance energy found in this study for Ag nano-clusters in the 20 - 80 nm diameter region correspond well with the bandgap energy of InGaN/GaN heterostructures operating in the blue and green wavelength region.

Providing a SP is confined as a LSP or meets a scattering site, it may allow the emission of a photon. If the plasmon is allowed to decay into a metal film however, the energy will be lost as heat, potentially causing a reduction in efficiency. Creating a suitable metal structure or grating that is optimised at a plasmon energy close enough to a QW bandgap energy (that creates LSPs and scattering sites) is therefore the key to enhancement via SP coupling.

Investigation of Plasmonic Enhancement of InGaN Quantum Wells

As discussed in chapter 2, plasmonic enhancement of GaN based structures has been investigated with Ag, Al, Au and Pt, [5–7] giving varying results with samples

based on the SP energy of the metal film, and bandgap energy of the semiconductor. Metals such as Ag, Au and Pt can have a broad range of SP energy based on the shape and size of the film or nanoparticle used. Ag, with energy in the 3.4 eV region is promising as this correlates well with GaN and InGaN structures with low In content, operating in the blue and green wavelength region. Au tends to have a SP energy around 2 eV, making it potentially useful for enhancement of very high In content InGaN structures, which may operate in the yellow to red wavelength ranges. The SP energy of Al and Pt tend to correspond to the UV optical wavelengths, with energy above 4 eV, although Pt in particular can support a widely varying SP energy depending on particle size [8].

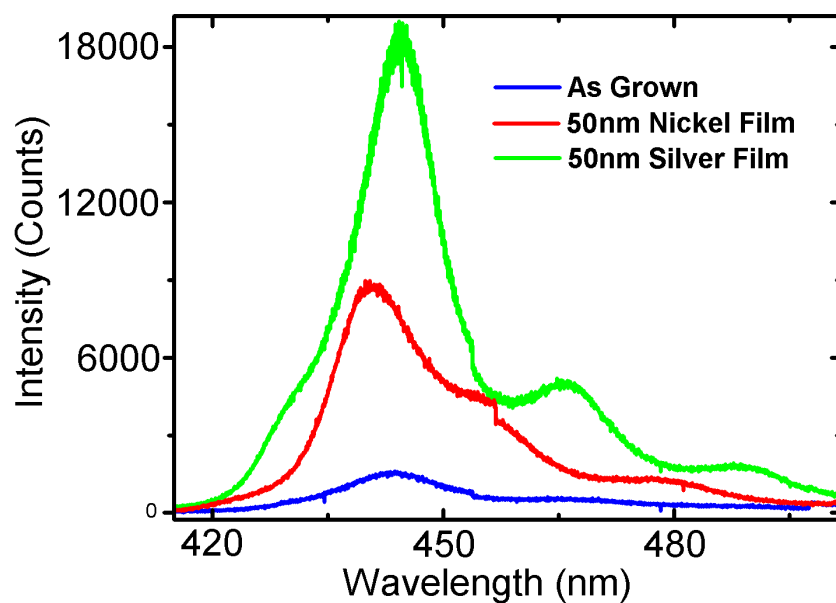


Figure 5.2: Enhancement of the PL emission of a planar InGaN single quantum well (SQW) sample by deposition of Ni and Ag films onto the surface of the structure, close to the InGaN active region. Peak enhancement of the sample with a Ni film is six times the planar as grown sample, with the Ag film producing twelve times enhancement.

Ni films tend to have a wide plasmon energy range in the 1 - 5 eV region, and may allow SP enhancement with some InGaN samples. An initial investigation of this yield increased performance of an InGaN QW, as can be seen in Figure 5.2, where enhancement in PL emission of a planar SQW structure is six times when a 50 nm Ni film is deposited onto the surface and PL measurements are taken through the back of the wafer. This is a significant enhancement, and there are currently no reported results of Ni SP enhanced InGaN structures in literature. A blue shift is also observed, which is more significant with the Ni film, suggesting the SP energy of the Ni is above that of the InGaN QW bandgap, and may be more suited to enhancement in the low UV spectrum. The enhancement found with Ag as seen in

| Metal | Thickness (nm) | Deposition Rate (nm/minute) | Coil Current (A) |
|-------|----------------|-----------------------------|------------------|
| Ag | 200 | 0.25 | 22 |
| Ag | 100 | 0.2 | 20 |
| Ag | 50 | 0.15 | 18 |
| Ag | 10 | 0.1 | 15 |
| Au | 120 | 0.2 | 15 |

Table 5.1: Sample preparation conditions - thickness and deposition rate of thermally evaporated metal films onto an InGaN SQW sample surface. The vacuum level for all depositions is below 2×10^{-6} mTorr.

Figure 5.2 is double that of the Ni film however, and consistently shows improved enhancement over other metals [9–13], so is therefore the main focus of this work.

5.2 Investigation of Ag Film Thickness on Surface Plasmon Enhancement of InGaN SQW Structures

An experiment has been devised to study the influence of increasing thickness Ag films on QW enhancement. Films in the nanometre thickness range allow SP modes with varying energy due to confinement in the deposition direction. This change in SP energy with thickness results in varying enhancement of the SQW emission, as the SP energy becomes close to the exciton energy allowing more efficient coupling.

5.2.1 Sample Fabrication

To investigate this, InGaN/GaN SQW samples were prepared into small rectangular tiles of similar size, approximately 5 x 5 mm, cleaved from the same central section of a wafer. The samples show good emission uniformity, and the SQW emits in the 440 nm wavelength region, with an as grown peak wavelength at 442.5 nm. The QW is a 2.5 nm $\text{In}_{13}\text{Ga}_{87}\text{N}$ well with thin GaN capping layer of ~ 7 nm, grown by MOCVD with a three layer laminar high speed gas flow allowing increase in sample quality by a reduction in thermal convection during growth [14]. The structure of the sample is shown in Figure 5.4.

Ag metal films of 10 nm - 200 nm thickness were thermally evaporated onto the tiles in separate deposition runs with an Edwards thermal evaporator, as detailed in Table 5.1. The thickness of the films is accurately monitored with a quartz crystal monitor, and a low deposition rate of between 0.1 and 0.25 nm/s is used for all films to ensure uniformity between the samples.

The evaporated Ag films on the sample surface become increasingly opaque with thickness. During testing laser excitation and sample emission must therefore be collected through the back side of the sample to ensure repeatability. The wafer initially has an unpolished back surface, which would cause scattering during PL testing. As a result, the sapphire substrate must be polished to a high level, which is accomplished using a Logitech PM5 precision lapping and polishing system.

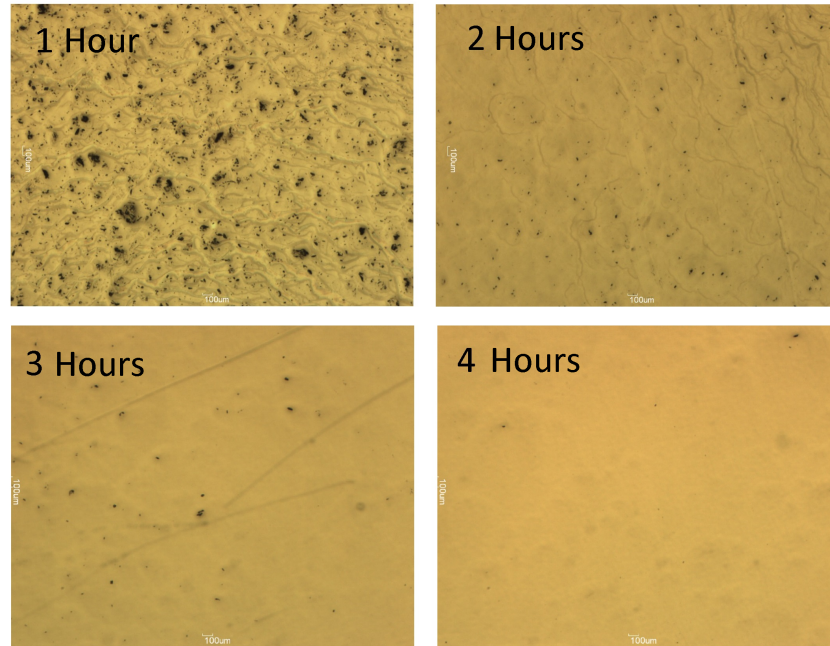


Figure 5.3: Optical microscope images of the back side of an InGaN/GaN SQW sample (showing the sapphire substrate) after polishing for between 1 and 4 hours.

An initial lapping process with accuracy of better than $1 \mu\text{m}$ flattens and thins the wafer, using a boron based lapping solution. The system is then used to polish to a high level using micro fibre pads and a nanoparticle sapphire polish solution, producing a smooth surface suitable for optical excitation and collection.

Figure 5.3 illustrates the results of the polishing process on the back side of an InGaN/GaN SQW sample, showing optical microscope images taken after polishing the back side of a sapphire substrate wafer between 1 and 4 hours - resulting in a very smooth surface ready for back side optical illumination without inducing excess light scattering.

5.2.2 Optical Characterisation of Surface Plasmon Enhanced InGaN SQWs

PL is obtained by laser excitation through the back of the sample with a 375 nm laser corresponding to a photon energy of 3.3 eV. This laser is chosen specifically as it selectively excites only the InGaN SQW, and is not absorbed by the bulk

GaN below it with slightly higher band-gap energy of ~ 3.4 eV. This allows direct probing of the QW structure, and laser excitation to pass through the underlying bulk GaN layers when measured from the back of the sample. The resulting InGaN SQW emission is also collected through the back of the sample, as illustrated in Figure 5.4.

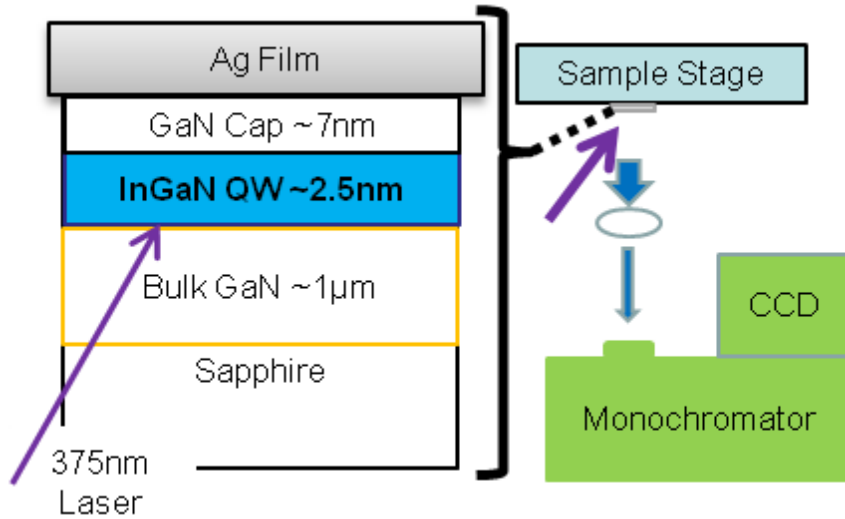


Figure 5.4: Diagram of an InGaN/GaN SQW structure with Ag film evaporated onto the surface, and a simplified schematic of the system used to obtain PL data.

5.2.3 PL Enhancement

As shown in the PL spectra on the left plot in Figure 5.5, a large enhancement of PL emission is observed with all Ag films of any thickness compared to a planar as grown sample. An increasing enhancement is observed with increasing film thickness, up to 100 nm of Ag, and above this width PL enhancement is reduced slightly.

To rule out enhancement due to reflectivity increases caused by the Ag film, an Au film of approximately 120 nm was deposited onto a sample. The Au metal has a low plasmon energy compared with the InGaN QW or GaN exciton energy, estimated to correspond to the ~ 560 nm wavelength range and above, which will not allow SP coupling to the QW emitting at 440 nm [3].

As can be seen in Figure 5.5, the Au film causes no enhancement due to reflections over the as grown sample, although the comparatively noisy spectra could be caused by some reflectivity in the structure, which does not appear to contribute to enhanced emission.

The reflectivity of Au is low compared to Ag, and some increase in the PL intensity is expected due to the high reflectivity of the Ag film. An increase in extraction of light is likely, due to the increased reflectivity of the sample surface reflecting more photon emission out of the rear of the sample to the collection

optics. Along with this increase, an increase in the reflection of the excitation laser is expected, which will effectively excite the InGaN SQW twice - once on the first pass, and once on the reflected pass of the laser. The intensity of the reflected excitation laser will be reduced, due to absorption by the SQW structure and Ag film, however combining this mechanisms along with reflected emission, a doubling of the PL output due to reflectivity alone is a reasonable estimation.

The use of Al as a plasmonic enhancement film was investigated by Okamoto et al., along with Au and Ag [3]. A similar result was observed, where strong enhancement is found with the Ag film, and no enhancement in PL with the Au film. The Al film does produce some enhancement, which could be caused by its higher reflectivity at the emission wavelength range of the sample, or due to a low plasmonic enhancement effect.

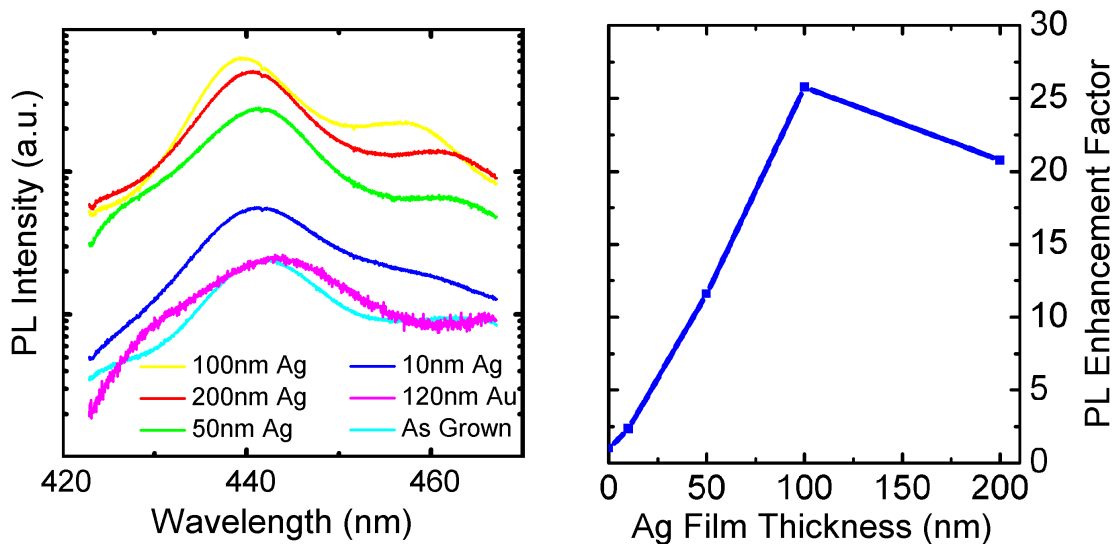


Figure 5.5: Increase of PL intensity and blue shift of peak energy of an InGaN SQW with increasing Ag film thickness.

The increase in PL peak intensity is plot on the right graph in Figure 5.5, where a clear trend is apparent. A significant enhancement of over twenty five times is found for a 100 nm Ag film, suggesting dramatic improvements to the radiative emission of the SQW, although some enhancement due to reflectivity of the Ag film is expected.

The initial increase in enhancement up to the peak with a 100 nm film is caused by the change in SP energy in the films due to confinement. With a 10 nm film, the confinement of the SPs in the structure will result in a low wavelength (high energy) SP mode, well below the peak wavelength of the InGaN SQW. As thickness is increased to a 50 nm film, the enhancement increases rapidly. This corresponds to a change in the SP energy due to the increase in thickness and therefore change in confinement in the film.

Above 100 nm, a slight reduction in enhancement is observed. This is due to two mechanisms:

The first is a change in SP mode energy as the confinement in the film changes, moving the SP energy below that of the InGaN SQW exciton energy and reducing the number of carriers coupling into SP modes.

The second is the change in grain structure and morphology of the thicker 200 nm Ag film. As the film thickness is increased, the film becomes smoother with a build up of metal, resulting in a reduction in scattering sites to localise LSP modes and confinement. This will result in increased ohmic loss in the film, as the InGaN SQW excitons transfer into SP modes, which then dissipate in the metal film before meeting a scattering site.

5.2.4 Peak Wavelength Blue Shift

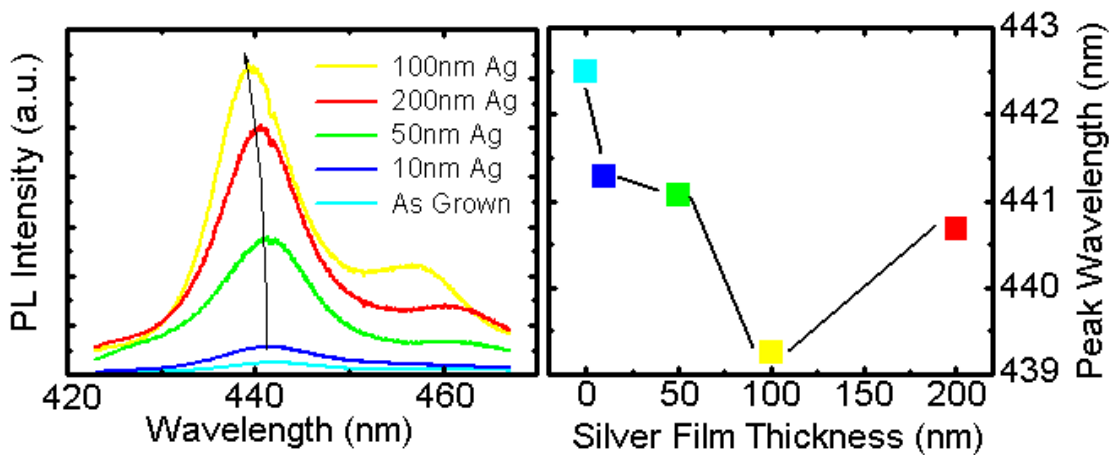


Figure 5.6: Blue shift in peak emission energy caused by surface plasmon interaction between an InGaN/GaN SQW sample and varying thickness Ag films.

A peak energy shift to the blue end of the spectrum is observed with all Ag coated samples, and as with the peak enhancement, is at a maximum for a 100 nm Ag film. This is illustrated in Figure 5.6, showing PL spectra with an arrow highlighting the peak shift on the left plot. The peak wavelength against Ag film thickness on the right plot shows accurate peak position and the change with increasing Ag film thickness.

This result is explained by a change in the recombining exciton energy of the QW structure due to the very fast SP coupling mechanism.

As previously discussed, the excitons from the InGaN SQW couple quickly to SP modes resulting in a fast emission process. This transition occurs before the excited carriers in the QW have had time to fully relax to the band edge of the structure.

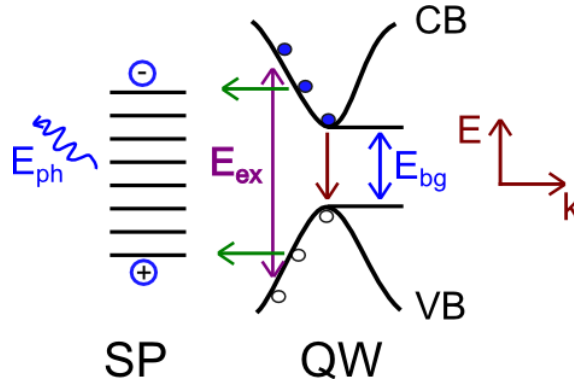


Figure 5.7: Coupling between a QW and Ag film with SP modes.

This is illustrated in Figure 5.7. As discussed in chapter 2, with a PL measurement system or in an LED, the injected carriers have high energy as they enter the system, and relax to the QW edge by a series of small energy reductions. Because the effective radiative lifetime is reduced due to SP coupling, carriers can potentially transfer to an SP mode before reaching the band edge of the structure [9, 10]. As such, the emission is blue shifted, as carriers have slightly higher energy when emitting before reaching the band edge. This mechanism depends on the carrier relaxation time in an InGaN QW structure, suggested to be below 150 ps in a study by Ushiyama et al. [15]. The coupling to SP modes would need to be faster than this process to support this mechanism, and studies by Okamoto et al. have found emission lifetimes for SQW InGaN structures enhanced by SP modes to be approximately 200 ps [16]. As the lifetimes are of the same order, this mechanism can be considered.

A second mechanism for the blue shift could be related to some form of relaxation of the QCSE as discovered in the previous nanostructure chapter. In this system, a plasmon (or oscillation of electrons with associated electric field) in close proximity to the InGaN QW could influence the strain in the well by opposing the electric field caused by strain. The result would be a blue shift in emission energy, related to the amount of carriers coupling into plasmon modes, and hence plasmon enhancement. A related mechanism could be the number of carriers present in the QW, which is known to reduce the QCSE [17].

As the energy of Ag films below 100 nm in thickness is high, the majority of excited carriers will be below the energy of the SP modes. Some blue shift (and peak enhancement) is observed with these films however, suggesting some Ag grains in the film will allow SP modes of the correct energy to allow excitons in the QW to couple their energy. As a result the blue shift in peak energy is observed to increase as SP mode energy becomes close to the InGaN exciton energy.

As with PL enhancement, the maximum blue shift of almost 3.5 nm is observed

for a 100 nm Ag film, suggesting the SP modes have optimal energy to allow coupling between InGaN SQW excitons in this confinement regime.

Above the optimum Ag film thickness, a decrease in peak blue shift is observed (with the 200 nm thick Ag film). This is again due to two mechanisms.

The first is a result of a reduced SP energy due to the change in confinement in the film. This suggests some excitons will couple to SP modes, however they will be at lower energy (longer wavelength) than with a 100 nm Ag film.

The second mechanism again relates to losses in the 200 nm Ag film due to the morphology change. Excitons coupling to higher energy SP modes will have a greater chance of being ohmically lost in the thick Ag film as the oscillation mode is smaller and more likely to dissipate as a bulk plasmon. This suggests that higher energy excitons coupling into SP modes are more likely to non-radiatively recombine as Ag film thickness increases beyond the optimum.

5.3 Investigation of Ag Grain Size Dependence on Surface Plasmon Enhancement

It is theorised that the Ag films deposited onto the samples have specific SP energy due to confinement in the metal grains in the film structure. As thickness and grain size change, the energy of the SP begins to match to the InGaN QW exciton energy, with a peak and best match with a 100 nm film and deposition rate of 0.2 nm/s used in the previous section to produce optimum enhancement.

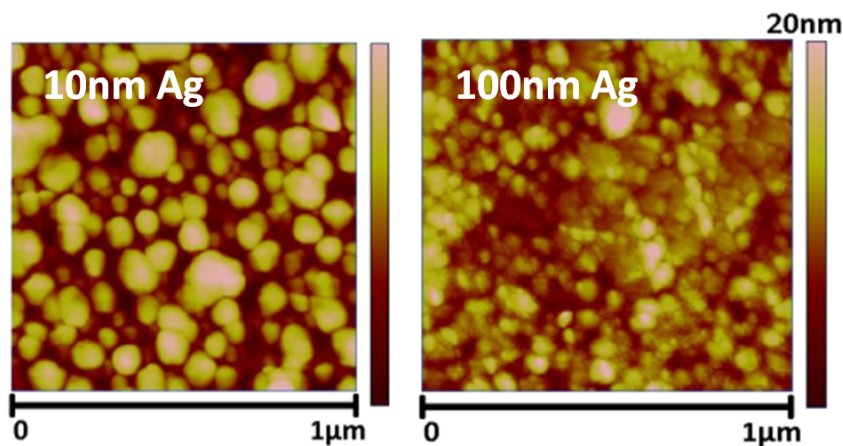


Figure 5.8: 10 nm and 100 nm Ag films on InGaN/GaN QW surface by AFM.

To further investigate this, high resolution AFM images were taken of the Ag films deposited by thermal evaporation on InGaN/GaN SQW structures.

Figure 5.8 shows AFM images of the Ag surface, where it is clear that a change in morphology occurs with changing film thickness.

| Metal | Thickness (nm) | Deposition Rate (nm/minute) | Coil Current (A) |
|-------|----------------|-----------------------------|------------------|
| Ag | 50 | 2 | 30 |
| Ag | 50 | 0.1 | 15 |

Table 5.2: Sample preparation conditions for two 50 nm Ag films with very different deposition rates. The vacuum used for both depositions is consistent, below 6×10^{-6} mTorr.

The 10 nm film appears as a series of Ag nano-islands on the sample surface, which are metal grains of Ag deposited at random across the wafer with varying size. This produces highly localised SPs with a large energy due to the confinement in the grains, resulting in a poor match in energy to the QW excitons and therefore reduced PL enhancement as observed in Figure 5.5.

The 100 nm film has coalesced into a smoother surface, where the grains have built into a film. The PL data in the previous section suggests the 100 nm Ag film has optimal SP energy for coupling to a blue wavelength InGaN QW and hence maximum PL enhancement. This is due to the morphology of the film, which has the optimum combination of size and grain structure to allow confinement of the surface plasmons at the correct energy. The film like structure will allow some propagation of SPs, but still confine them as LSPs and provide scattering sites allowing radiative emission to occur. This provides a large DOS for excitons to couple into SP modes confined in the film, and recombine efficiently via radiative processes.

Deposition Rate

Controlling the deposition rate of an Ag film is important, as this changes the morphology of the film and hence alters the SP confinement energy. To investigate the effects of deposition rate, two InGaN/GaN SQW samples were prepared, details of which are presented in Table 5.2.

50 nm of Ag was deposited onto one sample's surface using a very fast deposition rate of approximately 2 nm/s, and 50 nm of Ag was deposited onto the other with a very slow deposition rate of approximately 0.1 nm/s. Deposition rates and film thickness were obtained using a quartz crystal monitor fitted to a thermal evaporator with an accuracy of ± 0.1 nm.

AFM measurements were taken of the Ag films after deposition, and PL measurements were carried out at room temperature, comparing both samples with different deposition rates against an as grown sample from the same wafer. Figure 5.9 shows AFM scans of the samples surfaces after Ag deposition.

Figure 5.10 shows PL spectra of three samples on a log-linear scale; an as grown sample, and the two 50 nm Ag film samples with different deposition rates. It is

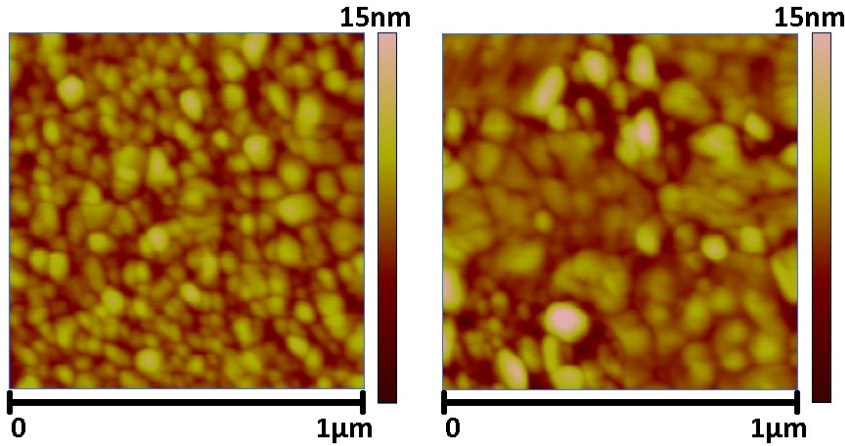


Figure 5.9: 50 nm Ag films on an InGaN SQW sample, deposited with slow (left image) and fast (right image) deposition rates. A clear change in morphology is observed between the two samples.

clear from Figure 5.9 that the morphology of the Ag films is very different, resulting in a change in SP energy and confinement for each sample even though the thickness is identical.

The low deposition rate sample, which appears to consist of smaller Ag particles or grains, and has a rougher surface, has a SP energy that is closer to the InGaN QW, and has a larger number of scattering sites due to the increased surface roughness. This allows the sample to have a higher PL intensity than the sample with Ag film deposited at a fast rate, where the SPs have lower energy due to the large grains deposited, and meet fewer scattering sites to allow momentum change and photon emission, resulting in greater carrier loss via dissipated SP modes [18].

This explanation has recently been confirmed by Xu et al. [19], where the dependence of SP energy to Ag grain size was further examined by sputtering Ag films, allowing accurate control of the grains and morphology of the Ag film. An ideal grain size of approximately 50 nm was observed in their study to couple to a high energy blue InGaN QW, corresponding well to the data presented here.

5.4 Study of Internal Quantum Efficiency of an InGaN SQW Enhanced by Surface Plasmon Coupling

Internal quantum efficiency estimations based on temperature dependant PL were undertaken to ascertain the IQE enhancement found in the structure. Previous standard PL measurements found up to twenty five times enhancement of an InGaN SQW sample due to a 100nm thick Ag film. Some of this enhancement may be

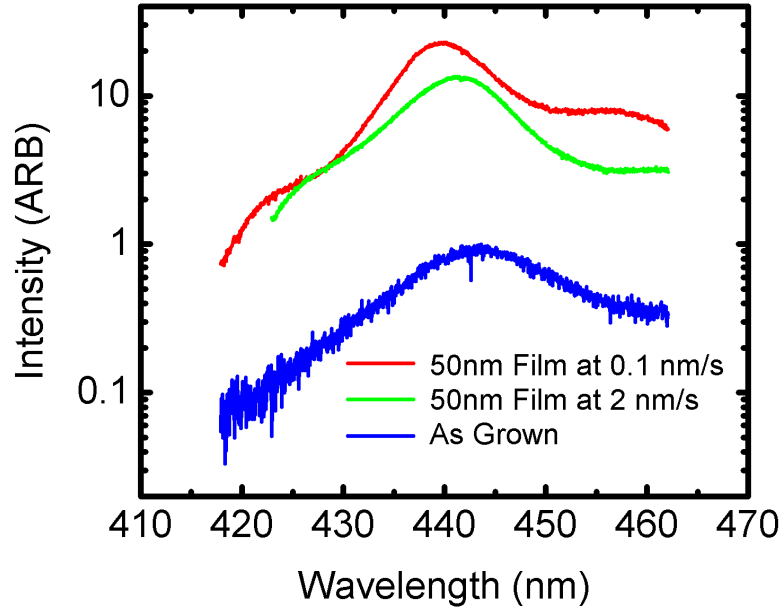


Figure 5.10: PL scan taken at room temperature showing the spectra of three samples: The lower spectra is the as grown sample, and the two enhanced spectra are from InGaN SQW samples coated with 50 nm Ag films. These samples differ due to their Ag deposition rate, which explains the difference in PL spectra.

due to laser or emission reflections caused by the Ag film, and therefore the IQE measurement of a sample provides the enhancement of the SQW structure only.

The real radiative efficiency increase is obtained by first cooling the sample to a temperature of 10K. At this temperature range, non-radiative recombination via defects is very low due to carrier localisation and a reduction in thermal effects, therefore the efficiency of the structure can be assumed to be 100%. By taking PL spectra at this range, and at regular intervals as temperature is increased, a change in efficiency can be observed as non-radiative effects begin to influence the recombination mechanisms. Using an Arrhenius plot, the efficiency can be obtained at 300K or approximately room temperature, where devices would operate. It is important to point out that the active region of the structure will be at a higher temperature of over $\sim 350\text{K}$ for a power LED, however the ambient temperature of operation is likely to be room temperature. The excitation laser used in this experiment will induce localised heating of the active region, which quickly dissipates into the surrounding GaN material and accurately mimics the operation conditions of an LED [20].

Figure 5.11 illustrates the efficiency increase observed. A significant enhancement in IQE of ten times due to excitons coupling to SP modes in a 100 nm Ag film on an InGaN SQW sample. The increase over the as grown sample is due to carriers

radiatively recombining quickly via SP modes, resulting in greater photon emission from the structure and reduced non-radiative recombination.

The enhancement in IQE of approximately seven times found with a 50 nm Ag film on the InGaN sample is also shown in Figure 5.11. This shows that efficiency is still increased considerably, however due to the greater confinement found in this film, the SP modes present are likely to be of higher energy than the excitons in the SQW, reducing the DOS available in the film at the InGaN exciton energy and hence reducing the coupling rate.

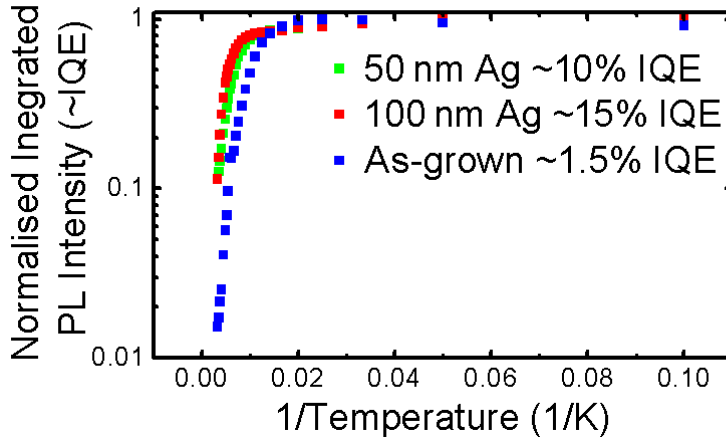


Figure 5.11: Arrhenius plot of the temperature dependant PL of an as grown InGaN QW and Ag Coated QW allowing an estimation of IQE.

5.5 Study of Surface Plasmon Enhanced InGaN QW Exciton Dynamics

As mentioned, a QW can potentially transfer an exciton to a SP in a silver film, which is made up of varying size grains of silver. The generated SP has the energy of the exciton from the QW, and propagates through the silver film until it dissipates as heat (ohmic loss) or meets a scattering site and becomes localised as a LSP. If the SP meets a scattering site, a change in momentum of the SP causes a photon emission as the plasmon scatters, emitting at the same energy as the exciton that it coupled with.

The coupling and resultant transfer of energy from exciton to SP is a fast process, generally below 1ns [11, 21]. This is faster than the normal radiative or non-radiative recombination processes in a QW structure, and potentially allows a high number of carriers to couple into SP modes. If a QW-Ag structure is correctly designed, the excitons that quickly transfer into SP modes can then meet a scattering site and

emit as a photon, potentially improving the overall emission efficiency of the system [13].

This process can be demonstrated with time resolved photoluminescence, where the decay time of a QW structure in close proximity to an Ag film is faster than the same QW without the influence of SP modes in a film [3].

An InGaN/GaN 10QW structure was prepared with 100 nm of Ag deposited onto the surface at a standard deposition rate of approximately 0.2 nm/s.

Due to limitations with the TRPL system, a strongly emitting 10QW structure allows a time decay trace to be observed, however the excitation laser power and detector sensitivity are too low to accurately measure the emission from a single or 2QW sample. This limitation arises due to the need to measure through the back of the sample, requiring a specific laser with very fast pulse response and wavelength above the GaN band edge yet below the InGaN band edge. The 375 nm laser used here has a high individual pulse energy, but an average emission power of below 0.1 mW, meaning time decay data from a SQW structure is very difficult to observe.

The time decay at room temperature for an InGaN QW structure is very fast as non-radiative recombination tends to be the dominant mechanism. As such, measurements of time decay are performed at low temperature here, allowing accurate comparisons between samples due to the long decay comprising mostly of radiative processes.

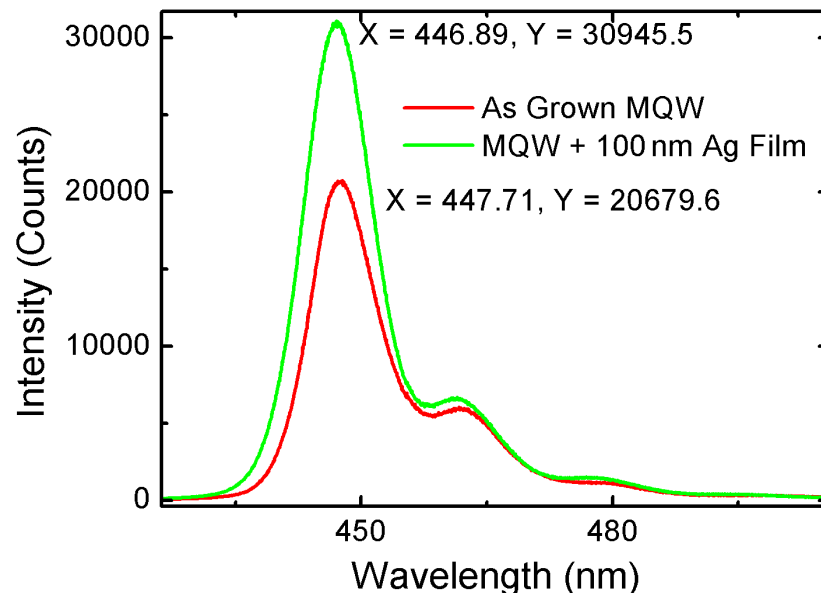


Figure 5.12: PL measured with a standard CCD at a temperature of 7K of a normal MQW heterostructure and MQW in close proximity to an Ag film. A clear PL increase and blue shift are observed, evidence of SP coupling.

The PL emission collected using a conventional CCD detector of the planar

MQW and SP enhanced MQW structures is shown in Figure 5.12, where a clear PL increase of approximately 50% is observed, along with a blue shift in peak wavelength of approximately 1 nm. As both samples are measured at a low temperature and assumed to be 100% efficient, any enhancement in emission is likely due to the reflectivity of the Ag film instead of due to SP coupling. The difference between the samples is therefore the recombination mechanism, via excitons in the as grown sample and via a SP mode with the sample in close proximity to an Ag film, both of which are efficient at this temperature.

Illustrated in Figure 5.13 are the decay time traces for the SP enhanced InGaN MQW structure and a planar InGaN MQW sample measured at 7K. The time decay is measured with a fast PMT-like detector to be 4.7 ns at a temperature of 7K for an InGaN MQW structure coupled to SP modes, compared to a decay time of 6.7 ns for an identical as grown planar sample at 7K without SP coupling. This significant change in decay time is a direct result of the fast coupling of excitons into SP modes, resulting in more efficient radiative recombination.

It is important to point out that the fringing depth of an Ag SP in close proximity to GaN is approximately 47 nm. The structure of the InGaN MQW stack is 2.5 nm InGaN QWs with 7 nm GaN barriers. This means SP coupling will only occur in the top 4 or 5 QWs, while the lower QWs are unaffected by SP coupling as they are outside the fringing field. As a result, the time decay measured is a combination of conventional and SP enhanced QW emission, suggesting the real decay time of the SP coupled QWs is significantly faster.

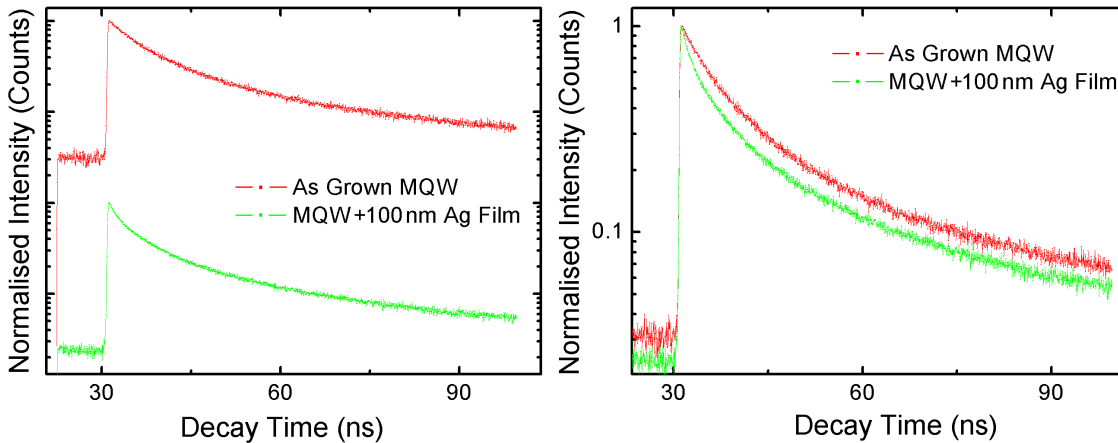


Figure 5.13: Time resolved PL decay curves of a normal QW and QW in close proximity to an Ag film, showing a decrease in decay time caused by the Ag film, corresponding to carriers coupling to SP modes. The graph on the left is a normalised plot showing stacked decay traces. The right hand graph shows overlaid traces, where the difference in decay profile is apparent.

The decay times and data fitting parameters of the traces in Figure 5.13 are

| Coefficient (ns) | As Grown InGaN MQW | MQW + 50 nm Ag Film |
|------------------|--------------------|---------------------|
| τ_1 | 6.694 | 4.700 |
| τ_2 | 33.48 | 29.656 |

Table 5.3: Time decays for an InGaN MQW sample and a sample with a 50 nm Ag film in close proximity to the active region.

shown in Table 5.3, where a bi-exponential function produces an accurate fit to the decay traces. The carrier decay times for both exponential functions are lower for the sample enhanced by SP coupling, suggesting an increase in the radiative decay rate due to carrier transfer to plasmon modes.

The radiative decay time constant for spontaneous emission is related to the DOS in the system, as described by Fermi's golden rule. Increasing the DOS can lead to increased photon emission, as the transition probability is increased due to more states being available - originally described by Purcell et al. [22]. From this, the Purcell factor F_P describes the ratio of enhanced emission due to an increase in the available DOS, and the normal free space emission of a system. As such, an exciton-SP coupled system can be described by F_P , where the SP modes influence an emitting dipole (an exciton in an InGaN QW here) by providing a higher DOS. At the energy range of interest, for InGaN visible emission in the blue-green wavelength range, the SP energy of Ag has a very high SP DOS as the SP dispersion relation nears its asymptotic limit. Due to this, a very high F_P can be generated in an InGaN QW-SP coupled system, as a result of an increased number of states available due to SP modes, resulting in a much faster time decay and hence more efficient recombination [11].

5.6 Conclusions

The PL enhancement of an InGaN SQW as a function of Ag film thickness has been investigated, where a changing Ag film thickness was found to modify the SP energy in the film. This results in varying enhancement with film thickness, and a maximum enhancement of over twenty five times in PL intensity is found for a sample with a 100 nm thick Ag film.

A blue shift in PL peak energy is observed, linked to the Ag film thickness and therefore a change in SP energy. This is caused by a change in the morphology of the film as a result of varying grain size, and is related to thickness and deposition rate. An investigation into deposition rates confirms the change in enhancement and blue shift of the InGaN SQW emission, which is further backed up by a recent publication on Ag grain dependence of SP energy by Xu et al. [19].

The IQE increase due to SP coupling is measured by temperature dependant PL methods, showing an increase in efficiency of approximately ten times in IQE between an as grown sample and sample with 100 nm Ag film in close proximity to the QW, suggesting massive real world enhancements are obtained when coupling excitons in an InGaN QW to SP modes in Ag films.

The radiative enhancement of InGaN based structures due to SP coupling are investigated with detailed optical characterisation. The mechanism of enhancement is researched, where a change in time decay of a MQW sample enhanced by SP coupling is observed, linked to increased DOS and radiative recombination via SP modes.

References

- ¹A. V. Akimov, A. Mukherjee, C. L. Yu, D. E. Chang, A. S. Zibrov, P. R. Hemmer, H. Park, and M. D. Lukin, “Generation of single optical plasmons in metallic nanowires coupled to quantum dots”, *Nature* **450**, 402–6 (2007).
- ²S. A. Maier, *Plasmonics: Fundamentals and Applications* (Springer Science and Business Media, LLC, 2007).
- ³K. Okamoto, I. Niki, A. Shvartser, Y. Narukawa, T. Mukai, and A. Scherer, “Surface-plasmon-enhanced light emitters based on InGaN quantum wells”, *Nature Materials* **3**, 601–605 (2004).
- ⁴C. Sonnichsen and T. Franzl, “Plasmon resonances in large noble-metal clusters”, *New Journal of Physics* **4**, 93 (2002).
- ⁵T. S. Oh, H. Jeong, Y. S. Lee, J. D. Kim, T. H. Seo, H. Kim, A. H. Park, K. J. Lee, and E.-K. Suh, “Coupling of InGaN/GaN multiquantum-wells photoluminescence to surface plasmons in platinum nanocluster”, *Applied Physics Letters* **95**, 111112 (2009).
- ⁶K. Okamoto, A. Scherer, and Y. Kawakami, “Enhanced Light Emission by Exciton Surface Plasmon Coupling”, *Materials Research* **1055**, 8–12 (2008).
- ⁷I. Gontijo, M. Boroditsky, E. Yablonovitch, S. Keller, U. Mishra, and S. DenBaars, “Coupling of InGaN quantum-well photoluminescence to silver surface plasmons”, *Physical Review B* **60**, 11564 (1999).
- ⁸A. D. Rakic, A. B. Djurisic, J. M. Elazar, and M. L. Majewski, “Optical properties of metallic films for vertical-cavity optoelectronic devices.”, *Applied Optics* **37**, 5271–83 (1998).
- ⁹D.-M. Yeh, C.-F. Huang, C.-Y. Chen, Y.-C. Lu, and C. C. Yang, “Surface plasmon coupling effect in an InGaN/GaN single-quantum-well light-emitting diode”, *Applied Physics Letters* **91**, 171103 (2007).
- ¹⁰J. J. Mock, M. Barbic, D. R. Smith, D. A. Schultz, and S. Schultz, “Shape effects in plasmon resonance of individual colloidal silver nanoparticles”, *The Journal of Chemical Physics* **116**, 6755 (2002).
- ¹¹A. Neogi, C.-W. W. C. Lee, H. O. H. Everitt, T. Kuroda, A. Tackeuchi, and E. Yablonovitch, “Enhancement of spontaneous recombination rate in a quantum well by resonant surface plasmon coupling”, *Physical Review B* **66**, 1–4 (2002).
- ¹²Y.-C. Lu, C.-Y. Chen, K.-C. Shen, D.-M. Yeh, T.-Y. Tang, and C. C. Yang, “Enhanced photoluminescence excitation in surface plasmon coupling with an InGaN/GaN quantum well”, *Applied Physics Letters* **91**, 183107 (2007).

- ¹³K. Okamoto, I. Niki, A. Scherer, Y. Narukawa, T. Mukai, and Y. Kawakami, “Surface plasmon enhanced spontaneous emission rate of InGaN/GaN quantum wells probed by time-resolved photoluminescence spectroscopy”, *Applied Physics Letters* **87**, 071102 (2005).
- ¹⁴T. Wang, D. Nakagawa, J. Wang, T. Sugahara, and S. Sakai, “Photoluminescence investigation of InGaN/GaN single quantum well and multiple quantum wells”, *Applied Physics Letters* **73**, 3571 (1998).
- ¹⁵T. Ushiyama, T. Toizumi, Y. Nakazato, and A. Tackeuchi, “Energy relaxation time of hot carriers photoexcited in InGaN”, *Physica Status Solidi (C)* **5**, 143–145 (2008).
- ¹⁶K. Okamoto and Y. Kawakami, “High-Efficiency InGaN/GaN Light Emitters Based on Nanophotonics and Plasmonics”, *IEEE Journal of Selected Topics in Quantum Electronics* **15**, 1199–1209 (2009).
- ¹⁷S. Nakamura and S. Chichibu, *Introduction to Nitride Semiconductor Blue Lasers and Light Emitting Diodes* (Taylor & Francis, London and New York, 2000).
- ¹⁸P. Renwick, H. Tang, Q. Wang, R. Smith, and T. Wang, “Enhanced internal quantum efficiency of an InGaN/GaN quantum well as a function of silver thickness due to surface plasmon coupling”, *Physica Status Solidi (c)* **8**, 2176–2178 (2011).
- ¹⁹X. Xu, M. Funato, Y. Kawakami, K. Okamoto, and K. Tamada, “Grain size dependence of surface plasmon enhanced photoluminescence”, *Optics Express* **21**, 3145–51 (2013).
- ²⁰V. Ramesh, A. Kikuchi, K. Kishino, M. Funato, and Y. Kawakami, “Strain relaxation effect by nanotexturing InGaN/GaN multiple quantum well”, *Journal of Applied Physics* **107**, 114303 (2010).
- ²¹C.-Y. Chen, D.-M. Yeh, Y.-C. Lu, and C. C. Yang, “Dependence of resonant coupling between surface plasmons and an InGaN quantum well on metallic structure”, *Applied Physics Letters* **89**, 203113 (2006).
- ²²E. Purcell, H. Torrey, and R. Pound, “Resonance absorption by nuclear magnetic moments in a solid”, *Physical Review* **69**, 37–38 (1946).

Stimulated Emission from Single Nanorods Enhanced by Surface Plasmon Coupling

6.1 Single Nanorod Emitters

Micro or nano-emitters are a useful tool with many varied applications. Highly accurate photolithographic techniques can be developed using blue or UV wavelength range nano-emitters, which would allow patterning at beyond the diffraction limit currently observed with normal lithographic techniques. Nano-emitters can also be combined with scanning near-field optical microscopy (SNOM) systems to allow sub wavelength microscopy and lithography [1]. Nano-lasers in particular have a future use in system-on-chip optical communications and computing, where emitters with a direct bandgap and narrow linewidth can be combined with mature Si technology to communicate optically as interconnects and optical switches [2]. The main issue currently surrounding the miniaturisation of lasers and other emitters is the diffraction limit of the optical cavity, and using NRs could be the way to push past this limit [3].

A potential method to increase the performance of InGaN nano-emitters is to couple them with surface plasmons, to increase the efficiency of the structure and develop stimulated emission from nanorods. Infra-red [4] and red [5] wavelength plasmonic lasers have been developed, and stimulated emission from plasmonically coupled CdS [3] and InGaN core-shell [6] MBE grown nanorods has been observed at some wavelengths. A simple method of fabricating such devices from conventional GaN growth methods would allow cost effective lasers to be developed, and this is investigated in the following chapter.

6.2 Single Nanorod Fabrication Techniques

As single NRs are difficult to identify and characterise due to their size (requiring electron microscopy techniques to measure size and shape), a uniform size of NRs is desirable. This allows comparisons to be made between samples, under the knowledge that the individual NRs measured are of the same dimensions (depending on mask and etch uniformity). Initial investigation of single NRs therefore requires the development of an array of uniform emitters, instead of the varying size NR array fabricated using a self aligned Ni mask as discussed in chapter 4. This can be accomplished using a SiO₂ nanosphere mask.

6.2.1 Silicon Dioxide Nanosphere Mask

Nanorods can be created using SiO₂ nanospheres as a mask. These spheres can be drop cast or spun onto a sample, allowing a uniform mask to be formed on the surface without the use of high temperature annealing or metal deposition. Etching using similar parameters to the Ni self aligned mask process in chapter 4 produces nanorods which are more uniform in diameter than a self aligned process. The uniformity depends on the range of SiO₂ sphere diameters prepared in solution, which can be improved with a centrifuge process allowing the separation of nanospheres into layers in a solution depending on size. Typically nanospheres approximately 500 nm in diameter are used in this work.

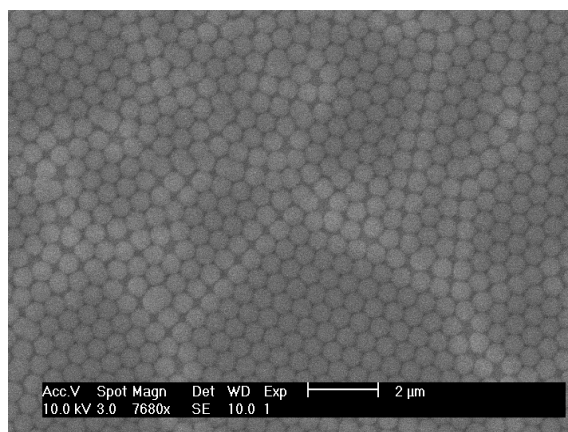


Figure 6.1: SEM image of SiO₂ nanospheres with a diameter of approximately 500 nm used as an etch mask to produce nanorods with uniform diameter.

A monolayer of nanospheres must be created to produce a good mask, which is best achieved by spinning. To spin the spheres, a sample is mounted to a spinner vacuum chuck, and a solution of nanospheres (suspended in de-ionised water or solvent) that have recently been subject to an ultrasonic bath (to uniformly mix them) is applied. A micro-litre scale pipette is used to drop a small amount of

nanosphere solution onto a sample - typically, $6 \mu\text{l}$ of solution for a 5 mm^2 sample. The spheres are allowed to settle for several minutes, followed by a spin program consisting of a slow ramp in spin speed followed by spin at 2000 RPM, allowing a monolayer of spheres to form on some areas of a sample.

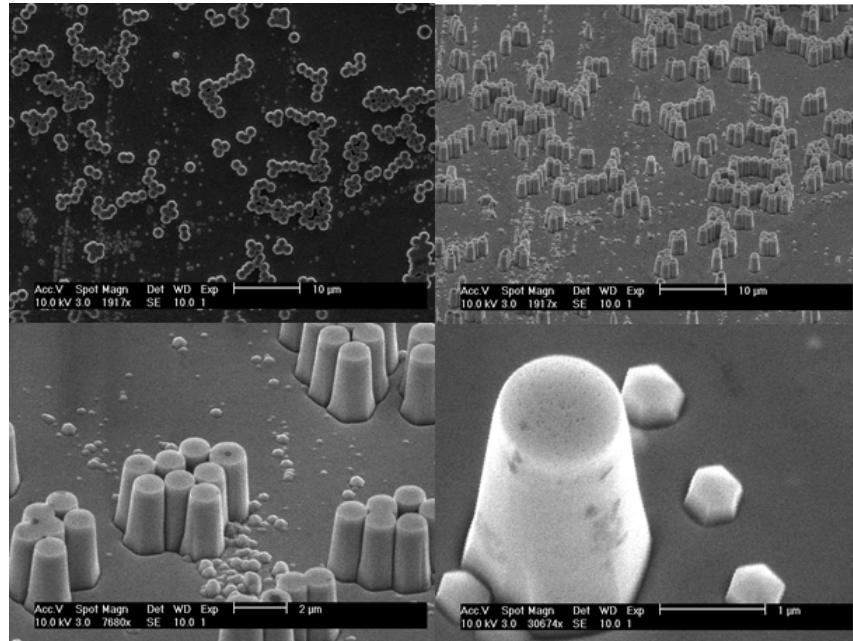


Figure 6.2: Various SEM images of nanorods etched using a drop cast nanosphere mask. The SiO_2 nanospheres used here are the largest used in this work, at approximately $1 \mu\text{m}$ in diameter.

A problem encountered with using a SiO_2 nanosphere mask is the maximum reproducible sample size that can be processed. A self aligned Ni mask will work with good uniformity across a wafer larger than 2", however a uniform SiO_2 nanosphere mask on this scale is difficult to produce by spin coating. Typically a uniform monolayer can be produced across most of a small wafer fragment after optimisation, although a maximum uniform area of several millimetres in diameter appears to be the limit. Edge effects encountered during the dropping and spinning process also mean uniformity is poor around the sample edge, with typically approximately 2 mm from the edge consisting of multi layered nanospheres that are unsuitable as an etch mask. Surfactants such as sodium dodecyl sulphate (SDS) must be used to obtain this degree of uniformity, and many defects still occur in the arrangement of the spheres. As an example, an ordered array of nanospheres can be seen in the SEM image in Figure 6.1, where although a lattice is produced, defects in the structure are seen, caused by non uniformity in the sizing of some spheres.

The spheres are well adhered to a sample surface by stiction and van der Waals interaction [7]. This electrostatic friction encountered by the nm scale nanospheres allows processing such as dry etching to occur without disturbing the array. Spheres

can be removed with a vigorous ultrasonic treatment in solution, or by wet etching in a HF acid solution which acts to dissolve the SiO₂ spheres.

In a drop cast method, a dilute nanosphere in solvent solution is produced, where typically the solution used to spin coat is diluted at a ratio of 10:1 solvent to nanosphere solution. A low quantity of solution is used, typically for a 5 mm² sample, 3 μ l is applied using a micro-litre pipette. The solvent is allowed to evaporate from the sample, leaving behind single or small arrays of nanospheres. The density of nanospheres is low, with large gaps between spheres, as can be seen in the SEM images of nanorods prepared using this process in Figure 6.2 (using 1 μ m nanospheres to ease initial characterisation).

This method provides a useful way of preparing nanorods for experiments, as individual nanorods can be probed depending on the density of nanospheres in the mask. Due to the amount of material removed in nanorod processing however, this method is only suitable for measuring physical properties of a structure - Enhancement compared to an as grown structure is difficult to see on a large scale.

6.2.2 Separating and Depositing Single Nanorods

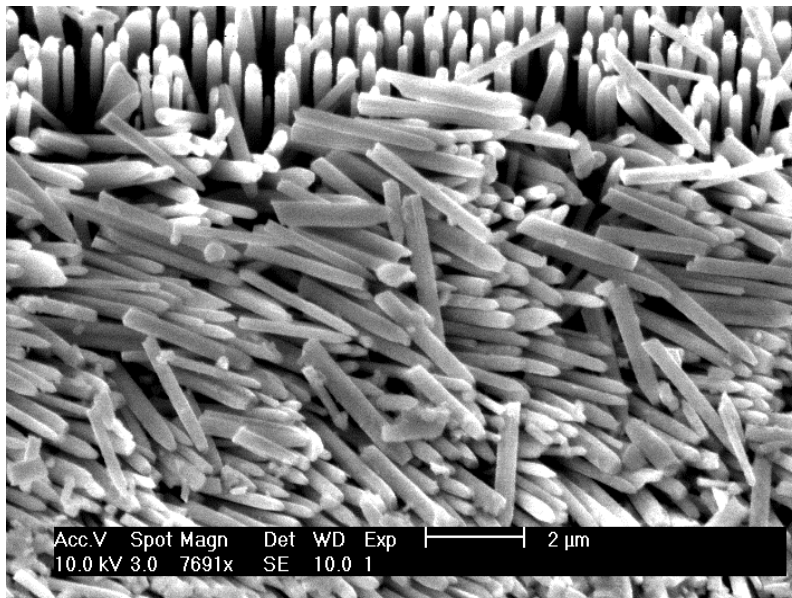


Figure 6.3: SEM image of loose nanorods (prepared using a self aligned Ni mask) separated from the substrate using a diamond tipped cleaving tool.

Nanorods are removed from an as etched sample using a mechanical process in iso-propyl alcohol (IPA) inside a cuvette. Similar studies have been performed with this removal process with no apparent damage caused to the structures [8, 9]. A diamond tipped cleaving tool is dragged across an as etched nanorod sample suspended in IPA, which acts to snap off NRs and allow them to suspend in the

solvent. Figure 6.3 shows a typical nanorod sample consisting of a GaN/InGaN QW structure with underlying GaN bulk layer grown on sapphire after the nanorod removal process. It can be seen that most NRs break off at the base, which occurs under the condition that the etch depth is suitably deep, and the nanorod sidewalls are parallel, meaning thickness of the nanorod is largely unchanged throughout its length.

Following the mechanical scratching process, the sample and NRs suspended in IPA are subject to an ultrasonic bath to further remove loose NRs from the sample. The cuvette containing IPA, sample and loose NRs is then subject to a large centrifugal force in a centrifuge. This separates the loose NRs and sample, creating a small pellet of loose NRs in the narrow base of the cuvette while the substrate stays above at the top of the cuvette. After this process the sample can be removed along with some IPA solvent, to allow a concentrated nanorod solution to be formed. Further ultrasonic treatment in an ultrasonic bath separates the nanorod pellet and equally distributes the NRs throughout the solvent, allowing them to be deposited onto a new substrate.

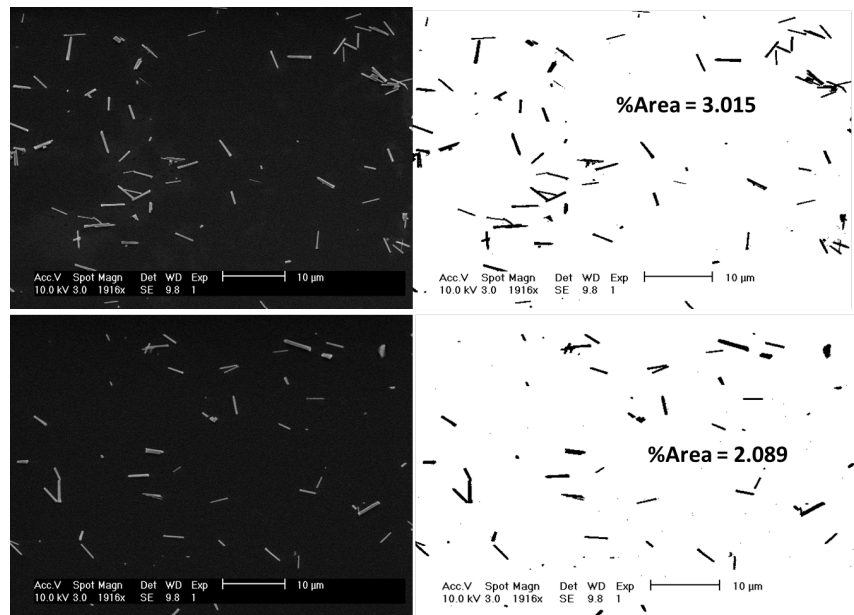


Figure 6.4: SEM images of single nanorods analysed by imageJ, showing density of nanorods per area.

Deposition by spin coating produces a very low concentration of NRs per area, making finding individual NRs difficult as their size is below that visible with optical microscopy techniques. An improved method was found to be drop casting - varying the concentration of IPA in the cuvette allows more or fewer NRs per area on a sample after drop casting with a micro pipette, and taking the solution from the same level in the cuvette after ultrasonic treatment allows good repeatability.

6.2.3 Substrates for Single Nanorod Deposition

The samples used to deposit single NRs onto are Si substrates that can be processed with Ag film coatings. Si is the preferred choice, as it is simple to process and allows equal sized samples for accurate drop casting. It also doesn't reflect or emit photons in the visible region allowing very low noise PL measurements to be taken. As Si is reasonably conductive, it allows good quality SEM images to be taken of the NRs (without excess sample charging), to aid in locating and re-locating individual structures.

Initially a 200 nm layer of SiO_2 is deposited onto the Si carrier wafer using a PECVD process, to produce a flat insulating layer for NR or metal deposition. A thin layer of Ag is deposited onto the SiO_2 using a thermal evaporator, with a thickness in the range 50 - 100 nm - the appropriate thickness to best obtain SP enhancement of InGaN structures as discussed in chapter 5. To insulate this layer from the NRs to be drop cast, a thin layer of SiN or SiO_2 is deposited onto the Ag film at low power using a PECVD, or using an e-beam deposition system, giving coverage in the 5 - 10 nm thickness range. This is thick enough to insulate the NR surface from the Ag film to reduce carrier leakage, yet thin enough to allow SP coupling to take place. Finally NRs are drop cast onto the sample, and measurements can be taken.

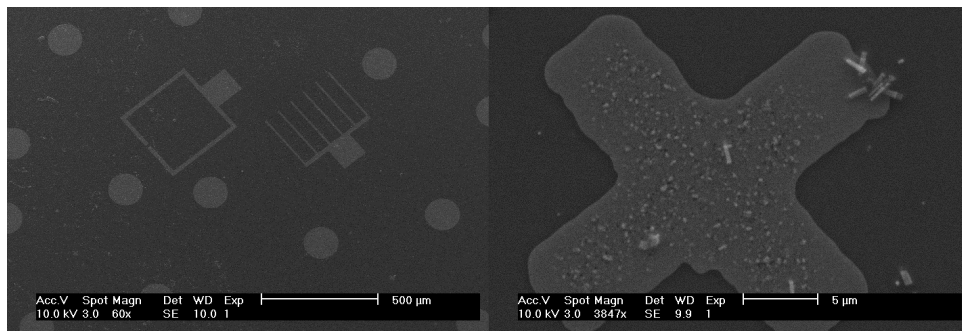


Figure 6.5: SEM images of single nanorods on Ag shapes deposited onto Si using a lithographic n-contact mask and lift off process. The left image shows the substrate with multiple $50 \mu\text{m}$ diameter Ag circles and other patterns allowing a map of single nanorod locations to be made. The right image shows a much smaller alignment cross with a single nanorod in the centre.

The individual NRs adhere to the substrate by stiction, and are generally well adhered to the surface if lying horizontally [10]. The substrate can be inverted without effecting the location of the NRs, however immersion in a liquid or ultrasonic treatment can dislodge them from the surface if required.

As discussed in chapter 4 the software package imageJ can be used to analyse nanostructures. This program is also useful for analysing the distribution of single NRs on a carrier wafer. Illustrated in Figure 6.4 are two SEM images with different

density of loose NRs (left), and the analysed image (right). The software picks out individual NRs, and can be used to calculate size distributions and average area covered. This allows density of single NRs to be measured, allowing comparisons between samples to be made.

On a planar substrate it is virtually impossible to re-find an individual NR after observation with an SEM or measurement in a μ PL system due the size of the structures. To allow re-measurement of single NRs and hence improve measurement repeatability a patterned substrate is used. Using an LED n-contact mask and photolithographic lift off process, a pattern of Ag structures can be produced on a Si substrate. Following NR drop casting, single NRs can be found on individual Ag shapes of $50 \mu\text{m}$ diameter. As the features are in a regular grid array, mapping of the sample becomes possible. This is illustrated in Figure 6.5 where NRs are observed on $50 \mu\text{m}$ circular shapes normally used for n-contact deposition (left image), as well as on a smaller lithographic alignment marker (right image).

6.3 Characterisation of Single Nanorod Emitters

6.3.1 Planar and Nanorod Sample Characterisation with Conventional PL

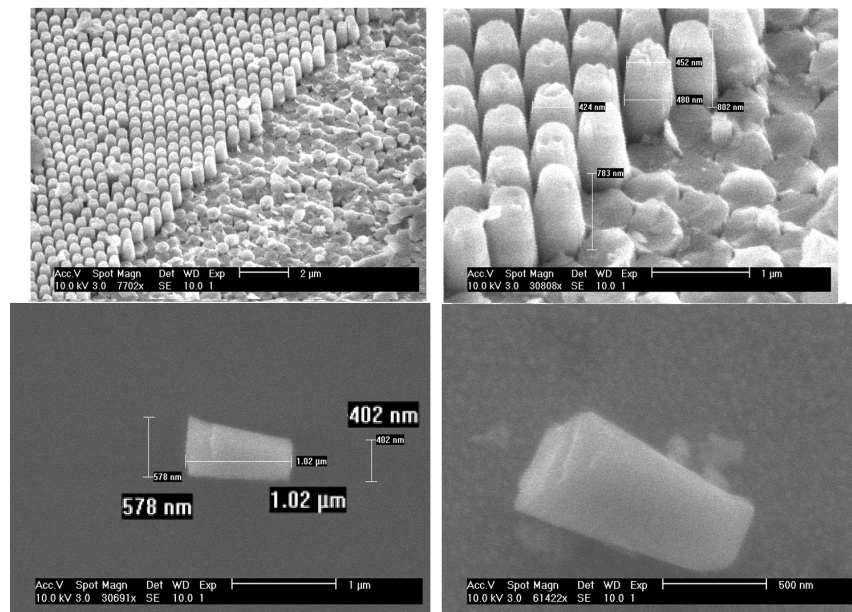


Figure 6.6: SEM images of single NRs fabricated using a uniform 500 nm SiO_2 nanosphere mask. The top images show the sample in an area where NRs have been mechanically removed. The lower images show loose NRs on SiO_2 deposited onto a Si substrate (left) and a thin 5 nm SiO_2 layer deposited onto a 100 nm Ag film which is in turn deposited onto SiO_2 on a Si surface (right)

The samples used for single NR processing are InGaN/GaN 5QW structures with a central emission wavelength of 450 nm. The NRs used for optical testing are fabricated using a uniform 500 nm nanosphere mask creating approximately 500 nm diameter NRs. This ensures repeatability between single NRs as the shape and size of each NR is identical.

The initial NR array is fabricated on a 5 mm² sample etched to a depth of 1 μ m, and the resultant NRs have slightly inclined sidewalls, as seen in Figure 6.6.

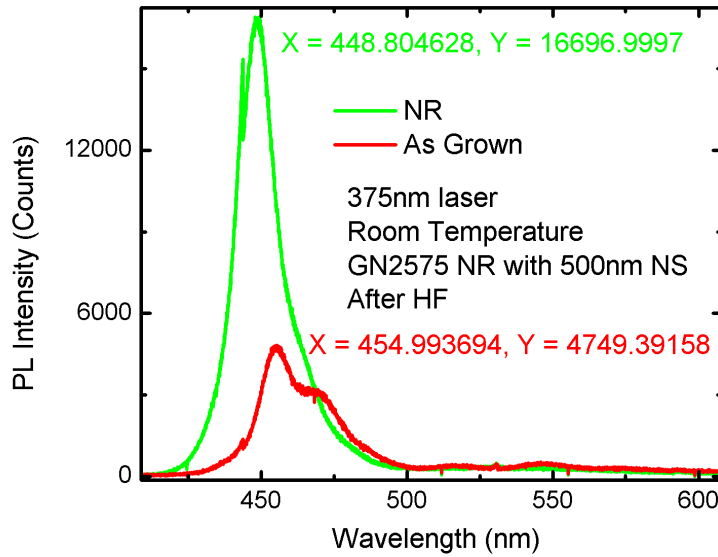


Figure 6.7: PL spectra of a planar as grown and NR processed samples fabricated using a uniform 500 nm SiO₂ nanosphere mask showing clear enhancement and central wavelength blue shift.

Conventional PL measurements of the original as-etched NR array show an enhancement over a planar as grown sample of over three and a half times, as seen in Figure 6.7, as well as a blue shift of the central peak wavelength of 5 nm, both due to strain relaxation and alleviation of the QCSE. This is measured with a laser spot over 200 μ m in diameter meaning many NRs are illuminated by the laser.

6.3.2 MicroPL Characterisation of Single Nanorods

After the single nanorod removal process discussed in section 6.2.2 the NR solution is deposited onto Si wafer tiles with a 300 nm SiO₂ PECVD deposited layer on the surface. An initial experiment is performed using a Si/SiO₂ tile with a 100 nm Ag film deposited onto the surface, followed by a thin 5 nm film of SiO₂ deposited by e-beam evaporation. The Ag film is photolithographically patterned onto the substrate creating areas with and without Ag, as discussed in the previous section.

MicroPL System

The samples are measured with a μ PL system, where PL excitation and collection are accomplished using a microscope objective to allow measurement of very small features. The system used in this work is a flexible set-up that was developed to use several different excitation sources, stages and detectors, as illustrated in Figure 6.8. A 375 nm laser is used as an excitation source in this work and a highly sensitive monochromator and CCD used for detection. The samples are placed in a vacuum using a cryostat stage to avoid NR degradation due to the high laser power density, but are measured at room temperature unless otherwise stated.

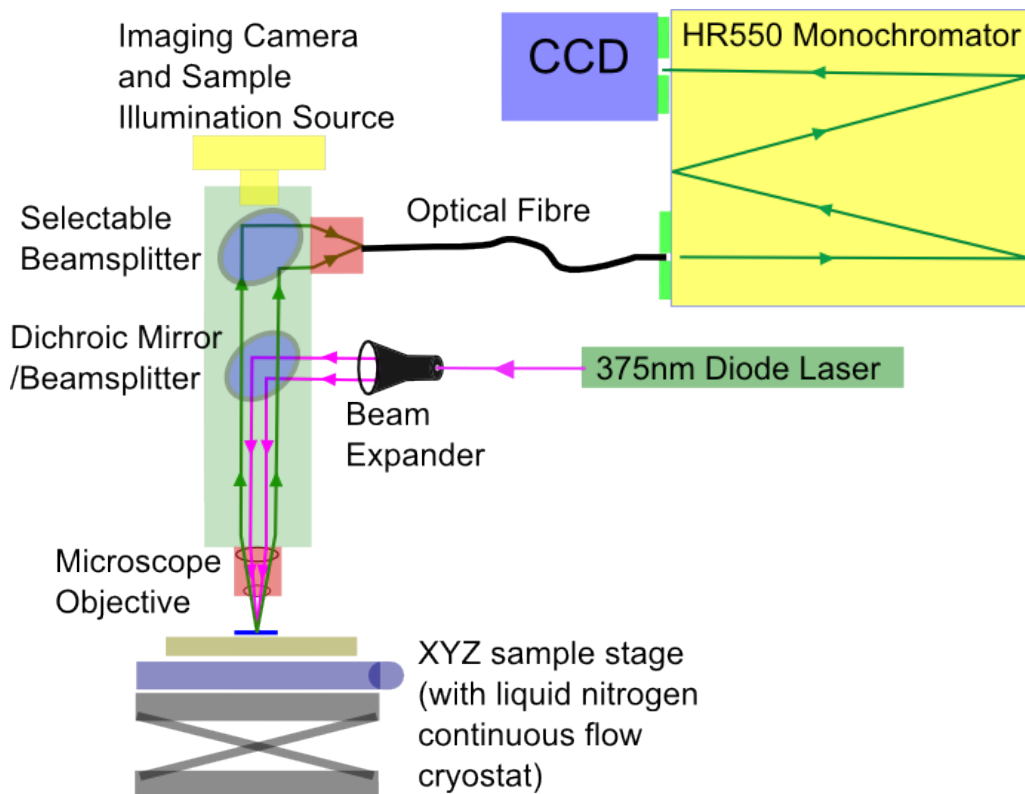


Figure 6.8: Micro-photoluminescence system used in this work.

A high quality long working distance Mitutoyo microscope objective is used as the main excitation and collection optic, and is mounted to a Navitar microscope tube, used to house various beam splitters and a camera.

The camera and a light source are mounted at the top of the tube, allowing illumination of the sample and a view of the laser spot and sample under test.

Lasers mounted externally are directed into the tube via a beam expander, and down to the microscope objective and sample by a dichroic mirror acting as a beam splitter with a cut off wavelength of approximately 410 nm. This mirror allows the UV laser line (with wavelength lower than 410 nm) to be reflected down towards the sample, but allows the emitted visible light (with wavelength longer than 410 nm) to pass back through and up into the tube for collection.

A second beam splitter system allows the emitted light to be directed into a fibre optic cable, where it can be transferred to a high resolution monochromator (0.025 nm wavelength resolution) and peltier cooled CCD detector. The secondary beam splitter is selectable, and can allow 100% of the emission into the camera to help with sample location and focusing, before being switched to direct light to the optical fibre and into the detector to maximise the sample emission signal.

Due to the high magnification of the objective along with a small laser spot size and therefore test area, a movement stage with very high accuracy is required for focusing. A custom XYZ directional stepper motorised stage from Standa is employed, to carefully control the position of a sample with step accuracy of below $1\ \mu\text{m}$.

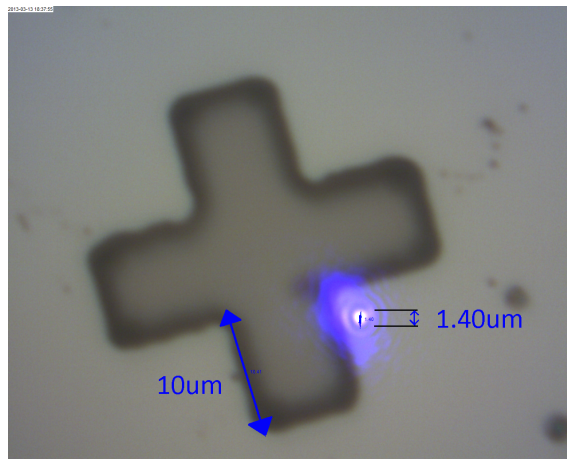


Figure 6.9: Estimate of the laser spot diameter from a μPL system observed through a microscope camera. The cross shape is a photo-lithographic alignment marker with known dimensions.

A laser spot size smaller than $1.5\ \mu\text{m}$ is attainable with this system after careful alignment of the optics as observed in Figure 6.9. To achieve this, the microscope objective must be completely filled, ideally with coherent light to maximise the lens area - accomplished using a beam expander. The high accuracy of movement of the sample stage in the Z-direction allows the system to be focused correctly by moving the sample and stage assembly vertically at 1/8th step increments of below $0.2\ \mu\text{m}$.

Increased Emission from SP Enhanced Single NRs Measured with MicroPL

Single NRs excited by the 375 nm laser are observed in Figure 6.10, using the USB microscope camera attached to the μPL system which views through the excitation and collection objective. Low excitation laser power is used for these images, and each end of the single NR can be seen illuminated.

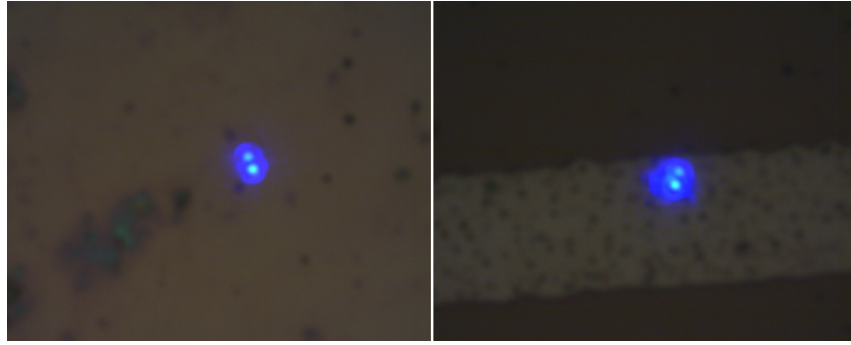


Figure 6.10: Optical microscope images taken using a USB microscope camera attached to a μ PL system showing single NRs excited at low excitation power using a 375 nm laser. Images show a single loose NR on SiO_2 deposited onto an Si substrate (Left) and a single NR on a thin 5 nm SiO_2 layer deposited onto a 100 nm Ag film, which is in turn deposited onto SiO_2 on an Si surface (Right).

The uniformity between different NRs on the same Si carrier wafer is illustrated in Figure 6.11, where four individual NRs are measured across a sample and the spectral intensity compared. The variation between NRs due to changes in alignment of the characterisation system and differences between individual NRs is below $\sim 20\%$. This suggests good uniformity between NRs, however this variation must be taken into account with claimed enhancement between structures.

An increase in emission intensity is observed by the USB camera after illuminating single NRs lying on a thin SiO_2 layer on top of 100 nm Ag, illustrated in Figure 6.12. The PL enhancement as a result of the Ag film is almost six times, as observed in Figure 6.13. This combined with the initial enhancement over the planar as grown sample suggests a potential maximum enhancement of over twenty times for the QWs in this structure due to strain relaxation and SP coupling. A blue shift in the central peak wavelength is observed, as is a change in the peak shape for the single NR coupling to SP modes. The blue shift and emission enhancement are explained as in chapter 5, where the initial excited excitons can couple to SP modes very quickly - resulting in increased emission efficiency. The carriers may also transfer to an SP mode before relaxing to the band edge, resulting in the shift in central emission energy.

To further investigate the SP coupling depth and the enhancement caused by SP coupling, three Si substrates were fabricated with a 100 nm Ag film, and increasing SiO_2 interlayer thickness of 5 nm, 20 nm and 50 nm. From chapter 5, the SP coupling maximum fringing distance is approximately 47 nm, and depends on the dielectric properties of the separating layer. The results illustrated in Figure 6.14 show that the sample with 5 nm SiO_2 interlayer produces enhancement close to the maximum previously observed, the 20 nm interlayer sample shows enhancement at

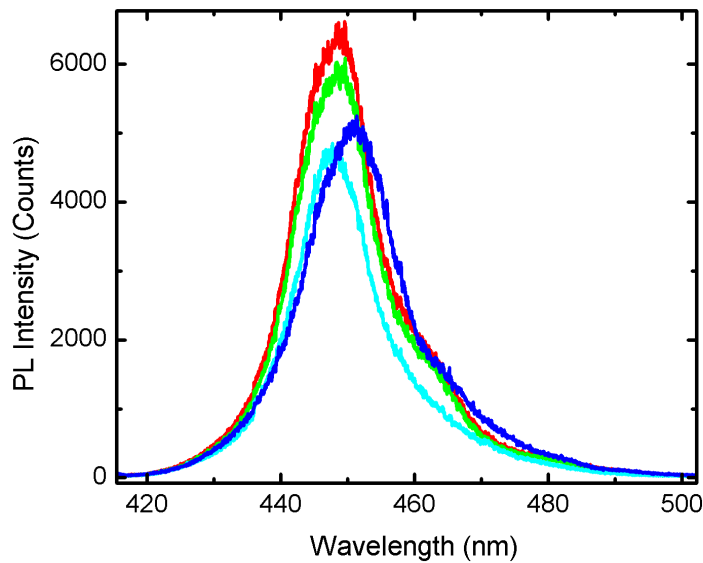


Figure 6.11: PL spectra of four individual single NRs on a 5nm SiO₂ interlayer on 100nm Ag. The difference between highest and lowest peak intensity is 20%, suggesting uniformity between individual NRs is good.

a reduced rate, and the 50 nm sample shows zero enhancement over a single NR placed on a standard SiO₂ film without Ag. This well agrees with the SP fringing field calculation, where the sample with a 20 nm interlayer has reduced SP coupling, and the sample with 50 nm interlayer places the single NR out of the SP fringing field, therefore stopping SP coupling from taking place.

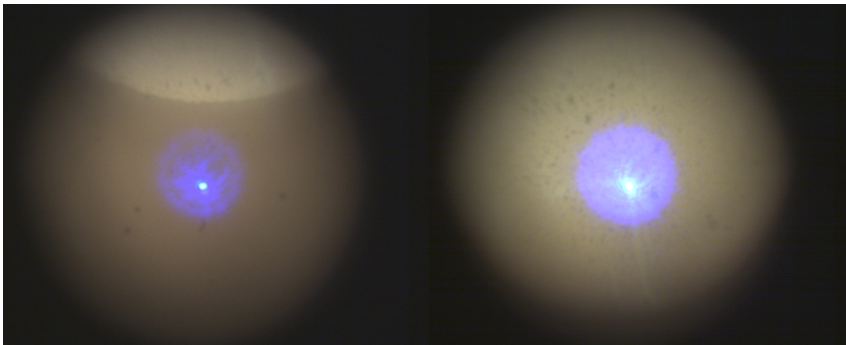


Figure 6.12: Microscope images taken from μ PL system showing a single excited NR on SiO₂ substrate (Left) and a single NR on a 100 nm Ag film with thin SiO₂ interlayer (Right) at the same 375 nm laser excitation power. A clear increase in brightness is observed between the two otherwise identical NRs.

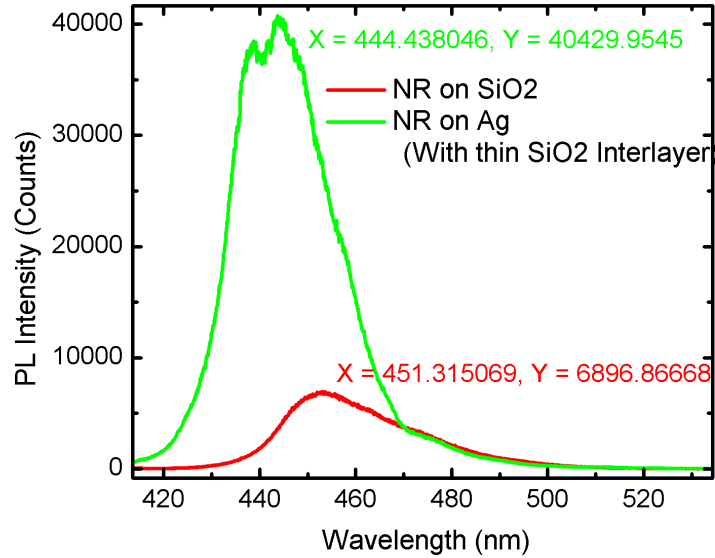


Figure 6.13: μ PL spectra of single NRs fabricated using a uniform 500 nm SiO_2 nanosphere mask. The red trace is a loose NR on SiO_2 deposited onto an Si substrate, and the green trace is a loose NR on a thin 5 nm SiO_2 layer deposited onto a 100 nm Ag film. An intensity enhancement of almost six times is observed as well as a blue shift in the peak emission wavelength.

6.4 Study of Surface Plasmon Induced Single Nanorod Lasing

The sharp peak observed in the PL spectra of the 5nm SiO_2 interlayer sample in Figure 6.14, as well as the satellite peak in Figure 6.13 are potentially caused by stimulated emission from the NR. In the high magnification image in Figure 6.10, both ends of the NRs appear bright, suggesting light may be reflecting along the NR, with the ends acting as the facets on each end of a cavity. In this situation the InGaN/GaN MQW stack would be the gain region. If a cavity exists axially along the NR and modes are generated resulting in stimulated emission, coupling to SPs in the Ag film could cause an enhancement in the emission.

A similar result is observed in CdS NRs coupled to an Ag film by Oulton et al. [3], and by Lu et al. with GaN core-shell MBE grown NRs [6], however there are no reported results for InGaN/GaN top down fabricated NRs coupled to Ag SPs.

The sharp PL spectral peak is observed only in some single NRs in close proximity to an Ag film. The investigation of the influence SP coupling has on lasing from InGaN nanorods is performed in the following section.

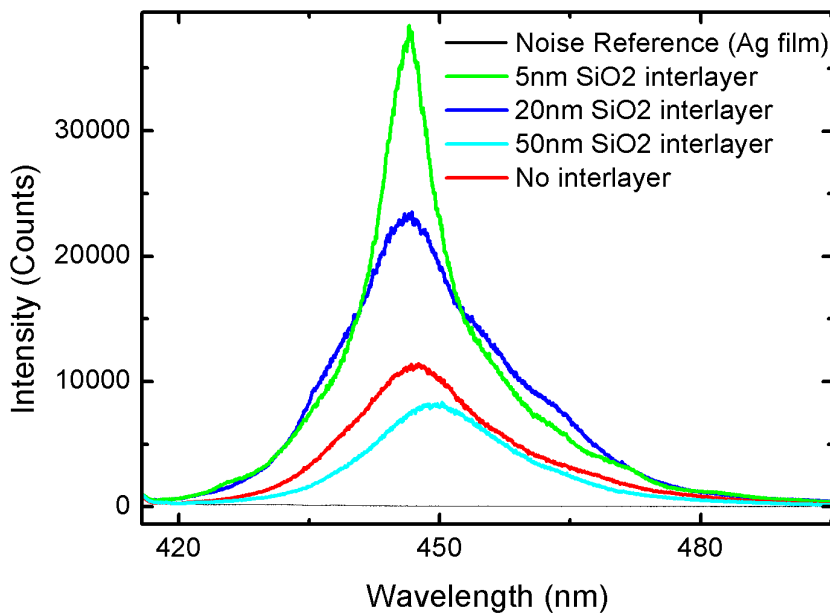


Figure 6.14: PL spectra of single NRs on a 5 nm, 20 nm and 50 nm SiO₂ interlayer on 100 nm Ag. The difference in PL spectra intensity is caused by the SP coupling distance.

6.4.1 Stimulated Emission from Single Nanorods Enhanced by Surface Plasmon Coupling

High brightness, coherent and compact light sources are imperatively desired as the basic building block for photonic integrated circuits system-on-chip devices and nanoscale optical lithography [11, 12]. One option to achieve this is to develop an ultra-small laser, but miniaturisation of a conventional lasing cavity is difficult due to the diffraction limit of $\lambda/2n$, where λ is the free space wavelength and n is the refractive index.

A number of studies have developed solutions to this issue, using nanowires, core-shell structures or photonic crystal nanocavities [13–16]. However, there are still three main challenges to overcome to realise coherent room temperature nanolasers:

- Stimulated emission thresholds become high as the dimensions of the cavity are decreased, reducing laser performance.
- Single mode lasing is hard to develop as fewer parameters can be adjusted on the nanoscale due to fabrication difficulties. This is essential for signal processing applications however requiring accurate single modes [17].
- The majority of reported structures using the above approaches are difficult to develop practically as electrical injection is often not discussed. A key component for optical integrated circuits is the ability to electrically drive lasers at beyond the diffraction limit in the nanometre range.

An alternative method to realise a nanolaser is to make use of SP coupling. As the evanescent electric field of the SP is perpendicular to the propagation direction (interface), SPs are tightly confined in a scale much smaller than the wavelength of emission (incident) light [18].

In 2003 Bergman and Stockman discovered macroscopic coherent SP modes could be built by exploiting a metal/dielectric component on the nanometre scale - termed surface plasmon amplification by stimulated emission of radiation (spaser) [19]. Ohmic loss hinders the development of plasmonic lasers however as much of the energy will dissipate in the metal layer during the SP propagation along the metal/dielectric interface. Theoretical studies show such loss can be significantly reduced by the gain medium in a hybrid plasmonic waveguide [20]. Several groups have demonstrated spasers or spaser-semiconductor hybrid lasers with this kind of plasmonic waveguide by using OG-488 dye nanoshells, CdS nanowires and InGaN MBE grown nanorods as the gain medium [3, 6, 21].

In the following section, details of a room-temperature low threshold spaser/InGaN MQW structure are presented. The nanorod consists of an LED structure of p-GaN, InGaN MQWs and n-GaN regions, and the MQWs act as the gain medium inside a Fabry-Perot cavity along the length of the nanorods. The spaser hybrid is capable of working under the diffraction limit and with a single mode. As the nanorods are fabricated using a simple top-down method from a conventional epitaxial film containing both n- and p-GaN doped layers, there exists the potential to fabrication an electrically pumped spaser in the near future.

6.4.2 Sample Fabrication

In the previous section, uniform nanorods were used to accurately compare enhancement between samples, showing a clear increase of emission due to SP coupling as well as stimulated emission. The SiO₂ nanosphere mask produces nanorods with an angled sidewall due to the circular profile of the sphere mask. Etch depths of approximately 1 μm also appear to be the maximum due to the narrow gap between spheres. Because the cavity in the lasing nanorods is parallel with the sidewalls, reducing the sidewall angle will reduce losses in the cavity and improve stimulated emission.

To produce longer, thinner nanorods with very low angle sidewalls, a Ni self aligned mask is used, as in chapter 4. The Ni self aligned mask produces improved sidewalls due to the tough metal mask and SiO₂ interlayer used, and the increased gap between nano-islands allows deep etching into the GaN material. The process is also easy to develop across a wide range of sample sizes with different surface morphology.

The nanorods used were fabricated from a commercial LED epiwafer, which was grown by MOCVD on a c-plane sapphire substrate. The structure of the device consists of a nucleation and bulk GaN region, followed by $2.8 \mu\text{m}$ of Si doped n-GaN material. The active region is an InGaN/GaN 10QW heterostructure with GaN barrier thickness of 13.4 nm and QW thickness of 2.9 nm. A 23 nm thin AlGaIn electron blocking layer is grown after the active region, and 200 nm of Mg doped p-GaN is grown to finalise the structure.

The epiwafer was fabricated into nanorods by top-down dry etching as in chapter 4 using an ICP-RIE and low etch power of 50 W RF to reduce QW damage. The SiO_2 etch mask is removed with a HF treatment. This is an important step to improve the reflectivity of the NR top surface, which will act as one half of the Fabry Perot (FP) cavity.

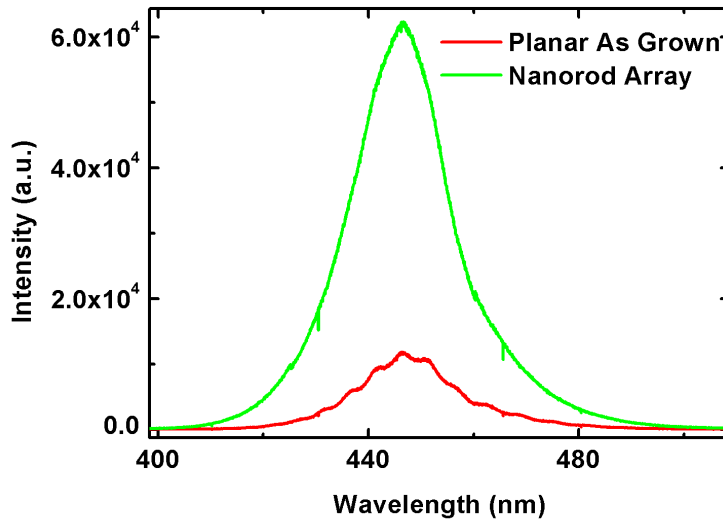


Figure 6.15: Conventional PL spectra of an LED planar as grown sample and nanorod array sample, showing a clear increase in emission intensity as a result of nanorod fabrication.

The conventional PL enhancement of the NR sample over the as grown is observed in Figure 6.15. Significant enhancement is found due to alleviation of the piezoelectric field by strain relaxation [22]. This is a vital attribute that leads to improved optical gain of the InGaIn MQWs when used in a stimulated emission application [23].

The nanorods are separated using a diamond tipped scribe and the process discussed earlier in this chapter, and Si substrates are used for nanorod deposition. Initially a 500 nm thick SiO_2 layer is grown on the pre-cleaned Si substrate, followed by an 85 nm film of Ag deposited at a rate of 0.1 nm/s. A thin SiO_2 insulating dielectric layer is then deposited by e-beam evaporation. Deposition of the single

nanorods is by drop casting as before, forming the plasmonic nanolaser structure as illustrated in Figure 6.16 (a).

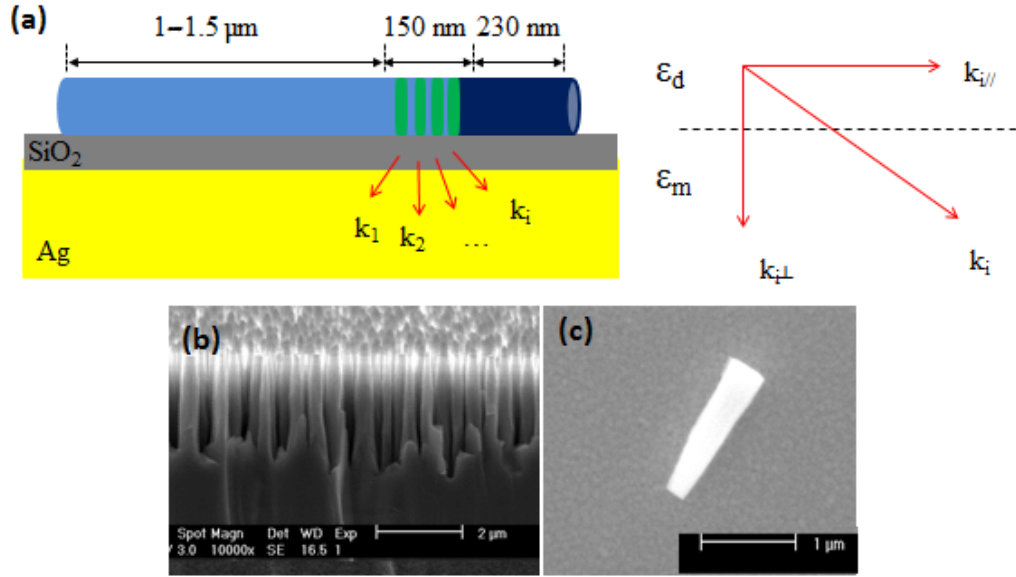


Figure 6.16: (a) Diagram of the structure used in this work. (b) Fabricated nanorod array and (c) individual nanorod separated from the as etched array.

A nanorod on SiO₂ structure was fabricated to act as a comparison sample, which is composed of the same MQW nanorods placed directly onto a SiO₂ substrate, without an Ag film (and therefore without SP enhancement).

The fabricated nanorods are shown in SEM images in Figure 6.16 (b), where it can be seen that the sidewalls of the nanorods are predominately straight, with a slight incline towards the top of the nanorod where the MQW heterostructure resides. This morphology is formed because InGaN material generally etches faster in the nitride ICP etch used, and is uncovered early in the etch (and therefore potentially etched for longer than the underlying n-GaN).

An individual nanorod, placed on Ag thin film is pictured in Figure 6.16 (c). The nanorods break away from the substrate leaving a smooth and flat surface, creating a good cavity with parallel facets allowing reflection between the bottom and top of the nanorod.

6.4.3 Theory of InGaN Single Nanorod-Surface Plasmon Stimulated Emission

In the structure illustrated in 6.16 (a), the electric field can be strongly compressed within the SiO₂ interlayer between the nanorod and Ag, allowing a long propagation distance of SPs in the structure, potentially up to tens of microns [3, 24]. Due to this, SP standing wave modes can be formed within the length of the nanorods.

The gain medium of the plasmonic nanolaser is the InGaN/GaN MQW active region. A study by Zhao et al. using $k \cdot p$ theory suggests this can create a large optical gain of several 1000 cm^{-1} in the blue and green wavelength regions [25]. Such a large optical gain will effectively compensate for any optical losses in the plasmonic nanolaser. This mechanism, along with the confinement and low loss propagation of SPs in the underlying Ag film coupling to excitons allows stimulated emission to take place.

The shortest length of InGaN/GaN nanorod to support a conventional laser can be evaluated from equation 6.1, where L is the nanorod length, α is the gain and R_1 and R_2 are the reflectance of each end of the cavity, the top and bottom of the nanorod in this case.

$$L = \frac{1}{2\alpha} \ln \frac{1}{R_1 R_2} \quad (6.1)$$

The reflectance of a GaN and air interface can be derived from equation 6.2, where n_{GaN} and n_{air} are the refractive indices of GaN and air, 2.5 and 1 used here.

$$R = \left| \frac{n_{\text{GaN}} - n_{\text{air}}}{n_{\text{GaN}} + n_{\text{air}}} \right|^2 \quad (6.2)$$

If $\alpha = 5000 \text{ cm}^{-1}$, and ignoring any loss [25], the length of the cavity (nanorod) L must be no less than $1.7 \mu\text{m}$. In a practical application, due to scattering, non-radiative emission and cavity losses, the required nanorod length is likely to be longer to produce stimulated emission from cavity reflections and semiconductor gain alone [26, 27].

As the nanorods used in this work are approximately $2 \mu\text{m}$ long, and the gain region is actually the much thinner InGaN QW material active area, lasing should be very difficult to see from a nanorod on SiO_2 structure. This further suggests that any observed stimulated emission is a direct result of the SP coupling effect.

6.4.4 Excitation Power Dependant MicroPL

Excitation power dependent emission spectra at room temperature from the MQW nanorod/ SiO_2 /Ag film structure is shown in Figure 6.17 (A).

At a low excitation laser power of 0.09 mW, a broad spontaneous emission spectrum is observed with the centre located at 438 nm and a FWHM of over 40 nm. The peak intensity then appears to increase drastically along with a prominent FWHM decrease as the excitation power increases.

A sharp spike appears at 438.5 nm at a threshold of 0.3 mW laser power, corresponding to a power density of approximately 10.5 kW/cm^2 . Such a low threshold at room temperature is comparable to the lowest thresholds reported, performed at

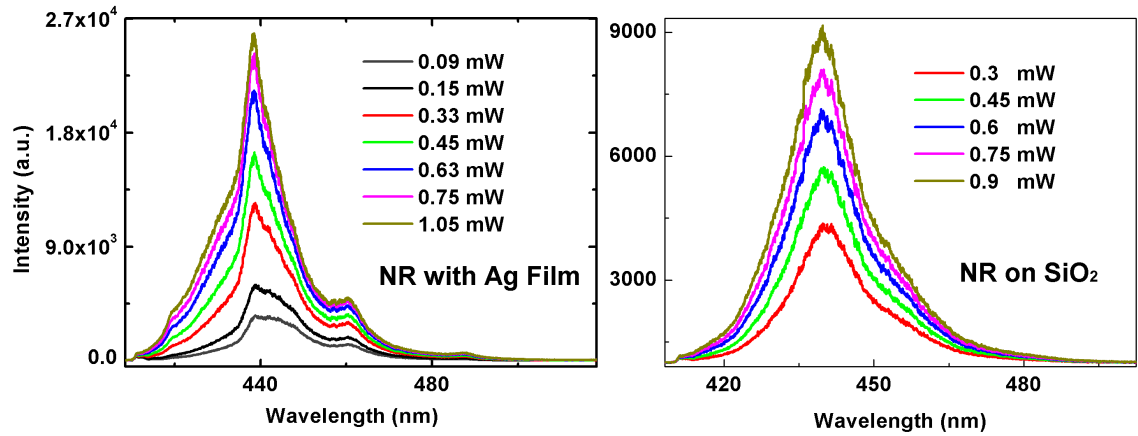


Figure 6.17: (A) Emission spectra of a single nanorod coupled to an Ag film. (B) Emission spectra of a single nanorod on SiO_2 without SP coupling.

low temperature using InGaN/ SiO_2 /MBE grown-Ag films (2.1 kW at 8 K, and 3.7 kW at 78 K) [6].

In contrast to this, a continually broad spontaneous emission spectra is observed from the MQW nanorod on SiO_2 structure without a Ag film, as shown in Figure 6.17 (B). A centre wavelength of 440 nm is observed along with little FWHM change with increasing excitation power for this structure.

Under identical measurement conditions, a large difference in the light intensity between the conventional nanorod on SiO_2 and SP enhanced NR is observed. The intensity of the plasmonic nanolaser is over three times that of the spontaneous emission under an excitation power of 0.75 mW. This enhancement of the emission is linked to the strong SP coupling, which is discussed in detail in the following section.

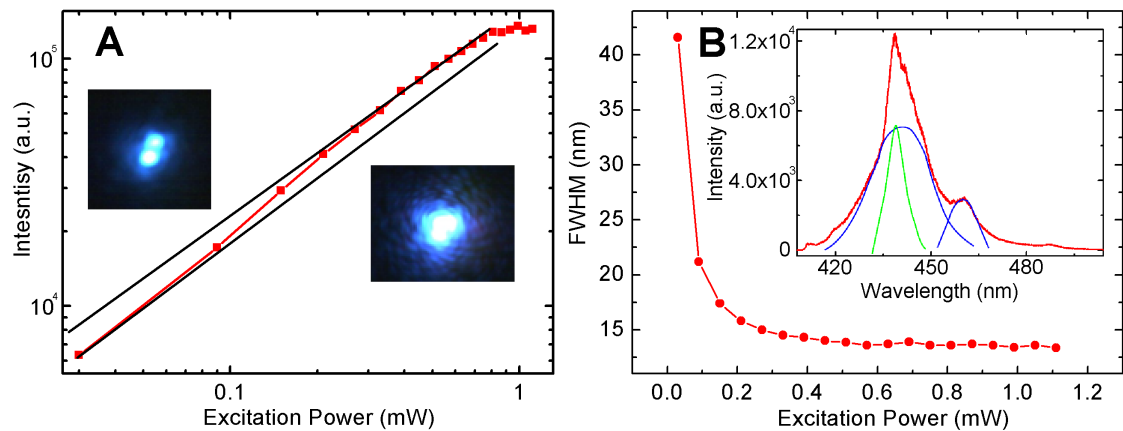


Figure 6.18: (A) Integrated emission spectra of single nanorod coupled to an Ag film on a L-L plot showing a clear threshold. (B) FWHM with increasing excitation power for the same sample. (B - Inset) Separation of stimulated and spontaneous emission components by data fitting.

The integrated intensity of the single nanorod in close proximity to an Ag film is plot on a log-log (L-L) scale in Figure 6.18 (A). A non-linear “s”-shape curve is observed with increasing excitation power, indicating possible lasing behaviour and a threshold between spontaneous and stimulated emission regimes.

The threshold read from the L-L plot is approximately 0.3 mW, which is consistent with the sharp spectral peak observed in Figure 6.17 (A). At higher excitation energy, the emission power appears to saturate, as a consequence of the efficiency droop effect in InGaN QWs and the extremely high excitation power density used.

The inset of 6.18 (A) shows optical images obtained from the μ PL camera showing a single nanorod before and after lasing. Clear diffraction patterns are observed in the emission above the laser threshold, suggesting the emitting light is highly coherent as would be expected in a stimulated emission regime.

The FWHM of the plasmonic nanolaser is plot as function of excitation power in Figure 6.18 (B). The FWHM of the spectra decreases dramatically after the threshold of 0.3 mW, corresponding to 6.18 (A) well. The FWHM at a high excitation power of 1.05 mW is 13.37 nm, significantly lower than the spontaneous emission regime in the conventional nanorod on SiO₂ without SP enhancement.

The quality factor Q of the cavity can be evaluated using equation 6.3, where λ is the peak wavelength of the emission and w is the FWHM [28]. A Q value of 34 is obtained from this structure at the highest excitation power.

$$Q = \frac{\lambda}{w} \quad (6.3)$$

This relatively low value of Q is influenced by the broad spontaneous emission spectrum which the stimulated emission peak overlaps. This is demonstrated in Figure 6.18 (B) inset, where the spectra can be broken down into multiple peaks consisting of both spontaneous (blue) and stimulated emission (green) regimes.

The plasmonic nanolaser in this work appears to emit under a single mode, differentiating it from the ones reported previously [3, 6]. As the cavity length of less than 2 μ m is short in this case, and mode spacing is inversely proportional to the cavity length L ($\Delta\lambda \propto 1/L$), only one cavity mode will operate when $\Delta\lambda$ exceeds the gain medium bandwidth where the emission wavelength falls here [29].

Lasing behaviour does not occur with every nanorod, which is related to the specific morphology of each individual structure. As the nanorods undergo scratching, centrifuging and ultrasonic cleaning during the fabrication process, the facets at each end of the nanorod may be damaged, reducing the cavity reflection and resulting in no observable stimulated emission.

This is illustrated in Figure 6.19, where three nanorods are observed with different cavities.

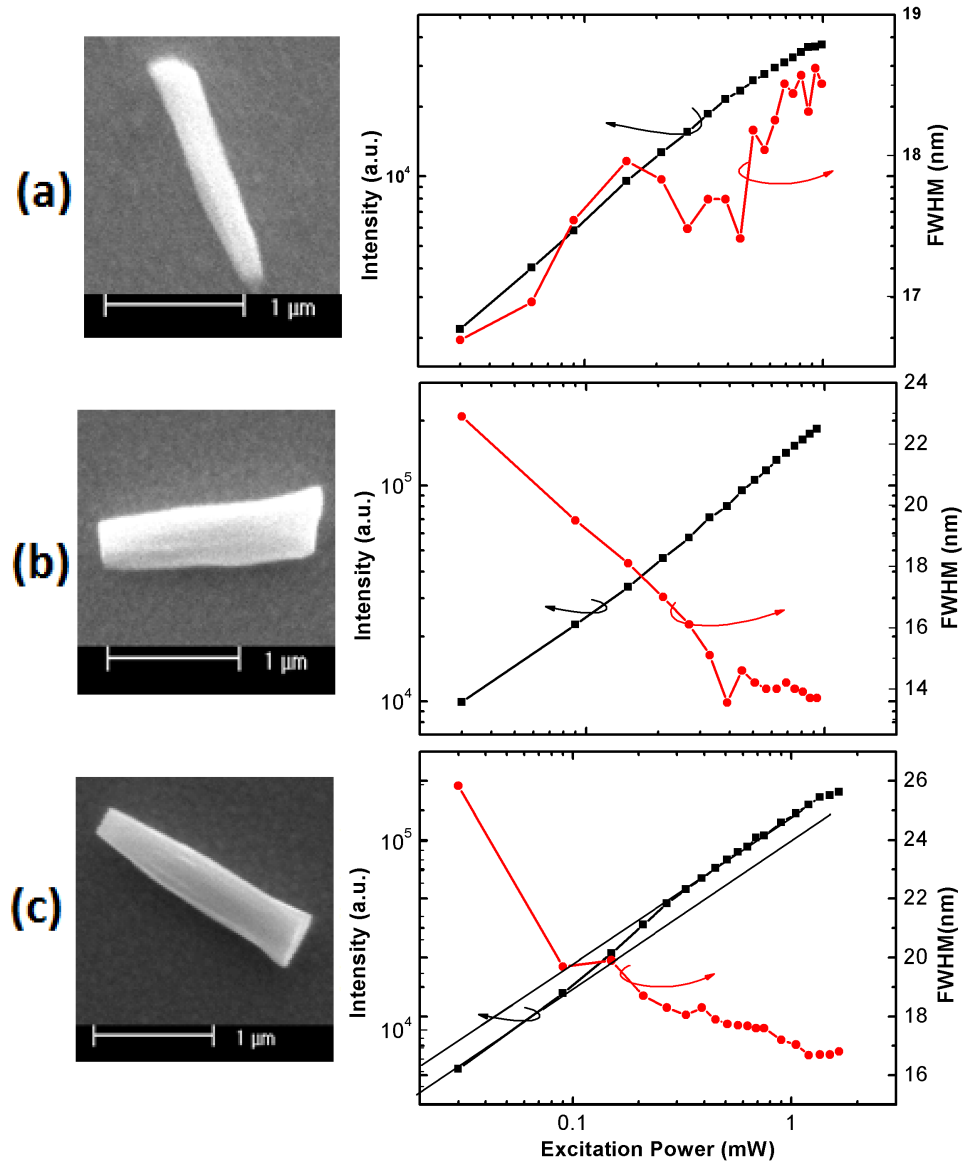


Figure 6.19: SEM and associated PL integrated intensity and FWHM with excitation power for three nanorods with different cavities (top and base of the nanorod).

Nanorod (a) clearly has a conical top and misshapen bottom, resulting in poor facets and therefore poor reflection in the NR plane. This leads to a linear increase in intensity with excitation power on the L-L plot, as associated with spontaneous emission, and a slight increase in FWHM of 1.5 nm due to band filling effects.

Nanorod (b) has a flat top facet, but appears to have snapped with an angled bottom facet. This structure shows a slightly non-linear increase of integrated intensity with excitation power, although no observable threshold kink is seen on the L-L plot. A significant reduction in FWHM is observed, from 23 nm to 13.5 nm, which is related to spontaneous emission enhancement by the single good facet - recognised as amplified spontaneous emission (ASE) [30]. ASE can be interpreted from the features of the nanorod, where as the pair of non parallel facets reflect light, photons will be emitted from the angled surface to free space by the SP modes without

forming a resonating standing wave. Unlike a passive cavity however, some optical gain still exists due to the high reflectance from the one smooth facet. This results in the spontaneous emission being amplified as the excitation power increases.

Finally nanorod (C) appears to have parallel smooth facets, and shows emission properties associated with stimulated emission. The L-L plot of integrated intensity against excitation power has a distinct “s” shaped profile, where a clear threshold of this plasmonic nanolaser is observed around 0.3 mW. A distinct reduction in FWHM is also observed.

From this result, it is clear that plasmonically enhanced single nanorods can be created reliably and are able to operate at room temperature, however the FP cavity plays a key role in the nanorods ability to produce stimulated emission.

It has been reported that a good FP cavity is not essential to producing plasmonic enhanced lasing. In a spaser for example, the cavity is formed by the energy transition from excitons in the semiconductor to energy states in SP modes via a non-emission energy coupling process [19].

In the structures demonstrated here, a large gain is required to compensate for any cavity loss (leakage), non-radiative emission loss (defects and surface states) and SP related propagation losses in the Ag film, which has previously been reported by Oulton et al. [3]. The nanorod itself acts as a plasmonic resonator, allowing SPs to oscillate between the FP facets and increase coupling. As a result, a high density of energy will be confined within the nanocavity, potentially resulting in stimulated emission.

Separation of Nanorod and Ag Film

A set of samples fabricated with increasing SiO₂ film thickness were fabricated, allowing the accurate separation of nanorods from the Ag film, by drop casting single nanorods after SiO₂ layer deposition. Separations of 0, 6, 10 and 15 nm were employed to investigate the effect on single nanorod lasing threshold and proximity to Ag film and hence SP medium.

Figure 6.20 presents the dependence between proximity and lasing threshold, showing a clear change with SiO₂ interlayer thickness. For a large separation, the local field enhancement due to SP coupling is weak, as a result of the evanescent nature of the fringing field, reducing SP interaction. At a low separation, an increase in non-radiative energy transfer loss is expected [31], resulting in a weak SP enhancement and hence low lasing performance (corresponding to a high threshold).

The number of lasing single nanorods found on each sample depends strongly on the structure, with over half the nanorods presenting some evidence to suggested stimulated emission with an ideal 10 nm separation. On the other hand, only one in

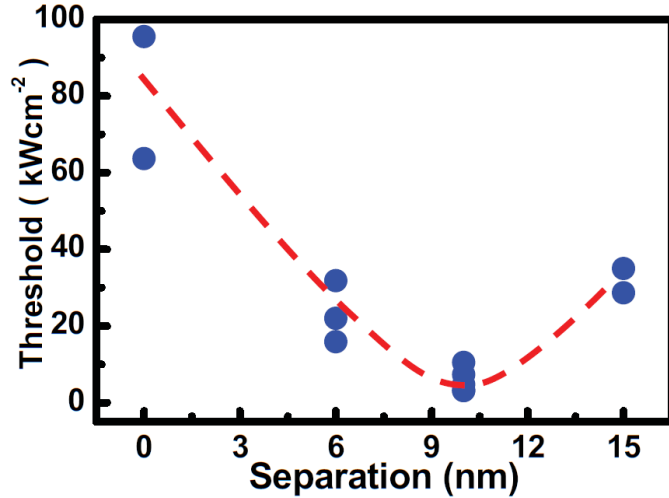


Figure 6.20: Plot demonstrating the dependence of the separation between single nanorod and Ag film on the observed stimulated emission threshold.

10 nanorods show stimulated emission evidence with 0 nm separation (the nanorods directly on an Ag film). This is thought to be a result of high carrier loss into the Ag film, via carrier leakage as well as non-radiative transfer losses.

Three plasmonic nanolasers with different cavities were studied further. These are labelled as structures A, B and C. The nanorods of sample A are identical to the previous structure illustrated in Figure (6.16), however during fabrication no HF clean was performed. This leaves a small SiO₂ cap on the top of the nanorod, which is likely to degrade the cavity by reducing reflectivity at one end. Sample B is fabricated from the same structure, but is treated with HF to remove the SiO₂ material before nanorod removal.

The nanorods of structure C are coated with a nominally thick layer of 10 nm SiO₂, which covers the sidewalls and tops of the nanorod array, and is deposited by e-beam evaporation. The SiO₂ interlayer of the substrate for this sample is reduced to 3 nm, compared to 10 nm for structures A and B. This coating layer can potentially passivate the nanorod surface, preventing chemical absorption/desorption and reaction processes, potentially improving the optical properties of the nanorod.

The integrated emission intensity and FWHM plot as function of excitation power for nanorods A, B and C are shown in Figure 6.21. The observed stimulated emission thresholds are 0.3, 0.1, and 0.63 mW for samples A, B and C respectively. Corresponding FWHM data at 0.5 mW excitation power is 14, 10 and 16.7 nm for nanorods A, B and C. This corresponds to Q factors of 34, 43 and 26.

The first observation is that the threshold of sample B has reduced to one third of sample A, due to a HF treatment before nanorod removal, which strips the SiO₂ mask from the top of the nanorod. This results in an improved facet and therefore increased light reflection inside the nanorod, which reduces the stimulated emission

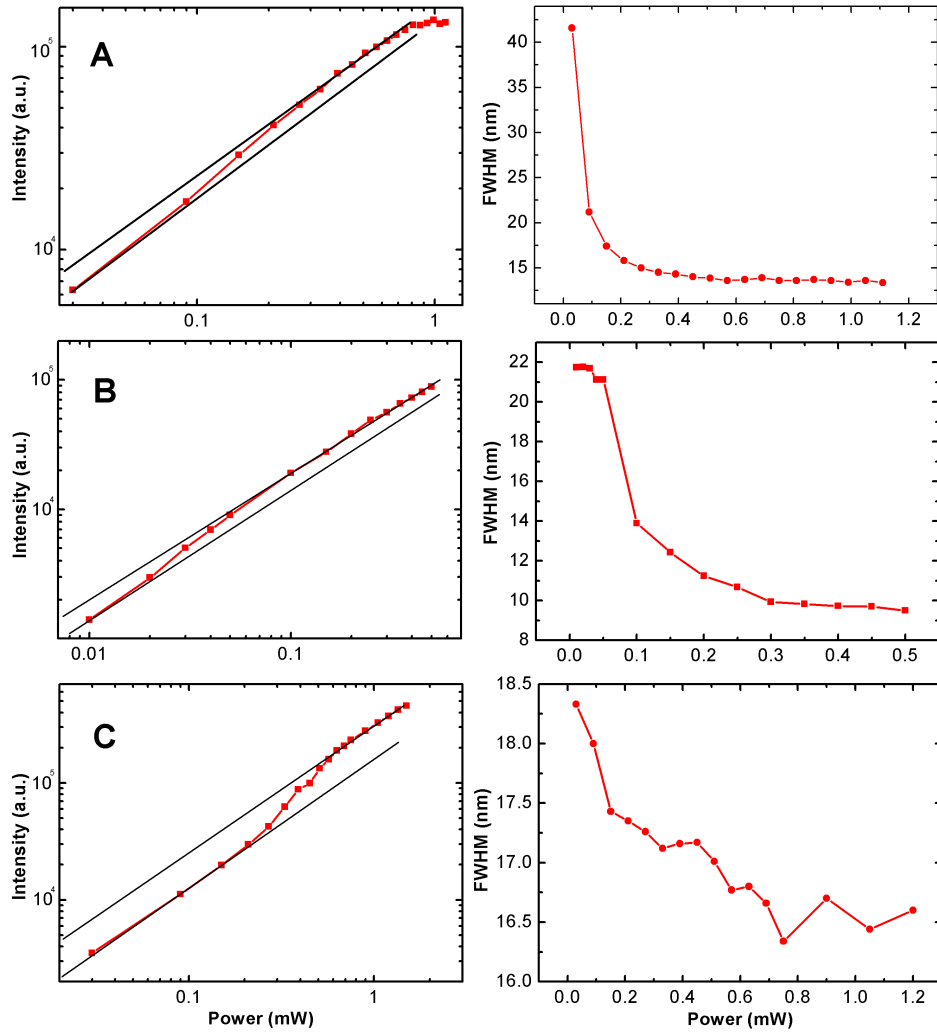


Figure 6.21: (Left) L-L plot of integrated intensity against excitation power for three nanorods with different cavities. (Right) FWHM against excitation power for the same nanorods.

threshold as in accordance with equations 6.1 and 6.2.

The wide range of initial FWHM values for samples A, B and C are related to difficulties in fitting the data and differences between individual nanorods. This could also be related to the high level of spontaneous emission observed. Comparing the integrated intensity against excitation power plots for samples A, B and C, a significant discrepancy can be seen before and after lasing. The change in “s” shift of the threshold is closely related with a key factor in stimulated emission systems, the β factor, which is defined as the fraction of spontaneous emission coupled into the lasing (cavity) mode (or the amount of spontaneous emission coupled along side the stimulated emission).

Beta Factor

The β factor can be high for strong mode confined cavities, such as photonic crystal nanocavities [32], micro-disk lasers [33], and plasmonic nanolasers [3, 6]. Among these, the value of β for a plasmonic nanolaser can be extremely high, as strong coupling between spontaneous emission and SP modes exists.

SP modes can exist as long as the wave vector fits equations 6.4 and 6.5, where $k_{i\parallel}$ and $k_{i\perp}$ are the SP wave vectors parallel and perpendicular to the propagation direction (illustrated in Figure 6.16), k is the free space wave vector at the emission wavelength and ϵ_{GaN} and ϵ_{Ag} are the real dielectric constants of GaN and Ag.

$$k_{i\parallel} = \frac{\epsilon_{\text{GaN}}\epsilon_{\text{Ag}}}{\epsilon_{\text{GaN}} + \epsilon_{\text{Ag}}} \quad (6.4)$$

$$k_{i\perp} = \frac{\epsilon_{\text{GaN,Ag}}^2}{\epsilon_{\text{GaN}} + \epsilon_{\text{Ag}}} k \quad (6.5)$$

As $\epsilon_{\text{Ag}} > |\epsilon_{\text{GaN}}|$, if the small imaginary portion of ϵ_{Ag} is ignored, almost all the wave vectors of the emission light exist perpendicular to the cavity. At the same time, the SPs propagation direction is parallel to the cavity, along the Ag film, resulting in a large amount of spontaneous emission coupling with the SP modes, and generating a large β factor. As this value increases, the transition (lasing threshold) from spontaneous emission to stimulated emission becomes difficult to see resulting in the small change between spontaneous regime and stimulated regime observed in sample A, compared to sample C for example. At the limit of $\beta = 1$, the integrated intensity against input power line will become linear on a L-L plot, and is known as “threshold-less” lasing [34].

The value of β can be established from the ratio of output intensity before and after threshold on the L-L plot in Figure 6.21, and is found to be 73%, 76% and 50% for samples A, B and C respectively. These high values could suggest an amplified spontaneous emission system, as mentioned previously for a single nanorod with poor cavity [35]. This ASE, or superluminescence, is difficult to distinguish from pure stimulated emission with the current measurement system used.

6.5 Conclusion

A significant enhancement in the performance of an InGaN/GaN MQW heterostructure has been obtained by combining single nanorod emitters with SP coupling. The enhancement due to a reduction in QCSE found with nanorod fabrication is increased further by SP coupling to an Ag film, which results in a fast recombination mechanism and increased DOS in the system. The outcome is a very high performance nano-emitter and the observation of potential stimulated emission.

From this, single mode plasmonic nanolasers have been demonstrated, comprised of an individual semiconductor nanorod/dielectric/metal structure. The nanorod is fabricated by a simple top-down method from a commercial epiwafer based on an InGaN/GaN QW-LED structure. This is the first reported plasmonic laser that can operate with stimulated emission modes at room temperature. The laser shows a very low threshold with a high β value and strong mode confinement in the sub-wavelength range. The evidence presented strongly suggests stimulated emission is observed, however amplified spontaneous emission cannot be ruled out as the cause of the narrowing FWHM and observed sharp PL peaks. This is due to the large spontaneous emission component observed in the spectra, caused by enhancement of the emission from the MQW structure by SP modes separate to stimulated emission. Further work that may be used to investigate this is discussed in the following chapter.

As the semiconductor nanorod consists of both n- and p- doped regions, electrical driven plasmon lasers are likely to be realised in the near future with suitable contact fabrication. This work paves the way for ultra-small lasers in applications for future advanced on-chip integrated optical circuits.

References

- ¹Y.-J. Lu, H.-W. Lin, H.-Y. Chen, Y.-C. Yang, and S. Gwo, “Single InGaN nanodisk light emitting diodes as full-color subwavelength light sources”, *Applied Physics Letters* **98**, 233101 (2011).
- ²J. Wang, M. S. Gudiksen, X. Duan, Y. Cui, and C. M. Lieber, “Highly polarized photoluminescence and photodetection from single indium phosphide nanowires.”, *Science (New York, N.Y.)* **293**, 1455–7 (2001).
- ³R. F. Oulton, V. J. Sorger, T. Zentgraf, R.-M. Ma, C. Gladden, L. Dai, G. Bartal, and X. Zhang, “Plasmon lasers at deep subwavelength scale”, *Nature* **461**, 629–32 (2009).
- ⁴F. Rana, C. Manolatou, and S. G. Johnson, “Nanoscale Semiconductor Plasmon Lasers”, 2007 Conference on Lasers and Electro-Optics (CLEO), 1–2 (2007).
- ⁵A. Banerjee, R. Li, and H. Grebel, “Surface plasmon lasers with quantum dots as gain media”, *Applied Physics Letters* **95**, 251106 (2009).
- ⁶Y.-J. Lu, J. Kim, H.-Y. Chen, C. Wu, N. Dabidian, C. E. Sanders, C.-Y. Wang, M.-Y. Lu, B.-H. Li, X. Qiu, W.-H. Chang, L.-J. Chen, G. Shvets, C.-K. Shih, and S. Gwo, “Plasmonic nanolaser using epitaxially grown silver film”, *Science* **337**, 450–3 (2012).
- ⁷B. Bhushan, “Adhesion and stiction: Mechanisms, measurement techniques, and methods for reduction”, *Journal of Vacuum Science & Technology B: Microelectronics and Nanometer Structures* **21**, 2262 (2003).
- ⁸M. J. Holmes, Y. S. Park, X. Wang, C. C. S. Chan, B. P. L. Reid, H. Kim, R. A. Taylor, J. H. Warner, and J. Luo, “Optical studies on a single GaN nanocolumn containing a single InGaN quantum disk”, *Applied Physics Letters* **98**, 251908 (2011).
- ⁹J. Bruckbauer, P. R. Edwards, J. Bai, T. Wang, and R. W. Martin, “Probing light emission from quantum wells within a single nanorod.”, *Nanotechnology* **24**, 365704 (2013).
- ¹⁰J.-L. Liu, R. Xia, and Y.-T. Zhou, “Stiction of a Nano-Beam with Surface Effect”, *Chinese Physics Letters* **28**, 116201 (2011).
- ¹¹H. Rong, R. Jones, A. Liu, O. Cohen, D. Hak, A. Fang, and M. Paniccia, “A continuous-wave Raman silicon laser.”, *Nature* **433**, 725–8 (2005).
- ¹²K. D. Hirschman, L. Tsybeskov, S. P. Duttagupta, and P. M. Fauchet, “Silicon-based visible light-emitting devices integrated into microelectronic circuits”, *Nature* **384**, 338–341 (1996).

- ¹³M. H. Huang, S. Mao, H. Feick, H. Yan, Y. Wu, H. Kind, E. Weber, R. Russo, and P. Yang, “Room-temperature ultraviolet nanowire nanolasers.”, *Science* (New York, N.Y.) **292**, 1897–9 (2001).
- ¹⁴F. Qian, Y. Li, S. Gradecak, H.-G. Park, Y. Dong, Y. Ding, Z. L. Wang, and C. M. Lieber, “Multi-quantum-well nanowire heterostructures for wavelength-controlled lasers.”, *Nature materials* **7**, 701–6 (2008).
- ¹⁵K. Hennessy, A. Badolato, M. Winger, D. Gerace, M. Atatüre, S. Gulde, S. Fält, E. L. Hu, and A. Imamoglu, “Quantum nature of a strongly coupled single quantum dot-cavity system.”, *Nature* **445**, 896–9 (2007).
- ¹⁶H. Altug, D. Englund, and J. Vučković, “Ultrafast photonic crystal nanocavity laser”, *Nature Physics* **2**, 484–488 (2006).
- ¹⁷H. Gao, A. Fu, S. C. Andrews, and P. Yang, “Cleaved-coupled nanowire lasers.”, *Proceedings of the National Academy of Sciences of the United States of America* **110**, 865–9 (2013).
- ¹⁸B.-H. Li, C. E. Sanders, J. McIlhargey, F. Cheng, C. Gu, G. Zhang, K. Wu, J. Kim, S. H. Mousavi, A. B. Khanikaev, Y.-J. Lu, S. Gwo, G. Shvets, C.-K. Shih, and X. Qiu, “Contrast between surface plasmon polariton-mediated extraordinary optical transmission behavior in epitaxial and polycrystalline Ag films in the mid- and far-infrared regimes.”, *Nano letters* **12**, 6187–91 (2012).
- ¹⁹D. Bergman and M. Stockman, “Surface Plasmon Amplification by Stimulated Emission of Radiation: Quantum Generation of Coherent Surface Plasmons in Nanosystems”, *Physical Review Letters* **90**, 027402 (2003).
- ²⁰R. F. Oulton, V. J. Sorger, D. a. Genov, D. F. P. Pile, and X. Zhang, “A hybrid plasmonic waveguide for subwavelength confinement and long-range propagation”, *Nature Photonics* **2**, 496–500 (2008).
- ²¹M. A. Noginov, G. Zhu, A. M. Belgrave, R. Bakker, V. M. Shalaev, E. E. Narimanov, S. Stout, E. Herz, T. Suteewong, and U. Wiesner, “Demonstration of a spaser-based nanolaser.”, *Nature* **460**, 1110–2 (2009).
- ²²Q. Wang, J. Bai, Y. P. Gong, and T. Wang, “Influence of strain relaxation on the optical properties of InGaN/GaN multiple quantum well nanorods”, *Journal of Physics D: Applied Physics* **44**, 395102 (2011).
- ²³H. Zhao, R. A. Arif, Y. K. Ee, and N. Tansu, “Optical Gain and Spontaneous Emission of Strain-Compensated InGaN-AlGaIn Quantum Wells Including Carrier Screening Effect”, in , Vol. 6889, edited by M. Osinski, F. Henneberger, and K. Edamatsu (Feb. 2008), pages 688903–10.

- ²⁴P. Dawson, B. Puygranier, and J.-P. Goudonnet, “Surface plasmon polariton propagation length: A direct comparison using photon scanning tunneling microscopy and attenuated total reflection”, *Physical Review B* **63**, 205410 (2001).
- ²⁵H. Zhao and N. Tansu, “Optical gain characteristics of staggered InGaN quantum wells lasers”, *Journal of Applied Physics* **107**, 113110 (2010).
- ²⁶F. Binet, J. Y. Duboz, N. Laurent, C. Bonnat, P. Collot, F. Hanauer, O. Briot, and R. L. Aulombard, “Realization and optical characterization of etched mirror facets in GaN cavities”, *Applied Physics Letters* **72**, 960 (1998).
- ²⁷X. Duan, Y. Huang, R. Agarwal, and C. Lieber, “Single-nanowire electrically driven lasers”, *Nature* **421**, 241–245 (2003).
- ²⁸S. Nakamura and S. Chichibu, *Introduction to Nitride Semiconductor Blue Lasers and Light Emitting Diodes* (Taylor & Francis, London and New York, 2000).
- ²⁹J. J. Zayhowski and A. Mooradian, “Single-frequency microchip Nd lasers.”, *Optics letters* **14**, 24–6 (1989).
- ³⁰M. A. Zimmler, J. Bao, F. Capasso, S. Müller, and C. Ronning, “Laser action in nanowires: Observation of the transition from amplified spontaneous emission to laser oscillation”, *Applied Physics Letters* **93**, 051101 (2008).
- ³¹S. Linic, P. Christopher, and D. B. Ingram, “Plasmonic-metal nanostructures for efficient conversion of solar to chemical energy”, *Nature Materials* **10**, 911–21 (2011).
- ³²H. Y. Ryu, M. Notomi, E. Kuramoti, and T. Segawa, “Large spontaneous emission factor in the photonic crystal monopole-mode laser”, *Applied Physics Letters* **84**, 1067 (2004).
- ³³S. Reitzenstein, A. Bazhenov, A. Gorbunov, C. Hofmann, S. Münch, A. Löffler, M. Kamp, J. P. Reithmaier, V. D. Kulakovskii, and A. Forchel, “Lasing in high-Q quantum-dot micropillar cavities”, *Applied Physics Letters* **89**, 051107 (2006).
- ³⁴K. H. Li, Z. Ma, and H. W. Choi, “High-Q whispering-gallery mode lasing from nanosphere-patterned GaN nanoring arrays”, *Applied Physics Letters* **98**, 071106 (2011).
- ³⁵E. Feltin, A. Castiglia, G. Cosendey, L. Sulmoni, J.-F. Carlin, N. Grandjean, M. Rossetti, J. Dorsaz, V. Laino, M. Duelk, and C. Velez, “Broadband blue superluminescent light-emitting diodes based on GaN”, *Applied Physics Letters* **95**, 081107 (2009).

Conclusions and Future Work

7.1 Conclusions

This thesis presents work combining plasmonic enhancement with nanostructure fabrication techniques to successfully improve the emission efficiency of InGaN based optical emitters. Due to their use in current state of the art LED based lighting solutions, improvements to InGaN emitters could produce large savings in energy in the illumination and lighting sector.

An initial investigation into the nanostructuring of InGaN/GaN MQW structures was performed, and significant enhancements in emission were obtained, suggesting a cost effective method of improving the performance of InGaN based LEDs. An increase in extraction efficiency was observed with angular resolved PL measurements, and an internal quantum efficiency increase was observed with temperature dependant PL. The time decay of nanorod structures was measured, allowing the exciton recombination dynamics of nanorods to be investigated. It was concluded that the enhancement found with a nanorod array structure is due to strain relaxation and in-plane exciton confinement.

PL measurements on a series of InGaN/GaN MQW nanorod array samples were carried out along with corresponding planar as grown samples. A clear phonon replica peak was observed for all samples, which is reduced when a sample is fabricated into a nanorod structure. The change in phonon-exciton coupling was quantified with the Huang-Rhys factor and Gaussian fitting, showing in particular a reduction in LO-phonon interaction for nanorod structures. This has recently been linked to improvements in efficiency droop, and high power PL measurements were performed which confirm an improvement in efficiency with increasing excitation power, due to a reduction in indirect Auger recombination [1].

Surface plasmon-QW interaction was studied as a function of Ag film thickness in close proximity to an InGaN SQW, where an Ag film coating was found to signif-

ificantly increase the internal efficiency of an InGaN SQW sample. The optimum Ag thickness and deposition conditions were obtained experimentally, showing a clear relationship between film thickness, morphology, and increased emission [2]. Efficiency increase was quantified with temperature dependant PL methods, and time resolved PL measurements were used to describe the coupling dynamics between surface plasmons and excitons in an InGaN QW.

Finally to combine the above enhancement techniques, single nanorod emitters were developed and enhanced with SP coupling, showing large enhancements of the InGaN QW structure compared to an as grown planar sample. Stimulated emission from single NRs enhanced by SP coupling was observed, which may be an important result for developing nano-lasers for lithography and system-on-chip uses. Measurements of power dependant PL allowed a stimulated emission threshold to be observed, and the emission was characterised showing a large spontaneous emission component due to the coupling of excitons into SP modes, resulting in a high beta value.

7.2 Future Work

7.2.1 Advanced Photoluminescence Studies

TRPL

TRPL, using an ultra-fast pulsed laser excitation source and detector is used to measure the decay time of individual carriers in a structure. The recombination paths and efficiency of various structures can be compared by this method, allowing various characteristics to be observed. For NRs, such measurements show real efficiency increases, and are vital for understanding the complex recombination mechanisms in nanostructures. For plasmonics, massive increases in carrier radiative decay time have already been observed [3], allowing a better understanding of the recombination mechanisms and real efficiency increases.

To further this work, TRPL measurements of single NRs enhanced by SP coupling would allow an understanding of the recombination mechanisms and coupling regimes, and allow an insight into the stimulated emission observed in single nanorods. Measuring a single nanostructure with a μ PL system using a conventional laser and detector proves to be difficult but possible, however coupling a TRPL system with ultrafast laser and extremely sensitive detector creates many problems and as yet is not possible with the systems used in this work. Measurement of single nanorods at changing collection angle would also be a useful technique for analysing the polarity and direction of the observed stimulated emission.

Photoluminescence Excitation

Photoluminescence excitation (PLE) measurements are taken at an individual emission wavelength, close to the bandgap emission of a sample, while the excitation source wavelength is changed. This allows many characteristics to be observed, including the Stokes shift of a sample, and complex absorption and emission properties resulting from defects and other recombination paths. PLE measurements may provide vital insight into the recombination pathways in a SP enhanced InGaN QW structure, and would be a useful next step in this work.

Polarisation

An increase in emission polarisation is useful for several applications, such as new display technologies, and initial testing of the emission polarisation of InGaN QWs has produced promising results, with NR fabricated samples appearing to have a higher degree of polarisation than a planar as grown counterpart. The optical measurement system used in this work involves the use of a monochromator with a grating, which can act as a polariser during collection of the sample emission. As such, obtaining accurate polarisation data is difficult and needs the development of a new system of optics.

The same system could also be used to measure the effect plasmonic interaction has on the polarisation of an InGaN/GaN QW, as recombination via SPs instead of the normal exciton recombination path in GaN will have an effect on the emission polarisation.

Finally the polarisation degree of the stimulated emission found with surface plasmon enhanced single nanorods would provide details of the complex recombination dynamics in such structures.

Electrical Injection

Difficulties in producing LED devices enhanced by nanorod fabrication stem from the potential short circuit path created due to the nanorod etching. If metal is deposited onto a nanorod LED structure, it would fill between the nanorods and effectively short the p-type and n-type regions, resulting in no light output. A method to overcome this involves insulation of the nanorod sidewalls or infilling of the gaps between nanorods. Both methods produce many difficulties due to the nanoscale fabrication techniques required, including the need for extremely accurate etch back procedures to uncover the electrical contacts after insulating the nanorods. Initial work has demonstrated electrically injected nanorod LEDs with good emission and electrical properties, [4] and future work on improving uniformity and reliability will produce promising results.

A surface plasmon enhanced InGaN LED has been demonstrated, [5] and currently involves the use of growth interruption techniques to ensure the Ag particles used for SP enhancement are located close enough to the InGaN active region. Improvements in the thinning of p-type material will allow SP enhanced nanorods with excellent properties by utilising a “flip-chip” design, however the p-type material must be below approximately 47 nm (the surface plasmon fringing field in a GaN/Ag structure), which is currently difficult to produce [5].

Electrical injection into single nanorods presents a variety of problems due to the size of the structures – being too small for typical lithography techniques. Contacts have been formed on individual nanorod structures, by focussed ion beam deposition or e-beam lithography techniques [6]. This is a time consuming and difficult process however with low yield, and the electrical properties of such contacts are generally poor. Metal contacts to the InGaN/GaN nanorods presented here could be achieved with FIB, e-beam, or a fabrication method of carrier wafer recessing to hold nanorods in a known location. All would be excellent future work, and would contribute to achieving electrically injected single nanorod lasing.

References

- ¹P. Renwick, H. Tang, J. Bai, and T. Wang, “Reduced longitudinal optical phonon-exciton interaction in InGaN/GaN nanorod structures”, *Applied Physics Letters* **100**, 182105 (2012).
- ²P. Renwick, H. Tang, Q. Wang, R. Smith, and T. Wang, “Enhanced internal quantum efficiency of an InGaN/GaN quantum well as a function of silver thickness due to surface plasmon coupling”, *Physica Status Solidi (c)* **8**, 2176–2178 (2011).
- ³K. Okamoto, I. Niki, A. Shvartser, Y. Narukawa, T. Mukai, and A. Scherer, “Surface-plasmon-enhanced light emitters based on InGaN quantum wells”, *Nature Materials* **3**, 601–605 (2004).
- ⁴J. Bai, Q. Wang, and T. Wang, “Characterization of InGaN-based nanorod light emitting diodes with different In compositions”, *Journal of Applied Physics* **111**, 113103 (2012).
- ⁵C.-Y. Cho, M.-K. Kwon, S.-J. Lee, S.-H. Han, J.-W. Kang, S.-E. Kang, D.-Y. Lee, and S.-J. Park, “Surface plasmon-enhanced light-emitting diodes using silver nanoparticles embedded in p-GaN.”, *Nanotechnology* **21**, 205201 (2010).
- ⁶X. Duan, Y. Huang, R. Agarwal, and C. Lieber, “Single-nanowire electrically driven lasers”, *Nature* **421**, 241–245 (2003).

